ABSTRACT

NEIRA ARCE, ALDERSON. Thermal Modeling and Simulation of Electron Beam Melting for Rapid Prototyping on Ti6Al4V Alloys. (Under the direction of Dr. Jerome Cuomo.)

To be a viable solution for contemporary engineering challenges, the use of titanium alloys in a wider range of applications requires the development of new techniques and processes that are able to decrease production cost and delivery times. As a result, the use of material consolidation in a near-net-shape fashion, using dynamic techniques like additive manufacturing by electron beam selective melting EBSM represents a promising method for part manufacturing. However, a new product material development can be cost prohibitive, requiring the use of computer modeling and simulation as a way to decrease turnaround time.

To ensure a proper representation of the EBSM process, a thermophysical material characterization and comparison was first performed on two Ti6Al4V powder feedstock materials prepared by plasma (PREP) and gas atomized (GA) processes. This evaluation comprises an evaluation on particle size distribution, density and powder surface area, collectively with the temperature dependence on properties such as heat capacity, thermal diffusivity, thermal conductivity and surface emissivity. Multiple techniques were employed in this evaluation, including high temperature differential scanning calorimetry (HT-DSC), laser flash analysis (LFA), infrared remote temperature

analysis (IR-Thermography), laser diffraction, liquid and gas pycnometry using mercury and krypton adsorption respectively.

This study was followed by the review of complementary strategies to simulate the temperature evolution during the EBSM process, using a finite element analysis package called COMSOL Multiphysics. Two alternatives dedicated to representing a moving heat source (electron beam) and the powder bed were developed using a step-by-step approximation initiative. The first method consisted of the depiction of a powder bed discretized on an array of domains, each one representing a static melt pool, where the moving heat source was illustrated by a series of time dependant selective heating and cooling steps. The second method consisted of the solution of a prescribed domain, where each powder layer is discretized by an individual 3D element and the heat source is represented by a 1D element displaced by a temperature-coupling extrapolation routine. Two validation strategies were presented here; the first was used to confirm the accuracy of the proposed model strategy by setting up a controlled experiment; the second was used to validate the post-processing data obtained by the simulation by comparison with in-situ measured EBSM process temperature.

Finally, a post-process part evaluation on surface finishing and part porosity was discussed including an assessment of the use of non-destructive inspection techniques such as 3D profilometry by axial chromatism for surface roughness, partial section analysis by serial block-face scanning electron microscopy (SBFSEM) and micro computed tomography (CT-Scan) for pore and inclusion detection.

Thermal Modeling and Simulation of Electron Beam Melting for Rapid Prototyping on Ti6Al4V Alloys

by
Alderson Neira Arce

A dissertation submitted to the Graduate Faculty of
North Carolina State University
in partial fulfillment of the
requirements for the Degree of
Doctor of Philosophy

Materials Science and Engineering

Raleigh, North Carolina

2012

APPROVED BY:

Dr. Jerome Cuomo
Advisory Committee Chair

Dr. Michael Rigsbee
Committee Member

Dr. John S. Strenkowski
Committee Member

Dr. Jonathan Bohlmann
Committee Member

DEDICATION

This dissertation is dedicated to my grandmother Rosita for her kindness and devotion while teaching me the value of persistence and dedication; to my mother Elizabeth for her endless and unconditional support; to my wife Lilian for her encouragement, love and friendship and to my daughter Kristen for bringing me happiness every day of my life.

BIOGRAPHY

Alderson Neira Arce was born in Palmira - Colombia. At an early age he started his interest in science and technology, leading him to pursue his high school education on a technical institution specialized in metallurgical processes. This early education allowed him to rapidly advance on his undergraduate studies in materials engineering by supporting teaching activities in a wide variety of materials and applications. Thanks to his constant support on academic matters; together with a faculty member, worked towards the formation of a research center facility focused on the fabrication of state-of-the-art materials using ultra thin coatings aided by plasma processes, for metal mechanical as well as biomedical applications; this work was possible with the support of the national council for scientific research COLCIENCIAS. Understanding that novel material research is time and cost demanding, he pursued his research on modeling and simulation of processes to decrease the amount of experimental work. As a next stage in his career, he initiated his studies in non-destructive inspection and plan asset management in Kyushu Institute of Technology, (Kyushu Japan), that later led him to start a new material evaluation division sponsored by the Japanese International Collaboration Agency – JICA, project that opened new research opportunities this time on the petrochemical sector with a wide spectrum of applications. Always interested in new research prospects, he decided to start his graduate education on rapid manufacturing, where he made his contribution on solid lubricant surfaces produced by Laser Engineered Net Shaping and later by the modeling and simulation of Electron Beam Melting processes, the later research led by Dr. Jerome Cuomo at the Institute of Maintenance Science and Technology in North Carolina State University. Additional activities during graduate school includes the use of atmospheric plasmas for digital micro fluidics applications on electro wetting on dielectric devices as well as destructive and non-destructive characterization of metal, polymers and composite materials.

ACKNOWLEDGMENTS

For their guidance and mentorship, I would like to thank Dr. Jerome Cuomo, Dr. Denis Cormier, Dr. Dick Guarnieri, Dr. John Strenkowski, Dr. Michael Rigsbee and Dr. Jonathan Bohlmann.

For their financial support I would also especially like to thank the Laboratory for Integrated Manufacturing Science and Technology (LIMST) at NC State University as well as the U.S. Department of Defense, through the Strategic Environmental Research and Development Program (SERDP) - Project No. WP-1762, the Navy Small Business Innovation Research - Project No. N102-166-0752 and Bennett Aerospace Inc.

For their group effort at LIMST - MSE, to Darin Thomas, Shaphan Jernigan, James Mulling, Dr. Steven Hudak and Dr. Roger Sanwald.

For their invaluable technical support on this dissertation to Dr. Ilir Beta, Robert Campbell and Bob Fidler at NETZSCH Instruments of North America, LLC; Joel Mancuso and Rich Fiore at Gatan Inc.; Steven Neptun, Luke Hunter and Naomi Kotwal at Xradia Inc.; as well as Peter Davis and Brett Muehlhauser from North Star Imaging Inc.

At NC State University I would like to extend my gratitude to Dr. Christopher Bobko from CCEE, as well as Tim Horn and Dr. Ola Harrison at ISE.

To my dear friends Dr. Federico Sequeda, Dr. Thomas Scharf, Dr. Nalin Kumar, Dr. Christopher Oldham, Dr. Theodore Winger, Victor Prince, Brad Hartman, Matthew King, Ty Wang, Dr. Anthony McWilliams and Dr. Jackson Thornton.

Last but not least to Edna Deas for her appreciation and constant support during all the graduate program process.

TABLE OF CONTENTS

LIST OF FIGURES

LIST OF TABLES

Introduction

Titanium and titanium alloys are considered an attractive material, when properties such as high strength-to-weight ratio, resistance to corrosion, fatigue, cracking and biological inertness are desired. Unfortunately, due to the high cost of these materials most of its use is dedicated to aerospace and biomedical applications.

Compared with materials such steel, titanium's high cost does not originate from its rarity (being ninth most abundant element on earth's crust and sixth most abundant metal [1]), but from its complex extraction and refining process [2, 3]; initiated by the reaction of titanium oxide extracted from the ore with chlorine to produce titanium tetrachloride, followed by a metallic reduction with sodium or magnesium at high temperatures resulting in a porous metal called a sponge. This process requires the use of high amounts of energy, a controlled environment to prevent oxygen and nitrogen embrittlement and its production is limited by individual batches, noticeably increasing the conversion cost. Later, additional expenses are incurred during the ingot production; again due to titanium's chemical reactivity, where environment controlled processes such as vacuum arc remelting (VAR) is required.

Once a raw material with sufficient quality is obtained, the challenge start in finding an economical path to producing an end-product; reason why the overall processes for titanium and titanium alloys are continuously improved, from optimizing the titanium extraction and refining process from the ore [4-6] to cost reduction by minimization of the necessary amount of material to produce a given product.

Several methods are available for metal refining and manufacturing process, departing from conventional casting and extractive processes; to final shape using fusion, solid state welding, superplastic bonding, laser welding and recently the use of net shaping and near-net shaping technologies. This includes processes such as powder metallurgy, cold isostatic pressing, stamping and roll compaction, [7] vacuum plasma spray forming, (VPSF) [8], friction stir welding and electron beam selective melting (EBSM), among others [9, 10].

Electron beam selective melting (EBSM), is a near net shape process attractive due to its unification of powder consolidation, welding and rapid solidification into a single step without the obstacles encountered in casting, forging and powder metallurgy, related with surface reactivity and allowing element segregation presented on titanium and its alloys [11, 12]. This process represents a promising opportunity to increase the use of titanium alloys due to its process flexibility, non-reactive environmental requirements (since the process runs in vacuum) and fast processing.

Additionally, this technique offers a more efficient and economical way to manufacture titanium parts, by a continuous effort to improve the manufacturing practice itself delivering a higher-quality product and decreasing the cost on post-processing once the part is completed. Therefore the use of EBSM process for processing titanium alloys such as Ti6Al4V, represents a viable alternative to manufacture fully functional parts for aerospace and medical applications at lower cost and lead times.

Currently, Ti6Al4V microstructures obtained by the EBSM process are mainly characterized by columnar shaped morphologies, with a growth orientation parallel to the build direction. These morphologies are mainly composed of (α+β) structures, namely Widmanstätten from α-platelets (acicular or plate-like) with rod-like β phase formed on the interfaces of the fine α grains [13-15], in some cases with the presence of a martensitic α' phase [16, 17] with some evident differences in phase size and distribution from bottom to top of the build. Even though a variety of studies have been performed on the microstructure evolution of Ti6Al4V alloys during the EBSM process, it is still difficult to forecast a microstructure caused by the intricate combination of thermal events [18], and considering experimental studies performed by trial and error are cost prohibitive, the development and refinement of numerical models representing the temperature distribution during the built including the thermal and physical properties of the material being processed is necessary.

As a result, factors such as rapid solidification, fast scan rates, and the thermal cycling inherent from the process must be examined to further understand the effect of system parameters on microstructure development. With this purpose, an overall review of the electron beam selective process was conducted here. Starting from a comparison of the thermophysical properties of Ti6Al4V powder feedstock (used as a raw material) produced by plasma (PREP) and gas atomization (GA) and how their characteristics evolves through the additive manufacturing process from as-received (raw state) powder feedstock to pre-heated, partially sintered and finally into solid or as-built state.

The information compiled from the physical and thermal characterization on the powder feedstock will ultimately be used to better represent the temperature evolution occurring during the EBSM process. This was possible by means of a numerical simulation, representing the electron beam as a moving heat source within the powder material and the powder bed was discretized as a continuous three-dimensional transient heat conductive field. A step-by-step method was used to solve discrete domains representing a single-layer material later to be used as initial condition for the subsequent additive layer. Considering the complex factors at work in this manufacturing process (i.e. high cooling rates, melt pool size, marangoni effects, etc.), model verification was only conducted on the robustness of the mathematical representation and numerical convergence. However, a model validation was conducted to prove the model validity using actual in-situ process monitoring data from the EBSM production equipment, later used as feedback for model correction. Finally, in this study, an evaluation on EBSM parts on surface quality and volumetric porosity was addressed by using non-destructive inspection techniques.

This work presents an overview for the additive manufacturing process, presenting new data for the powder feedstock not yet available that will allow the development of better and more accurate simulation models, providing reliable information mainly focused on shorter turnaround times for prototyping and a higher-quality final product by the use of for better microstructure predictor tools.

1. Additive Manufacturing, Modeling and Simulation

1.1. Rapid Prototyping and Manufacturing

Rapid prototyping and manufacturing is an additive process playing an important role in the development of new materials and parts, when design, process conditions and delivery times are difficult to attain by conventional methods like casting or extractive methods [19]. The process is initiated by the use of a computer aided designed CAD drawing of the part to be built, including dimensions and tolerances. Later, the 3D information is processed to be used within the additive system, discretizing the 3D model into a set of 2D layer slices (*x,y* coordinates) and the *z-axis* is set by the individual layer thickness, controlled by the build hatch within the additive system. The part is then processed, layer by layer, until the final shape is obtained.

Net shape or near-net shape processes were initially designed to enable the production of new parts at low cost. As a response to these requirements, powder metallurgy made its appearance as an attractive option, to manufacture net shape custom parts in a short period of time through heating of and subsequent pressure application to the part by hot isostatic pressing process HIPS [20] to obtain minimum porosity values. Although powder metallurgy provided a new venue to process a wide range of materials, the use of molds limited the manufacture of complex shapes like inner features where a two part mold must be used, as well as the difficulty to process some metal powder alloys prone to high levels of environmental corrosion and embrittlement.

As a result of the aforementioned limitations, a new series of processing methods consisting on an additive free-form principle called rapid prototyping and/or manufacturing made its appearance, enabling the processing of low and high melting temperature materials such as polymer-based elements, cermets, refractory metals and wide variety of intermetallics. These techniques were mainly classified according to the delivery method for the additive material, the source used for agglomeration, the state of the material prior to deposition and the material temperature process condition. When high melting point materials were to be processed, higher-heat sources were used, especially for metals and ceramic materials. For this, two different methods were designed to deliver the material prior to processing.

The first method developed was direct-melt processing, consisting of selective delivery of metal and ceramic materials to the location of deposition (i.e. Laser Engineered Net Shaping – LENS) providing extensive flexibility for processing, tolerances and build time. However, the preferential deposition of powder material to be further melted by the laser, causes lack of temperature control over the build part where the majority of the heat is lost by conduction through the build plate, creating undesirable temperature gradients, resulting on highly stressed and in some cases delaminated parts between the deposited layers during the build[21].

The second method designed was the powder bed process, where a layer of powder is placed on the build plate and a heat source such as a laser or an electron beam, selectively melts the area of the part, with the remaining powder material acting as a structural support, maintaining a stable built temperature thanks to the low thermal conductivity on the loosely sintered powder. Several manufacturing techniques using a powder bed as an initial process stage made their appearance in this arena, such as laser assisted additive manufacturing (LAAM). One of the most remarkable techniques is the selective laser sintering (SLS), in which the powder material is partially sintered below its melting temperature, followed by a high peak laser to melt the powder material. This versatile process allowed the manufacturing of a wide range of materials, from polymers to metals, using single or mixed composition powders. Even though this alternative seems effective for many applications, there are still limitations to be addressed involving the use of a laser as a heat source such as:

a. *High power requirement to melt metal powders*: As the power is increased, the penetration depth is decreased, requiring a higher laser dwell time disabling the control on adverse processes like recrystalization and annealing [22].
b. *Restricted thermal capacitance of the mirror galvanometer:* Together with a high inertia of the mirrors within the scanning system, prevents the laser track accuracy [23, 24].
c. *Longer dwell times represent longer process time and higher costs*.
d. *Material sensitivity to environmental contamination:* Corrosion or stress cracking is induced by atmospheric contamination as well as the gas shielding reacting with the processed material in the case of atmospheric or pressurized processing.
e. *Power efficiency*: Related with the limitations of processing materials with high laser reflectivity (i.e. native metal oxides)
f. Low beam quality of high beam lasers

These delivered power and scan speeds limitations on SLS technologies led to the development of a new technology emerged from a conventional method in which an electron beam was initially used to melt and refine materials highly susceptible to corrosion and environmental contamination[25, 26]. This gave birth to the Electron Beam Selective Melting process (EBSM) first designed by ARCAM AB, consisting of a focused, high-energy electron beam, deflected by magnetic lens, melting the powder material in a layer-by-layer fashion to build a physical part.

Like any new material processing technology, a learning curve had to be developed to improve the process robustness; solving end-product non-conformities like warping, stress build up, preferential grain orientation, porosity, and surface finishing, to name a few. With the aim to improve the quality of these manufactured parts, this work intends to gain a better understanding on factors related to the powder material properties used during the EBSM process (powder feedstock), the numerical representation required to best understand the process variables effect on the final built part properties, the use of in-situ control process data to validate and improve the proposed numerical process representation and the use of non-destructive inspection for surface and volumetric quality EBSM part assessment.

1.2. Electron Beam Selective Melting Process (EBSM)

The electron beam selective melting process EBSM (Figure 1.1) consists of the melting and solidification of a layer of metal powder, followed by an additive step (layer-by-layer) to create 3D elements. The heat source used in this process (electron beam) is generated by a tungsten filament through a thermionic emission in a high vacuum column (5 x 10^{-4} mBar). Immediately after electron generation, the beam is focused and steered by an array of magnetic deflectors, allowing high scan rates of 300 to 5000 cm/sec.

Figure 1.1. EBSM (ARCAM A-2) System Illustration

The beam impingement on the material generates high temperatures due to kinetic energy transfer from the accelerated electrons into thermal energy inside of the material, causing the metal powder to melt, with build rates close to 60 cm^3/hour [27]. In spite of required features to operate an electron beam such as high vacuum, together with the x-ray emission caused by the electron beam impingement on the powder surface, makes the EBSM environment very challenging for *in-situ* process monitoring.

Additionally, the hard architecture (unable to be modified for in-situ process control) of the ARCAM-AB system common on any production oriented equipment, makes it difficult to modify without affecting the original design, jeopardizing the process stability of the system; reason why the use of modeling and simulation of this additive manufacturing process represents an excellent strategy for material and process evaluation.

1.3. EBSM Process of Ti6Al4V Alloys

The preferential use of EBSM to process Ti6Al4V alloys is required due to titanium's alloys susceptibility to contamination and embrittlement by elements like hydrogen, nitrogen and oxygen. As a result, companies like ARCAM-AB have been successfully manufacturing EBSM systems used for implant production. About 2% of all hip implants worldwide are manufactured on an ARCAM machine[28]. In aerospace, the EBSM technology is a developing process used for building prototypes and low-volume parts [28]. The main interest in aerospace application of near-net shape of Ti6Al4V alloys by EBSM process lays on the low level of machinability required, decreasing the use of low cutting speeds and heavy feed rates [29, 30].

Having a finished or a near finished manufactured part by EBSM process does not imply the required mechanical properties required by the standards for a specific application are met, or how close the EBSM manufactured product is to be *use-ready*, or if a post-processing procedure is required to modify the resulting material microstructure. Since microstructure and mechanical properties of Ti6Al4V alloys are heat treatment and processing history dependent [17, 31-33], a predictor method is required to estimate the resulting EBSM microstructure, able to mimic the heat evolution originated from a series of melting and re-melting steps occurring every time a new layer of material is deposited [13], making a numerical representation by modeling and simulation to be a rather complex and time-consuming task.

Once the EBSM part is built, a series of process validations are required to ensure that the performance of the part meets the regulatory properties necessary to be used in medical or aerospace applications. For medical uses, the manufactured specimens demonstrated that EBSM processed Ti6Al4V has comparable, and in several cases superior, chemical and mechanical properties to those designed for surgical implant applications based on quality technical standards such as ASTM

F136-02a and ASTM F1108-04 [34-36], as well as biocompatibility and bioactivity [37, 38].

Early work on aerospace applications showed the advantages of EBSM process on structural metallic components such as rocket engine impellers [33], turbine blades, spare components for environmental control and life support systems (ECLSS) and command and liaison vehicle (CLV) parts[39], among others. On the other hand, aircraft components are currently being manufactured with this technology [40, 41] for quick response tooling, lower recurring unit part costs and faster part delivery times. These improvements come mainly through material requirement changes and design modifications, such as replacing aluminum and steel parts with titanium and making a single part instead of an assembly [27] .

1.4. Modeling the Rapid Prototyping and Manufacturing Process

Despite the progress in additive processes by rapid prototyping and manufacturing, the thermal evolution responsible for the final microstructure and built part properties is a constraint due to limitations on the feasibility to measure the temperature during the process. Therefore, the use of numerical modeling represents a viable alternative by using fundamental principles in order to study the effect of the process variables over the thermal behavior of the building part.

However, the thermal model for beam-material interaction concerning EBSM becomes rather complex. In particular, the temperature-dependent properties of powder and the consideration of a moving heat source, together with a nontrivial geometry, represent a constraint for analytical solutions of the describing mathematical equations. Thus, numerical methods have been used to calculate the resulting temperature distribution, allowing approximate solutions of three dimensional differential equations with minor losses in accuracy [42]. In particular, the finite-element-method (FEM) subdivides the relevant part geometry into single domains of arbitrary shape which are called finite elements. Thus, the basic functions are only valid within the range of a certain element and comply with the adjacent elements. Consequently, the complete solution consists of a multitude of solutions from neighboring domains.

The Step-Wise Solution

Even though, attempts have been made to represent the thermal evolution of the additive process; a most important challenge is the ability to simulate the entire manufacturing process, including the additive process of complex geometries. With this purpose in mind, many thermomechanical and thermokinetic models have been devised to evaluate residual stress and microstructure, respectively. A practical way to solve a multilayer material deposition or a multidimensional moving boundary problem was initiated with laser-based technologies [43, 44] simulating the laser based deposition process of stainless steel 316L by finite element analysis (FEM) of a traveling volumetric heat source, representing the melt pool in a quasi- steady 2D simulation. The entire built material modeled was discretized in small cubic sub-domains assigning thermal insulation values to the elements (or material) not yet deposited. The movement of the melt pool as the material was deposited was represented by a time and space dependant heating of each element at melting temperature. Once an individual cube or material fraction solution was obtained, it was saved as the initial condition for a new element or material being deposited.

This gave rise to the stepwise solution for the heat transfer in layered manufacturing; consisting on the transient numerical solution of a discrete volume representing the melt pool, within a continuous three-dimensional transient heat conductive field representing the powder material. Here, the heat source or melt pool movement solution is obtained by partially solving the model at a specific location and using this partial solution as an initial condition for a new thermal event or heat source location for which is called the step-by-step method. This method was later followed by *Labudovic* and *Kovacevic* using the same birthing or partial solution events by assigning thermal insulation values to the elements or material not yet deposited through a thermo-mechanical coupled calculation as a representation of a heat source during the deposition of Monel on AISI 1006 [45]; including process parameters such as non-linear physical properties, thermal load, thermal flux densities and latent heat of fusion and neglecting effects such as the convective flow of heat, occurring between the melt pool and the solid part. This evaluation was made using ANSYS software aided by a parametric design language (APDL) for variable definition and simple looping to conduct an iterative analysis until a converged solution for dynamic equilibrium was attained.

Moreover, *Kelly* and *Kampe* [46] used the same approach employing a modeling application called Mathematica by Wolfram Research Inc. to study solid-state transformations and microstructure evolution on Ti6Al4V processed by laser metal deposition through a combination of cooling and reheating cycles common from multilayered process by simplifying the model to a 2D geometry; keeping one of the axes in a thermally steady-state condition using an implicit backward finite difference analysis. Temperature dependant properties were included in this model, although no heat losses caused by convection or radiation were considered. Later on, *Costa et al.* used ABAQUS, used the same birth element approach, to pursue a thermo-kinetic study by laser powder deposition (LPD) of tool steel iron (AISI 420), again the microstructure evolution caused by thermal cycling was modeled; such model included material thermal properties as well as heat losses by convection and radiation [47-49]. *Wang et al.*, improved this technique by automating the activation and deactivation of the elements in the algorithm model using the a finite element software SYSWELD [50]; program commonly used for heat treatment and welding modeling and compared it with a new approach, named "the dummy material" method, in which instead of deactivating the elements or sub-domains, they were given low conductivity values for energy conservation (in this way the forthcoming element would not be heated). These properties were later updated to the actual thermal conductivity value during element activation representing the material deposition [51].

Despite the accuracy of the previous approaches, the layer-by-layer evaluation required an enormous amount of computing resources, it made necessary the introduction of a fixed boundary method, first introduced by *Takeshita* and *Matsunawa* during the laser surface melting process of aluminum copper eutectic alloy [52], and further used and improved by *Ye et al.* [53]during the modeling and simulation of laser engineered net shaping process (LENS) deposition of a thin wall of stainless steel 316L; enabling mesh refining of the simulated elements using the following assumptions:

(1) The thermal conductivity, specific heat capacity, and other materials parameters in stainless steel 316L powder are temperature-independent;

(2) Only heat conduction in build and substrate are considered;

(3) The quasi-steady state is established, i.e. the molten pool does not change size with time;

(4) The temperatures of the element nodes are set as the melting point temperatures;

(5) The part to be formed is adiabatic.

During the modeling and simulation, the activation of elements were performed through a prescribed time step using ABAQUS, linked with the scanning speed of the laser and the amount of mass required to satisfy the melt pool volume. Energy distribution in the laser beam was considered the source of heat, instead of the powder particles at melting temperature. All these approximations were validated by temperature measurements obtained by high speed infrared (IR) thermal imaging during the process and the data was later used to support and correct the simulation values.

As seen before, some of the work conducted in this field neglects the laser energy distribution of the laser beam and estimates the powder particles at melting temperature as a heat source. This laser energy distribution was later evaluated by *Neela et al.* [54], through a multistep transient heat transfer analysis where the heat source was represented as a heat input with a non-uniform Gaussian distribution, where the elements are synchronized by smaller time increments. Herein, a number of elements were activated at each time step and determined by the evaluated volume of melt pool, which depends on the process conditions (powder mass flow rate, powder use efficiency, and scanning velocity).

Finally, the importance of the temperature properties for the powder material was shown by *Patil and Yadava* [55], where a model for an individual layer is used in metal laser sintering (MLS) to optimize the laser process conditions and avoid thermal distortion during cooling. This was done by the study of a non-uniform transient temperature distribution in the single powder layer of titanium caused by laser irradiation.

1.5. Electron Beam Selective Melting Simulation and Modeling

The knowledge base gathered as a result of previous efforts for simulation on laser assisted additive technologies, was later used to numerically solve a similar type of heat source. The electron beam melting process included a new energy source analogous to the laser process in terms of melting interaction volume (deep and narrow melt pool). Characterized by smaller beam spot sizes, faster scan rates now possible by the action of magnetic steering systems (contrary to the lower beam steering speeds attained by laser systems) as well as no limitation by reflection attenuation caused by the beam powder material interaction [56].

Besides the use of a different an energy source characterized by a high electron beam power (~4000W), additional process conditions characteristic from the EBSM technology like extremely fast scanning rates (up to 1000 m/s), a vacuum system (5x10^{-4} mBar), high cooling rates (~10 °C / min) [57], melt pool instabilities during the molten state [58-61], together with low alloy element vaporization, powder pushed-away or blown from the build plate caused by static charges accumulation on the powder due to poor contact between the powder particles, preferential grain growth caused by an unidirectional heat flux during the built, thermal stresses from temperature gradients developed during the process and built part porosity caused by un-melted powder particles and inner particle hollow cavities present on the powder feedstock material; makes the electron beam selective melting process modeling and simulation a non trivial task.

Considering this, early numerical simulations were mainly focused on the electron beam – melt pool interaction and its subsequent effect on chemical composition, specifically metal evaporation. Studies on the evaporation of low alloy elements in Ti6Al4V, due to transient local heating caused by the electron beam on the melt pool, were developed by *Powel et al.* [62]. Herein, the system was solved using a volumetric solution accounting for the electron beam penetration into the material and a thin film solution evaluating only the temperature distribution below the electron beam. Finally the model was validated by comparing evaporation rates from an electron beam furnace.

Later on, methods used to represent the melt pool and heat transfer process were the basis for EBSM modeling and simulation. This time additional process factors such as powder *"push-away,"* (mainly caused by static charge formation on the powder due to poor electrical conductivity) were included in the numerical model, leading to the study of the effect of the electron beam scan strategy on this phenomena. For this, an ANSYS 2D numerical representation was designed (but not experimentally validated) to study the different scan strategies in order to improve build heat distribution and diminish the push-away phenomena. As a result, new scan strategies were created (i.e. reversed scan mode, interlaced reverse scan mode) dedicated to eliminate the charging build-up as well as the non-uniform heat distribution responsible for stress concentration during the built [63].

Parallel to this work, *Zaeh* and *Kahnert* [24], used the concept of reducing the total power during the scan as the temperature attained by the pre-heating stage increases, improving the adhesion between sintered metal layers of H-13 steel; using an adaptive scan strategy as well as developing an adaptive electron beam power input to avoid overheating in areas previously melted. Later, *Zäh* and *Lutzmann* [64] worked on a model to substantially reduce the balling effect and delamination. The former created by melt pool surface energy instabilities, causing the presence of metal beads on top of a recently deposited layer causing a rough surface as initial condition for the upcoming material to be deposited and the latter caused by inadequate energy density transmitted from the electron beam into the powder. The model used by his group was the first to consider temperature-dependent properties such as emissivity, density, heat conductivity and heat capacity, but only in bulk material corresponding to a stainless steel 316 alloy, where heat conductivity in powder condition was calculated by using the Zehner/Bauer/Schlunder (SZB) model, estimating the effective heat conductivity of the examined powder below solidus temperature. This method consisted on the calculation of the thermal conductivity of a particulate media starting from known data from the bulk material and composed by a standard model cell containing two contacting particles where heat conduction and radiation between particles is accounted for.

This was followed by *Körner* and *Attar et al.* [65] who developed a 2D lattice Boltzmann model (which is an alternative to ordinary computational fluid dynamics models) to study the influence of factors such as the relative powder density, including factors such as the stochastic effect of a randomly packed powder bed, capillary and wetting phenomena on gas atomized (GA) Ti6Al4V powder. The proposed model, although still two dimensional (2D), was able to predict many experimental observations such as the well known surface energy instabilities causing the balling effect. As a result, the effect of the packing density over the melt pool characteristics was observed and a validation process was performed using gas atomized powder as a feedstock material. In this case, results were compared with experimental findings during electron beam selective melting EBSM and the comparison showed to be in good agreement with the simulated results.

1.6. The use of COMSOL Multiphysics Software on Additive Processes

For many years the use of modeling and simulation has been supporting conventional processes through the use of fundamental principles and empirical data to better represent and improve industrial processes [66]. The numerical representation of physical phenomena such as the EBSM technique requires the solution of multiple partial differential equations, product of a transient temperature evolution coupled with a moving heat source, not to mention the mutual interdependence on the material's thermal and physical properties with the temperature. For that purpose, previous researchers have used finite element analysis software packages such as ANSYS, Mathematica and ABAQUS among others, showing the increasing necessity for computer modeling software to improve the qualitative and quantitative process knowledge.

Considering the complexity of the EBSM process involving the conversion of electromagnetic (EM) fields into thermal energy that ultimately melts a metal powder layer. This process contains many variables influencing the outcome of the finished material. Therefore, the selection of a modeling and simulation tool is critical, requiring the use of a powerful system with the ability to be adapted to the very nature associated with electron beam selective melting. This means the coupling of thermal information with phase transformation and finally the as-built material properties.

COMSOL Multiphysics v.4.2a, is a commercially available software package that has the breadth and range of modeling functionality to accurately model the EBSM process. COMSOL has the advantage of providing multi-physics models in a combined functional model. This means that the software can work with multiple equations as it solves the simulation, even when the equations have interdependencies with one another. Previous data on similar applications showed the flexibility of COMSOL Multiphysics to model additive processes initially modeling the temperature evolution caused by a laser heat source interaction with a three-dimensional transient heat conductive field on a semi-infinite metallic solid [67, 68].

Later, the software was used to model the residual stresses developed by an electron beam heating using a double-ellipsoidal transient heat source [69]. Finally the EBSM process was modeled by *Zäh et. al*. [70] where factors such as temperature dependent properties for stainless steel (316L) material, heat losses by radiation, and electron beam penetration depth as a function of temperature were included. However, the challenge still remains in producing a numerical representation and modeling strategy of the heat transfer evolution not limited by a small EBSM built area but able to solve a layer-by-layer process, including not only estimated Ti6Al4V powder feedstock thermophysical properties [64, 71, 72] but also experimentally measured values; including material's surface emissivity required to estimate heat losses by radiation. Thus, a more accurate and closer numerical representation to manufacturing process conditions is desired while keeping a reasonable balance between the significance of the obtained results and the computational resources needed.

1.7. Summary

An overall introduction into additive manufacturing and the electron beam selective melting processes was presented; including previous numerical methods used to represent the physical and thermal phenomena taking place during the additive process, with heat sources of high aspect ratio and volume interaction. Finally a review of the strategy used to solve the thermal heat transfer equation on a three dimensional (3D) domain by a moving heat source using a multiphysics solver is described considering its model assumptions and limitations.

2. Materials and Methods

2.1. Ti6Al4V Powder Material

A Ti6Al4V powder was used in this research work with the designation Ti6Al4V (ELI) Grade 23. ELI, stands for extra low interstitial oxygen ~0.13% content with a lower nitrogen carbon and iron composition percentages. This material was obtained from ARCAM-AB and ASM (American Specialty Metals Inc.). The powder material obtained from Arcam-AB was produced by the gas atomization method. This method entails the melting of a metal wire through an array of plasma torches, after which the molten metal is atomized by an argon gas nozzle and cooled at rates between 10^2 – 10^3 °C/sec during precipitation inside an isolated chamber [73, 74]. Final powder properties can be controlled by adjusting melt temperature and viscosity, alloy composition, metal feed rate, inert gas type, gas pressure, nozzle geometry, gas temperature and residual atmosphere [75].

The powder manufacturing method used on the second powder was the plasma rotating electrode process (PREP); This powder production method consists of a centrifugal process, where the end of a metal bar is melted using helium plasma as a heat source while it is rotated along its longitudinal axis [74]. The molten metal is then atomized by centrifugal forces, and the resulting powder is obtained by quickly cooling (10^3 Celsius/sec) these molten particles in an inert gas environment

[76, 77]. The resulting powder is spherical, with a tap density close to 65% of solid substance. Both powders PREP and GA were evaluated in as-received and recycled condition as well as partially sintered, representing the state of the circumventing material during the build and as well as after the additive process.

2.2. Physical Properties Analysis on Ti6Al4V Powders

Several methods are proposed herein to characterize additive materials like Ti6Al4V, including all processing stages from powder, sintered and solid state. The as-received powder material (PREP and GA) was evaluated throughout the EBSM process to identify possible changes that might affect the numerical model later described. Differences in morphology between PREP and GA powders were examined through SEM analysis as well as the presence of hollow cavities within the powder particles using computed tomography (CT Scan). Gas and liquid pycnometry was used to determine powder porosity volume as well as surface area. Finally, particle size distribution for PREP and GA powders was analyzed using laser diffraction.

2.2.1. Particle Morphology Analysis

Scanning Electron Microscopy (SEM)

A Phenon - G2 Pro desktop SEM system was used for the PREP and GA powder morphology study. For this, a monolayer of powder was placed on an aluminum sample holder and graphite tape was used to improve sample conductivity and to promote adhesion with the powder to the tape preventing the particles from flying off once the vacuum system was in operation.

2.2.2. Density and Surface Area

Density values were evaluated on the powder material to understand how particle packing was affected as a function of temperature, starting from loose to sintered powder. These measurements partially explain factors such as thermal diffusivity, thermal conductivity and overall cooling rates of the built part. For this analysis, gas and liquid pycnometry were used. Additional values for Ti6Al4V in solid and liquid state were obtained from literature [78] and adapted to an interpolation function, together with the data on the powder condition.

Density by Gas Pycnometry

Operation principle

Gas pycnometry consists of the infusion of helium (He) gas into a porous material contained in a known volume. The gas covers the surface of the sample, obeying the Archimedes principle of fluid displacement. The operating principle corresponds to the gas law PV = nRT. Where P is the gas pressure, V is the volume containing the gas, n is the number of moles of the gas, R is the universal gas constant and T is the temperature of the gas. The equipment used in this analysis was a Ultrapyc 1200e, and the following tests conditions were used:

Table 2.1. He Gas pycnometry measurement conditions

Equipment setup	Value
Cell Volume (cm^3)	149.6553
Analysis Temperature (Celsius)	27.7
Target Pressure psi	10
Type of Gas	Helium
Flow Purge (min)	1
Number of Runs Averaged	3

Density by Mercury Pycnometry

Operation principle

Density by liquid pycnometry was performed according to standard DIN 66133. (Determination of Pore Volume Distribution and Specific Surface Area of

Solids by Mercury Intrusion) and consisted of the use of a non-wetting material intruding into the porous sample following the Washburn's equation [79]. The equation (2.1) dictates that the pressure required for the liquid metal to fill up the pores is inversely proportional to the pore diameter allowing the analysis of particle sizes within the range from 0.003μm to 360μm.

$$-\boldsymbol{\pi} D\gamma \cos\boldsymbol{\theta} = \frac{\boldsymbol{\pi D}^2\boldsymbol{P}}{4} \tag{2.1}$$

Where:

D = $Particle\ Diameter$

πD^2 = $Cross\ sectional\ area\ of\ the\ pore\ opening$

γ = $Surface\ Tension$

P = $Intrusion\ Pressure\ (up\ to\ 50\ psi)$

And the relation between applied pressure and the minimum pore size into which mercury will be forced to enter is:

$$\boldsymbol{D} = -\frac{4\boldsymbol{\gamma cos\theta}}{\boldsymbol{P}} \tag{2.2}$$

The system uses a known-volume chamber in which a known sample (powder and sintered material) weight is introduced within the chamber, later pumped down using a vacuum system for sample degassing. After this, the liquid metal (mercury) is introduced to the system until the pressure in the chamber is in equilibrium, and the mercury volume used for pore intrusion is later used to calculate the powder porosity. A low pressure mode 50 psi (345 kPa) was used in this analysis able to attain volumetric resolutions up to 0.1 μL during the mercury intrusion process [80].

Table 2.2. Bulk density measurement setup

Sample and System Properties	GA Powder	PREP Powder	GA Sintered	PREP Sintered
Sample Weight (g)	0.7790	0.5093	0.5773	1.1614
Bulk Sample Volume (cc)	0.2990	0.1959	0.2007	0.4354
Total Intruded Volume (cc/g)	0.1509	0.1573	0.1360	0.1373
Hg Surface Tension (erg/cm^2)	480.00	480.00	480.00	480.00
Hg Contact Angle	140.00°	140.00°	140.00°	140.00°

*Mercury volume normalized by sample weight

Surface Area Measurement by Krypton Adsorption

Operation principle

First created by Brunauer, Emmett, and Teller (BET) in 1938; the surface area by gas adsorption, consists on the determination of the amount of adsorbate liquid or gas required to entirely cover the external and internal surface of a solid material with an adsorbate monolayer. The analysis starts by the insertion of the sample to be analyzed into a known volume cell. The pressure within the cell is decreased and a degassing process takes place at high temperature, in order to clean the inserted sample from any present contamination. Once this operation concludes, Krypton the adsorbate material, is injected at a temperature of 77.3K into the chamber containing the sample. This adsorbate forms a monolayer of atoms over the sample surface and using BET theory[81], the number of molecules required to cover the sample with a monolayer is estimated and the surface area is obtained by multiplying this value by the cross-sectional area of the adsorbate (20.5 Å). Subsequently, the pressure in the chamber rises until the adsorbate completely fills all the pores within the sample and knowing the adsorbate density the total pore volume is estimated[82].

Sample and system setup

Samples from Ti6Al4V PREP and GA material in powder and partially sintered condition, each with a weight of approximately 14 grams were prepared to be later placed within the sample cell for analysis on a *Quadrasorb Si* system. The sample powder contained within the analysis cell was degassed for 3 hours at a temperature of 150°C and the adsorption time used was 200 seconds.

2.2.3. Particle Size Distribution by Laser Diffraction

Operation principle

Laser particle analysis is based on the Joseph von *Franhoufer* model of light diffraction caused by opaque, spherical and non-porous particles. During the evaluation, a specific amount of powder passes through a broadened beam of laser light. This beam is then scattered depending on the particle size traveling in front of it and a particle size distribution is inferred from the angular variation (see Figure 2.1). Diffracted light is higher for small particles than for coarser ones and the resulting pattern is not effected neither by is position nor motion, only causing obscuration or attenuation of the light beam [83].

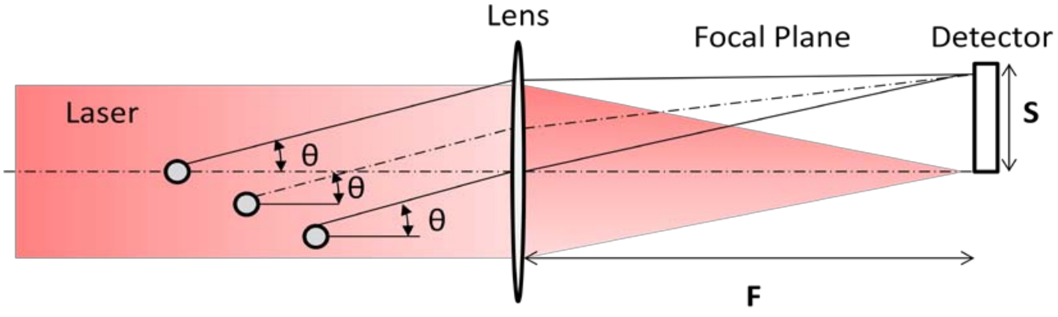

Figure 2.1. Laser diffraction technique (adapted from [84])

Based on *franhoufer's* theory, only the size of the particle will affect its diffraction pattern following equation(2.3), where *r* corresponds to the particle radius, *S* is the distance from the focal plane and λ is the incident laser wavelength

$$\times = \frac{2\pi r S}{\lambda F} \tag{2.3}$$

Sample and system setup

Two different sample dispersion methods (wet and dry) were used to estimate the particle size distribution of PREP and GA powders. The laser diffraction system used for the measurement was a CILAS 1180 for wet analysis, and a Mastersizer 2000 Ver. 5.60 from Malvern Instruments Inc. was used dry evaluation.

The wet mode analysis consisted of the dispersion of 5 grams of Ti6Al4V powder using water as a solvent to ensure the proper particle dispersion, coupled with ultrasound for 60 seconds during the test. Low obscuration values 1.2% (+/- 0.2) was used during the test to guarantee the resolution of small particles, and a total of 5 samples were measured during the analysis.

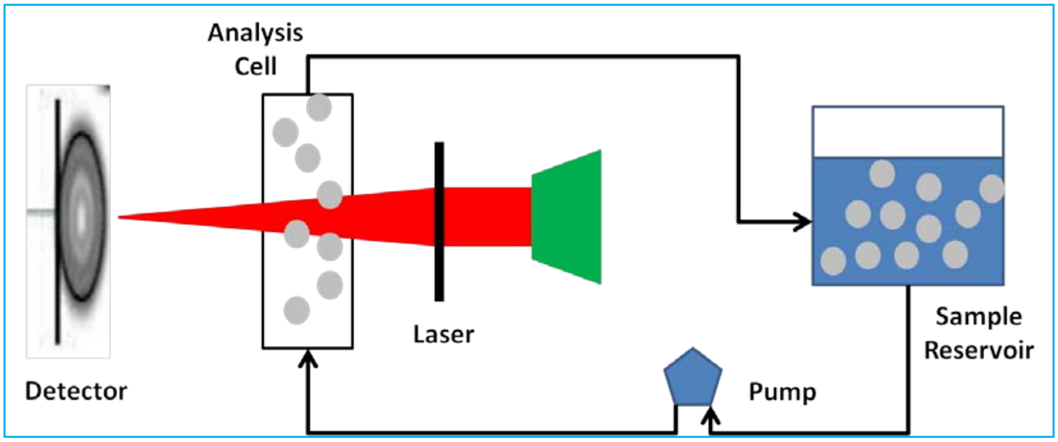

Figure 2.2. Wet dispersion system *Cilas 1800* using a 5gms sample size and obscuration of 1.2%

Dry analysis was performed by dispersion of 250 grams of PREP and GA powder to ensure a representative sample quantity. A high-pressure compressed air stream was used to disperse the particles that later were transported through the light detector. Since the instrument operation depends upon obscuration and not the mass of the sample, a total of 158 tests were necessary to use all 250 grams of powder. To analyze each sample, a small amount of powder was placed onto the sampling tray using a vibration feed rate of 75%, and the dispersive air pressure was set at 4 bar. Nitrogen was used as the analysis medium.

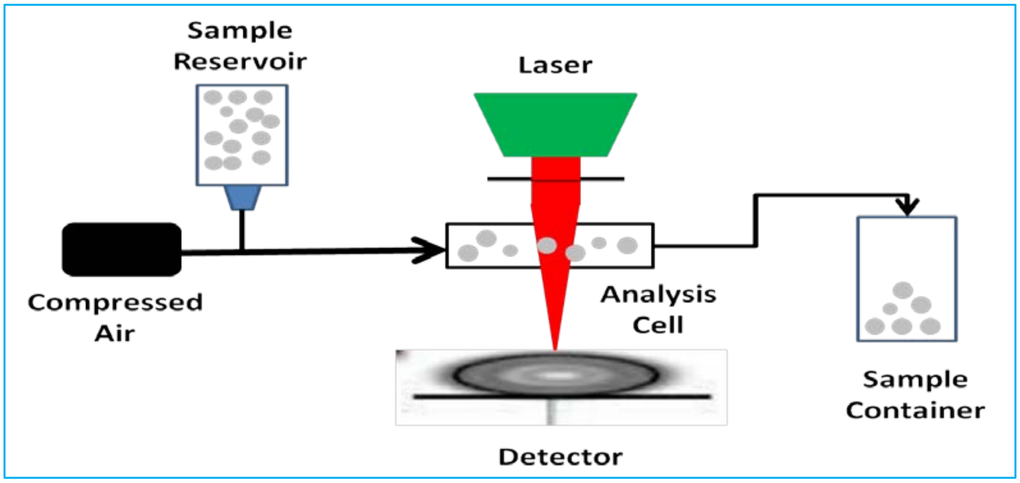

Figure 2.3. Dry dispersion system *Malvern 2000* using a 250grams sample size and obscuration values of 3.91%

2.2.4. 3D Profilometry by Axial Chromatism

Non-contact profilometry has been used to measure the different surfaces involved during the EBSM process, mainly in the case of powder material, where its weak cohesion make it very difficult to measure with conventional contact (stylus) methods. The method used here was 3D optical profilometry using a Nanovea ST400 3D Profilometer. Thanks to its operation principle (axial chromatism), a reliable measurement of rough and non-reflective surfaces is possible without the artifacts and software data manipulation limitations present on light interferometry; offering direct measurements on the surface in focus at higher angles (up to 80°) at the same speed as interferometry, and at lower cost.

Operation principle

The system's operating principle is based on the refractive index change due to changes in wavelength caused by a diffraction grading. Each wavelength is then used to find a focal point in the surface to generate an image, and the remaining wavelengths (out-of-focus) are canceled during the filtering process. Within the measurement range no height correction must be made and a single monochromatic point is always in focus to construct the image [85].

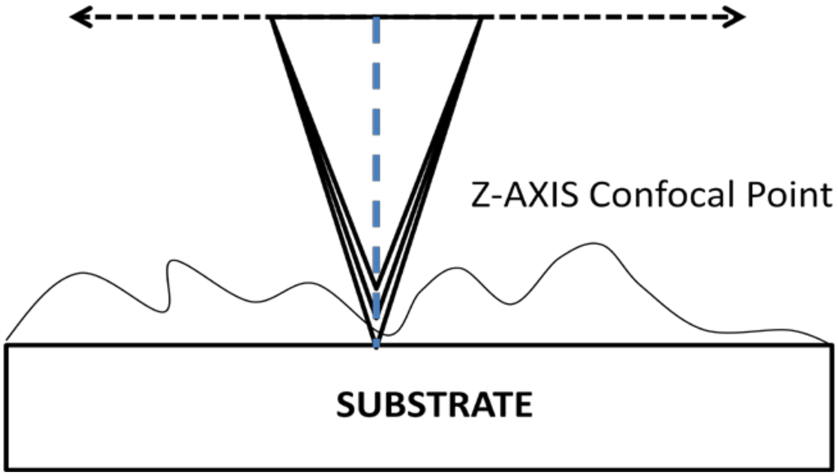

Figure 2.4. Axial chromatism operation principle (adapted from [85])

Profilometry measurements were taken with the purpose of correlating the effect of roughness on emissivity values, and to document the EBM processed part surface finish at specific powder size distributions. The surfaces measured included the pressureless sintered powder circumventing the built, the melt (smooth) surface area in line-of-sight of the electron beam and the surface between the solid part built and the surrounding loosely sintered powder.

<u>Sample and system setup</u>

The samples used for this test consisted of an EBSM manufactured solid cube made of Ti6Al4V (1” cube) using PREP powder, where the faces to be measured were labeled (Face 1 and Face 2). Additionally a partially sintered Ti6Al4V PREP powder sample was prepared with 0.75" in diameter and 0.25" thickness.

Figure 2.5. Image of solid Ti4Al4V (left) and sintered TiAl4V (right) used for 3D roughness analysis

Probe specifications and system measurement setup are specified in Table 2.3 and Table 2.4.

Table 2.3. Probe Specifications 3D Profilometry

Sample	Ti6Al4V Solid	Sintered PREP Powder
Measurement Range	1100µm	3.0 mm
Z resolution (nm)	25	75
Z Accuracy (nm)	200	400
Lateral Resolution (µm)	1.55	2.6

Test conditions:

Table 2.4. 3D Profilometry Test Conditions

Test Specifications	Cube Face 1	Cube Face 2	Sintered Powder
Probe (um)	1100	1100	3
Acquisition rate (Hz)	2000	2000	200
Averaging	1	1	1
Measured surface (mm x mm)	27.0 x 27.0	27.0 x 22.0	27.0 x 27.0
Step size (μm x μm)	10 x 15	10 x 15	25 x 50
Scanning Mode	Constant speed		

2.2.5. Micro Computed Tomography

Computed tomography was initially used as inspection technique on metrology activities for additive manufacturing parts for medical use and is a non-destructive, cost effective and flexible alternative to partial sectioning processes[86]. But, metrology is not the only capability of computed tomography; defect analysis (porosity) has become an area of special interest for this technology. However, the use of this technique for porosity analysis requires the use of an adequate system setup and a higher resolution compared with the currently used for metrology purposes having as a result a new line of products called micro and nano x-ray scanners.

Conventional methods for residual pore analysis in additive parts like partial sectioning (consisting of slicing the material and using an electron beam microscope system for imaging) has been previously used, proving to be time consuming and destructive to the inspected sample, allowing flexible technologies like micro computed tomography to occupy its place with optimum results.

Operation Principle

Also known as Micro-CT scan; this technique involves a dynamic 2D projection around a single axis of rotation of an object placed on a sample table holder using an X-ray source. The 2D projection is then digitally processed by reconstruction calculations to generate cross-sectional images (see Figure 2.6). Finally, 3D CT data is rendered as *voxels* (volume element) with three-dimensional resolution from a few micrometers.

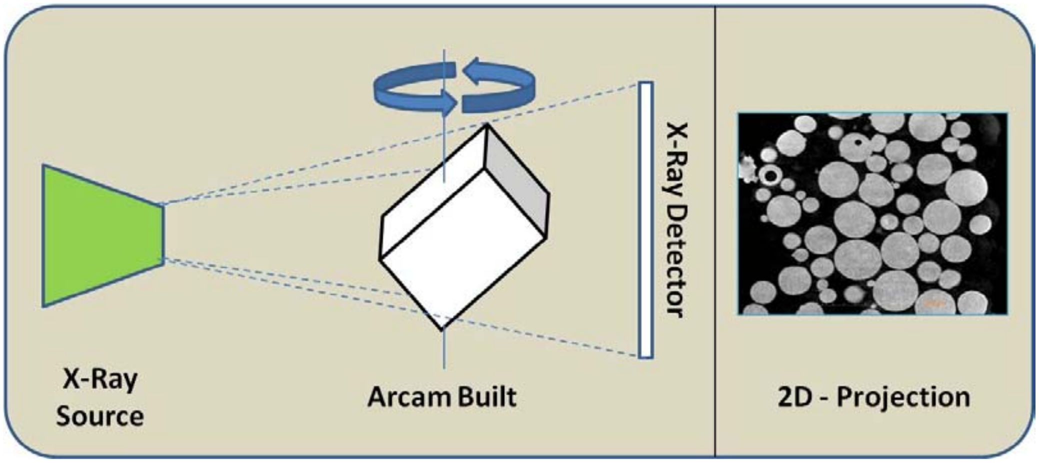

Figure 2.6. Micro-CT Scan setup

The X-ray projection principle is based on Beer's Law (2.4) denoting the x-ray signal reduction as a function of the energy path length and its linear attenuation coefficient,

$$I = I_0 \, e^{-\int \mu(x) dx} \tag{2.4}$$

and considering the effect of the part thickness to be inspected:

$$I = I_0 \, e(-\mu L) \tag{2.5}$$

where I_o is the intensity of the incident X-ray beam, I is the X-ray intensity at a distance $\boldsymbol{L}$ from the source, and $\boldsymbol{\mu}$ is the linear attenuation coefficient of the metal measured in cm^{-1}. The attenuation coefficient depends on the specific density of the material, the element atomic number, and the X-Ray beam energy used for the analysis. After the projection data is collected, a comprehensive algorithm is used for 3D reconstruction and final imaging of the object.

Sample and test setup

Three sample types were used in this analysis; PREP (plasma rotating electrode powder) and GA (gas atomized powder), both in a sintered state and a 1" square Ti6Al4V cube produced using PREP powder material, as later described in Table 2.5. The equipment used in this analysis consisted of two micro computed tomography systems for defect analysis, consisting on an X-Radia's (VersaXRM-500) and North Star Imaging (X-View model X-50).

Table 2.5. CT micro scan analysis matrix

Material condition	Analysis	Equipment used
PREP (sintered)	Powder particle inner porosity and particle necking	Xradia VersaXRM-500
GA (sintered)	Powder particle inner porosity and particle necking	Xradia VersaXRM-500
PREP (solid)	Porosity analysis	Xradia VersaXRM-500 NSI X-View model X-50

Table 2.6. Setup Conditions used on Versa XRM-500

Sample Name	PREP (sintered)	GA (sintered)	PREP (solid)
Source settings (kV/W)	70/6	70/6	150/10
Voxel size (μm)	0.54	0.54	30
Start and end Angle	[-180,180]	[-180,180]	[-180,180]
Number of Views	2000	2000	5000
Time Per View (sec)	5	8	4
Total Acquisition Time	3Hrs 40 mins	5Hrs 20 mins	7.5 Hrs
Field of View FOV (mm)	0.5 x 0.5	0.5 x 0.5	30 x 30

Table 2.7. Setup conditions used on NSI X-View model X-50

Equipment Specifications	**Scan A**	**Scan B**
Source Settings:	Microfocus X-Ray source (XRayWorX)	Microfocus X-Ray source (XRayWorX)
Voltage:	220 kV	205 kV
Current:	93 µA	168 µA
Focal spot size:	20 microns	34 microns
Voxel Size	25 microns	20.4 microns
Detector:	Varian [1536x1920]	Perkin Elmer [2048x2048] [XRD 1620/1621 AM/AN]
Pixel pitch:	[127 x 127] microns	[200 x 200] microns
Framerate:	1.2 fps (833.333 ms integration time)	1 fps (999.911 ms integration time)
Flip:	Horizontal	Horizontal
Rotation:	270 degree	270 degree
CT Scan:		
Type:	Step	Step
Number of frames averaged:	4	4
Number of projections:	1440	1800
Analysis duration:	1h46m	2hours 29min

2.3. Thermal Properties of Ti6Al4V Powder and EBSM Processed Parts

Thermal properties for Ti6Al4V material in powder, sintered and solid state were evaluated to be used as a model input for the heat transfer simulation of the EBSM process. Temperature dependence ranges from room temperature to1600 °C were used to measure heat capacity and thermal diffusivity to finally calculate the thermal conductivity of this additive manufacturing material.

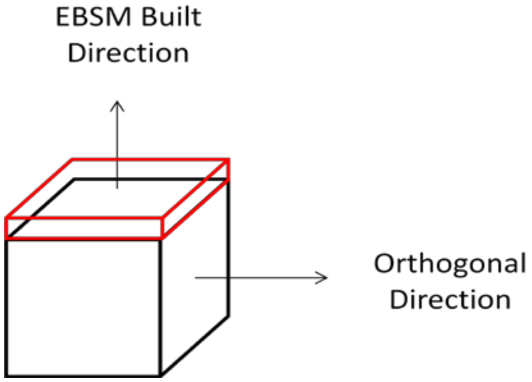

Figure 2.7. Sample orientation illustration used for thermal analysis on Ti6Al4V solid parts

Solid samples prepared for the thermal analysis were cut parallel to the built direction, since it is the main source orientation for heat losses due to the poor heat conductivity expected from the powder material circumventing the solid built.

2.3.1. High Temperature Differential Scanning Calorimetry (HT-DSC)

Operation Principle

The heat capacity is defined as the quantity of heat necessary to raise the temperature of a system or substance at constant pressure by one degree Celsius. Changes on heat capacity of a metal object of a known mass is measured by the difference of heat flux required to raise the temperature both the sample and a reference material as a function of temperature according to equation (2.6).

$$C_p(T)_{sample} = \frac{m_{ref}}{m_{sample}} \times \frac{DSC(T)_{sample} - DSC(T)_{base\ line}}{DSC\ (T)_{ref} - DSC(T)_{base\ line}} \times C_p(T)_{reference} \tag{2.6}$$

where C_p corresponds to the heat capacity the sample and the reference material given on (J/g.K) units; m corresponds to the mass in milligrams (*mg)* for sample and reference material, and DSC corresponds to the signal obtained from the system corresponding to sample, reference and base line test.

Continuous measurement of heat flux as the temperature progresses depends on the material state and phase. Therefore, changes in the amount of heat flux required to maintain the preset rate of heating is shown as endothermic or exothermic events. When the amount of necessary heat flux increases (i.e. in cases like melting and solid-liquid reactions) the event is considered endothermic; on the contrary when the needed heat flux is lower than the setup value (i.e. in cases like solid-solid transitions and crystallization), the signal present itself as an exothermic occurrence.

Sample and system setup

Samples used for this test consisted of PREP and GA powder Ti6Al4V material on as-received (never used) and recycled condition as well as solid samples produced by both powder types later processed by EBSM, which characteristics are later described in chapters 3 and 4. A 2.5µl volume was used for the powder and sintered material and 20µl for the solid samples. Solid PREP and GA Ti6Al4V disks were machined to fit 5mm in diameter and 1mm thickness and both type of samples were contained on a platinum (Pt/Rh, 30µl volume) crucible holder.

Specific heat capacity was measured using a power compensated DSC 404 -F1 *Pegasus*®- differential scanning calorimeter from NETZSCH instruments. Different form conventional heat flux -DSC systems, where both samples are heated by the same plate, the compensated heat flux system is composed by independent heating systems for sample and reference materials allowing additional energy to be applied to or removed from one or both of the calorimeters to compensate the energy change occurring in the sample when an exothermic or endothermic event occur. In this way the heat flow is measured in a more direct manner compared to conventional DSC were the heat capacity measurement is obtained indirectly from temperature differences between sample and reference materials as previously described in equation(2.6).

Additionally, the system was equipped with a platinum-rhodium furnace capable of operation from -150°C to 1650°C and is vacuum-tight, so samples could be tested under purely inert, reducing, or oxidizing atmospheres, as well as under vacuum. Instrument control and data acquisition are accomplished via a 32-Bit MS®-Windows™ Proteus® software and electronics system.

Data evaluation was carried out by a comprehensive PC software package that allows computation of peak and onset temperatures, inflection points, partial area integration, specific heat and transformation energetic. The DSC 404 C can be operated in accordance with national and international standards such as ASTM C351, D3417, D3418, D3895, D4565, E793, E794 and E1269, as well as DIN 51004, -51007, -53765, -65467, DIN EN 728, JIS R 1672 and ISO 10837, -11357, -11409 and the test setup is described in Table 2.8.

Table 2.8. Differential Scanning Calorimetry measurement setup using DSC 404 F1Pegasus®

Temperature program	Heat RT-1600°C, 20 K/min
Purge Gas / Flow rate	Argon / 60 mL/min
Sensor	DSC type S
Crucible	Pt-Rh with alumina liners and pierced lids
Sample Masses (mg)	
PREP Powder (as-received)	45.31
PREP Powder (recycled)	46.92
GA Powder (as-received)	40.77
GA Powder (recycled)	41.64
Solid PREP	58.41
Solid GA	62.43

2.3.3. Laser Flash Analysis (LFA)

Operation principle

Laser flash is a thermo analytical method, consisting on the heating of a disc-shaped sample on one of its sides using a laser pulse and measuring the increase in temperature caused by the absorbed energy on the opposite surface (see Figure 2.8). The laser beam shape is circular, with a spot size diameter of 12.7 mm, procuring a uniform intensity to generate a uniaxial heat flux perpendicular to the surface of the sample. Thus, the resulting rear-face temperature rise is recorded and analyzed to calculate the thermal diffusivity of the material whether it is in powder, sintered, or solid form[87].

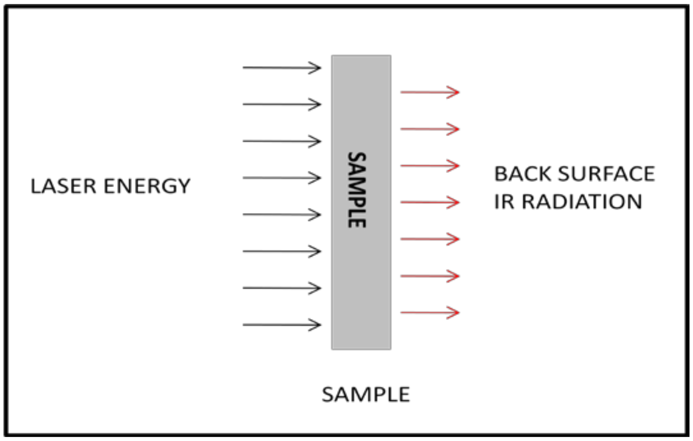

Figure 2.8. Laser flash operation principle

Thermal diffusivity

The thermal diffusivity α indicates the material's ability for heat propagation by conduction when the temperature change with time (transient process); this property is measured by the ratio between the sample area L^2 and the half-time ($t_{1/2}$) required for a laser pulse created by the laser flash system to increase the sample temperature from the baseline to an specific analysis temperature. This property has a dimension of area over time expressed in m^2/s as seen in equation(2.7).

$$\alpha = 0.13879\,L^2 / t_{1/2} \tag{2.7}$$

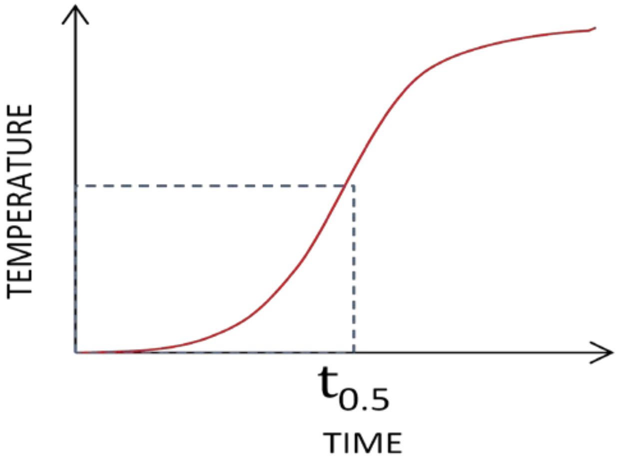

Figure 2.9. Half time temperature pulse calculation

Thermal conductivity

Thermal conductivity is the quantity of heat transmitted as a result of a temperature gradient with a direction normal to the surface and is calculated by,

$$\lambda = \alpha \, Cp \, \rho \tag{2.8}$$

where λ is the thermal conductivity, α is the thermal diffusivity, C_p the sample heat capacity, and ρ the sample density.

Sample and system setup

An LFA 427 system was used to calculate the thermal diffusivity based on the thermal laser flash method conducted according to standard test ASTM E 1461-11. Two type of samples with replicas *(n=2)* from PREP and GA Ti6Al4V as-received powder, and EBSM processed solid condition, were prepared for this test with 12.7 mm diameter size and 2 mm thickness. The system heat source for diffusivity measurements was set with a laser pulse power of 2.1kV and a pulse width of 0.5 µs.

2.3.4. Remote Infrared Temperature Measurement (IR)

A remote infrared temperature measurement (IR Camera) system was used to measure powder and solid Ti6Al4V material contained in a vacuum system to calculate its respective emissivity value depending on temperature (see section 2.3.6). These values will be later used as a part of the heat losses by radiation to correct the model and simulation representing the EBSM process.

Operation principle

Remote temperature measurement is possible through the detection of infrared energy emitted from all objects at temperatures above the absolute zero energy (0°K). This radiated energy is later converted into a thermal image of the object being surveyed [88].

System setup

The temperature system used here consisted of a FLIR SC5600-M camera using a Indium antimonide *InSb* photovoltaic sensor, operating on the 2.5 - 5.1 micron waveband range. Since the measurement range for the emissivity evaluation exceeds the 300°C, neutral density germanium filter (0.3 O.D with 25mm diameter), spectrally flat between 2-14 microns, was used inside of the camera to attenuate the signal enabling the temperature reading up to 1000 °C.

2.3.5. Fourier Transform Infrared Analysis (FT-IR)

Since the remote temperature measuring process for emissivity calculation took place inside of a vacuum system to replicate the EBSM process, the use of a suitable view port transparent in the infrared study range was necessary. Thus a quartz window was chosen in terms of availability and its infrared trasmissivity was measured using the FT-IR technique. Furthermore the data obtained was later used to calibrate the remote temperature setup.

Figure 2.10. Nicolet 8700 FT-IR System

The system used for the measurement was a Thermo Electron Nicolet 8700 FT-IR spectrometer, with an spectral wave number range between 7800 to 350 cm^{-}1 (equivalent wavelength range 1.28 – 28.57.43 microns). Once the sample was placed on the detector, a total of 32 scans were performed with a laser wavenumber of 15798.3 cm $^{-1}$ (632.99 nm) in the range between 1000 and 5000 cm^{-1}.

2.3.6. Emissivity measurement

System setup for Ti6Al4V emissivity calculation

A vacuum system was used to mimic the low pressure environment present inside of the EBSM chamber during the build. A graphite heater was used to heat the samples up to 800°C (Figure 2.12.f), since common built temperatures used on Ti6Al4V are in the range of 625 to 700°C [17].

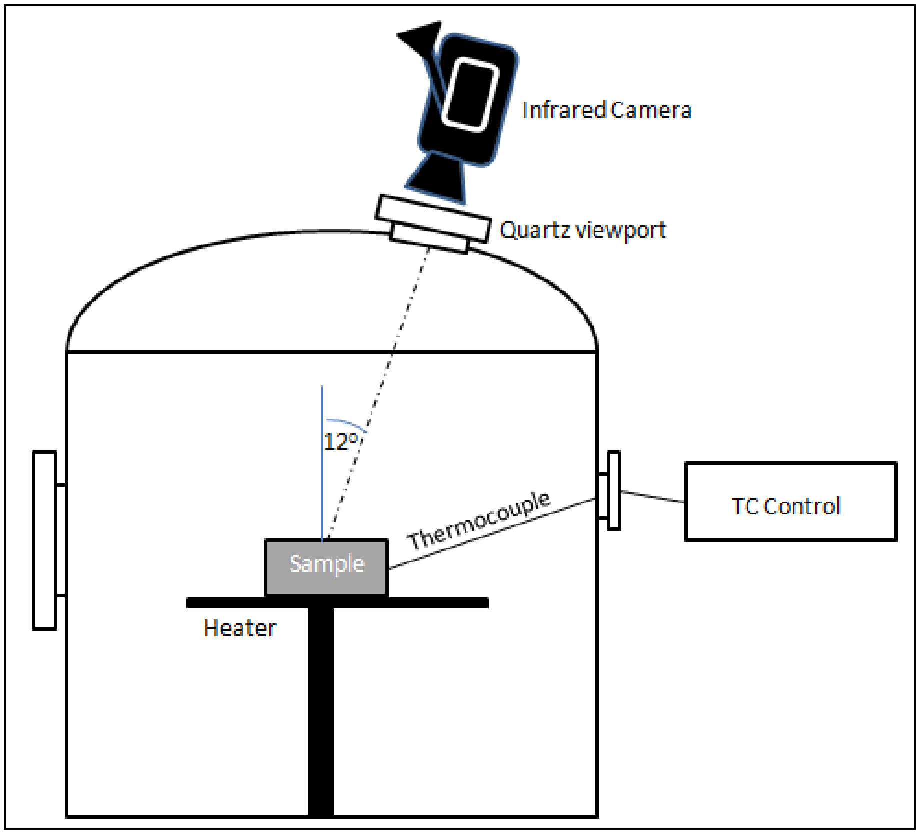

Figure 2.11 Vacuum setup for emissivity measurements

The vacuum system was equipped with a quartz viewport, through which the infrared camera could view the test sample. The standard deviation of the temperature measurement from the FLIR SC5600 infrared camera is approximately 1°C within the range of analysis.

EBSM solid parts made out of PREP and GA powder were sectioned and its surfaces (smooth surface caused by the e-beam melting and rough surface created by the contact with the circumventing powder during the built Figure 2.12. c through e) were partially coated with graphite to serve as a black body radiation reference point.

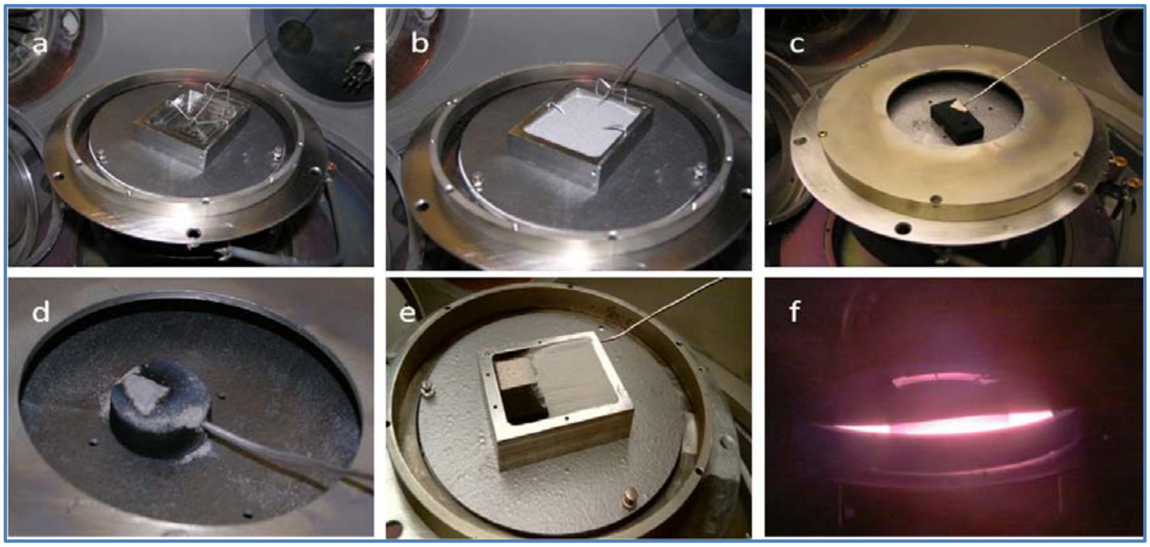

Figure 2.12. Emissivity sample setup: a. EBSM processed Ti6Al4V holder; b. Ti6Al4V powder; c. Solid Ti6Al4V partially coated with graphite; d. Sintered Ti6Al4V powder; e. Powder and partially graphite coated rough Ti6Al4V solid; f. Side view image during sample heating.

An EBSM solid block (manufactured using Ti6Al4V PREP powder material) was properly machined to fit the samples and ensure a uniform heating surface while containing the powder material (see Figure 2.12a. and b). A quartz window was chosen for its vacuum compatibility and spectral concordance to the camera range and operating temperature[88]. Additional calibration was required on the viewport window used to remotely measure the temperature, since a flat IR transmissivity in the range of 0.1 – 3 microns in wavelength was necessary. It was found the window was not entirely transmissive to infrared radiation (see Figure 2.13) within the evaluation range and further calibration was necessary using a black body (BB) radiation correction protocol.

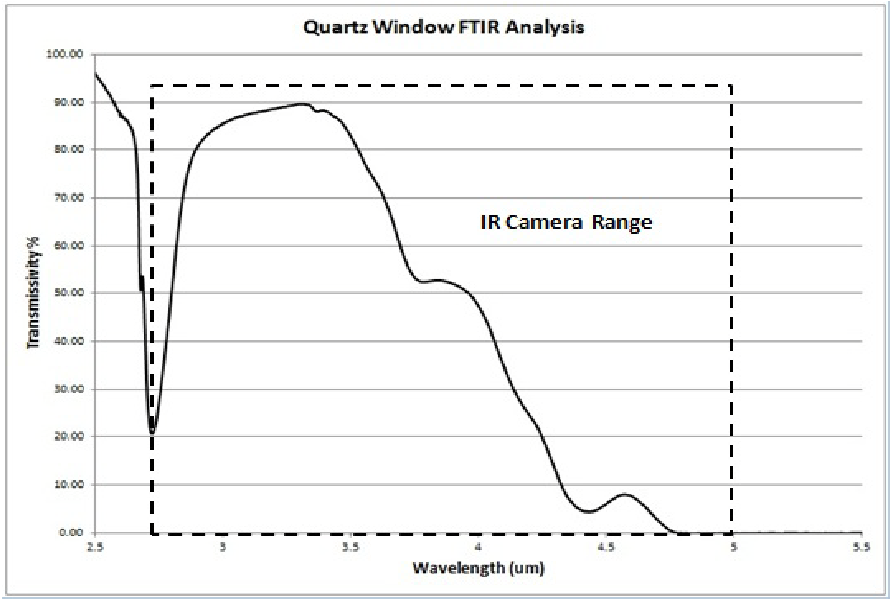

Figure 2.13 FTIR Analysis on Quartz window

Figure 2.14. Viewport correction setup

The view port spectral calibration consisted on the infrared temperature measurement of parts coated with graphite (for maximum emissivity results) with and without using the view port (see Figure 2.14) to create a correction curve as previously described by *Xu and Fisher* [89] and depicted in Figure 2.15. Data was obtained from room temperature up to 300°C and a linear polynomial solution correlating the data was later used to extrapolate the data up to 1000°C.

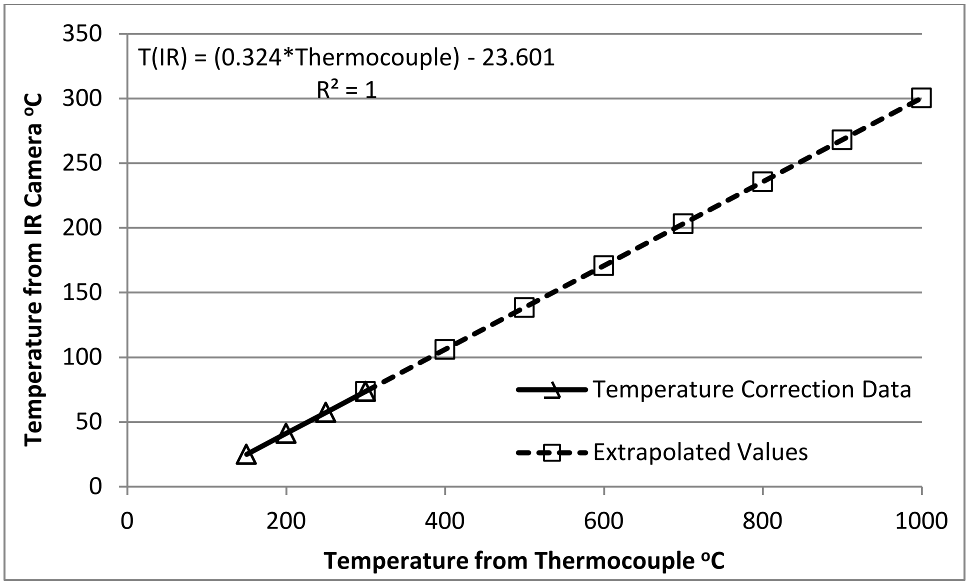

Figure 2.15 **Thermal Camera Calibration with black body source behind Quartz window**

Figure 2.15 shows the calibration result with a blackbody (BB) source behind the quartz window. The temperature reading from the camera is linear with the actual temperature, and this characteristic has been verified with different surfaces both in air and in high vacuum environments. Once the calibration was performed, the data provided by the IR camera was corrected and the emissivity values were estimated as seen in section 4.4.

2.4. Ti6Al4V Sample Preparation EBSM Process

A sample was manufactured with the EBSM system using PREP powder Ti6Al4V material with the sole purpose of being used to mimic and describe average process conditions, later used during the modeling and simulation validation step. The resulting surface finishing and volumetric porosity was also evaluated in these samples as seen in section 4.4.

An A2 EBSM system from Arcam-AB was used to build a 1”x1”x1” part. First, PREP powder was loaded on the powder hoppers and the system was closed to initiate the chamber cleaning by vacuum degassing until an ultimate pressure of 3.4×10^{-3} mBar was reached. Later on, the build plate is preheated (stainless steel) to a temperature of 500°C for 10 minutes for degassing. After the degassing was complete, the heating of the build plate continues until it reached a final value of 734 °C, which is called the start build plate temperature. The powder is then dispersed by the raking system (see Figure 2.16) back and forth 3 times in 7.5 seconds. The powder heating measured time was 10.5 seconds, changing its orientation 90° degrees for each layer.

Figure 2.16. EBSM Powder Raking System

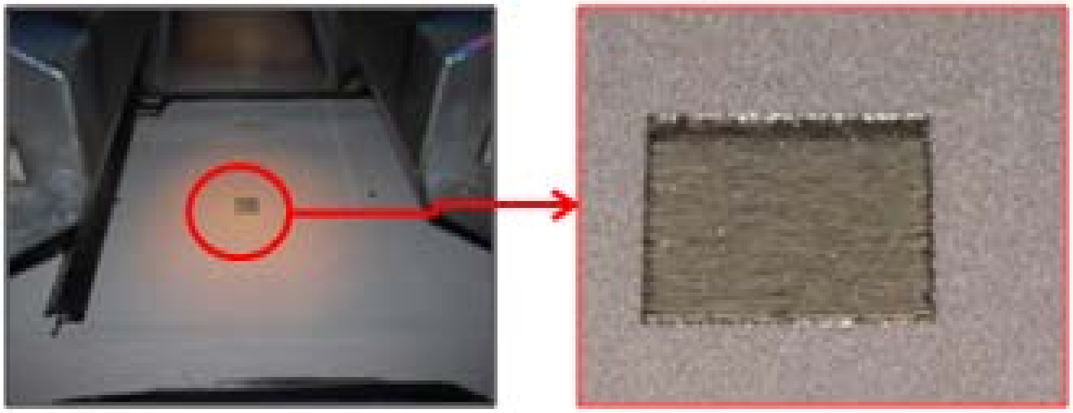

Figure 2.17. Cube built image (PREP powder) after being processed by EBSM. Sample is embedded in PREP powder material.

Finally the part contour and internal volume of the layer is melted in 7 seconds, yielding an average build time per layer of 25 seconds in 254 layers, for a total build process time of 2.2 hours including the pre-heating stage.

Figure 2.18. EBSM processed Ti6Al4V cube sample from PREP powder

The recorded e-beam scanning speeds ranged between 223.7 – 1077.3 mm/s, with an overall measured temperature at the bottom of the build plate in the range of 608 – 668 °C. Electron beam acceleration voltage corresponded to 60kV with 37.5 mA of maximum beam current feedback.

2.5. Summary

Density measurements for powder and sintered material were conducted using gas and liquid pycnometry. Laser flash diffraction was also used to determine particle size distribution similarities or differences between powders produced by the GA or PREP method. Finally thermal properties such as heat capacity, thermal diffusivity and the evaluation of the thermal conductivity by direct and indirect methods were reviewed as well as a comprehensive setup representing the vacuum environment of the EBSM for emissivity coefficient evaluation for further radiation losses calculation. All these techniques will contribute to the material data currently available on Ti6Al4V for additive manufacturing purposes.

3. Physical Characterization of Ti6Al4V Powder Material for EBSM Use

The success of any powder based metallurgical process such as EBSM, strongly depends on an optimum characterization and control of the metal powder used, and their method of production; these will ultimately control the resulting particle microstructure, chemical composition, shape and size distribution [90], affecting the way the powder behaves during the EBSM process sintering.

For example, in powder bed processes like EBSM, the use of powder with spherical morphology and high packing density conferring good flow properties is desired to ensure a uniform part build. Even though the particle shape is a common feature in the powder (spherical or irregular shape), a particle size distribution exists and it changes depending on the production process, influencing the EBSM build part resolution capability and surface finishing. For these reasons, the effect of the powder manufacturing process PREP versus GA on the final physical properties for Ti6Al4V was conducted here, considering the available information is scarce if non-existent [91], however is essential for the development of predictive thermal modeling and simulation.

Previous thermal models on the EBSM process have only considered cast and wrought temperature dependant physical properties in bulk condition [78]; disregarding the properties of the powder surrounding the part while it is being manufactured. This powder is subject to physical changes from loose particles to *pressureless* sintered, to melted and finally solidified; additional characteristics to consider includes the powder production method, particle morphology, particle size distribution, powder and inner particle porosity and powder surface area. These factors will further have an influence on thermal properties affecting the way heat is transferred during the EBSM part manufacturing, finally controlling its microstructure and end-product properties.

3.1. Powder Particle Morphology

During the EBSM process, the powder is spread by the raking system (as previously seen on Figure 2.16) and its uniform distribution is a key characteristic to ensure high build rates and part accuracy. The main characteristic to meet this purpose is to use a powder with high flowability. This property improves significantly with factors such as particle sphericity, (for what the use of irregular shaped powders particles is not desired), powder packing and compressibility. Thus the powder particle morphology is an important factor to be considered in additive manufacturing affecting processing factors such as flowability, powder packing and ultimately heat transfer process conditions.

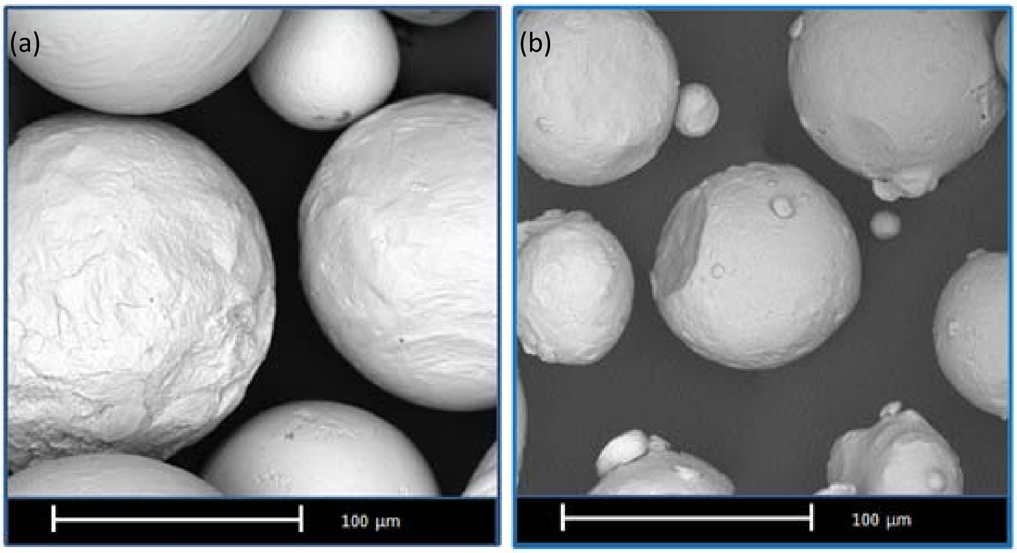

Figure 3.1. SEM images PREP (left) GA (right)

As observed in Figure 3.1, gas atomized powders as well as plasma rotated electrode powders are spherical in shape. Spherical particles (see Figure 3.2) promote higher packing densities and a uniform powder bed. This increases part build consistency and faster build rates. The only distinct feature observed between the two powder materials, consisted in smaller particle sizes and satellite particles attached to the gas atomized powder [92]. Satellite formation is attributed to the interaction between both coarse and fine particles as a result of the turbulence on the gas atomization process creating particle-particle collision and partial welding interaction on the solid state [93, 94].

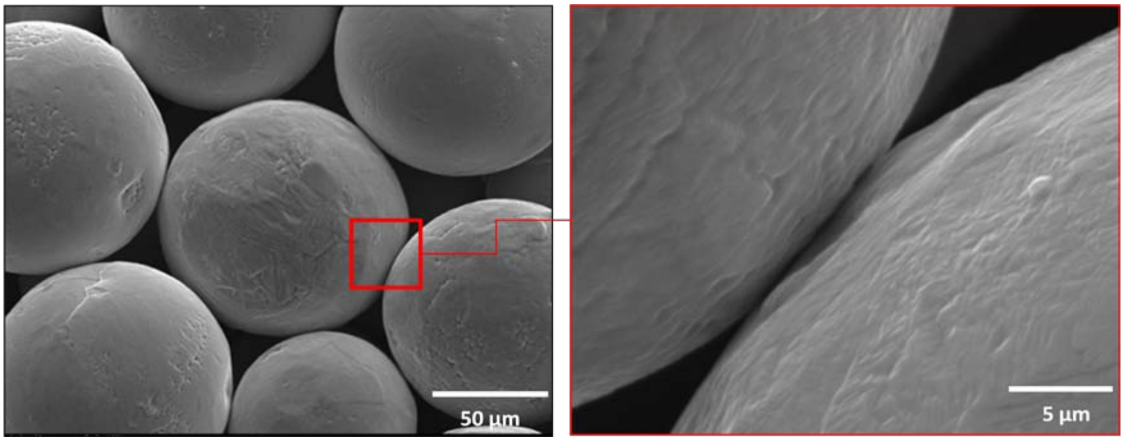

Figure 3.2. Ti6Al4V PREP powder contact surface SEM image

3.2. Powder Particle Defect Analysis

In the present study, powder material in a sintered state was evaluated using micro computed tomography (see Table 2.6). Micro-CT scans for powder and EBSM as-built part characterization was chosen over partial sectioning for being a non-destructive inspection technique, as well as for its ability to inspect large volumes. Another limited trend with partial sectioning arises when shape evaluation of porosity is conducted, due to the defect-polishing direction relationship, which can create inaccurate shapes, making the defect source identification difficult.

For this analysis, partially sintered powder was produced by replicating the temperature signature obtained from the (EBSM) process itself, to better understand the level of sintering and particle contact. Both GA and PREP powders were *pressureless* sintered, using a surrogate vacuum system described in section 2.3.4, and using an EBSM-produced solid part as a container as described in Figure 2.12. b.

As seen from the computed tomography image rendering process in Figure 3.3 and Figure 3.6, the presence of internal hollow cavities in both PREP and GA powder particles is apparent. Similar findings have been previously shown on gas atomized powders [95] of steel and aluminum alloys and Inconel 718 [96], showing the susceptibility of the GA powder to inert gas entrapment during the solidification process.

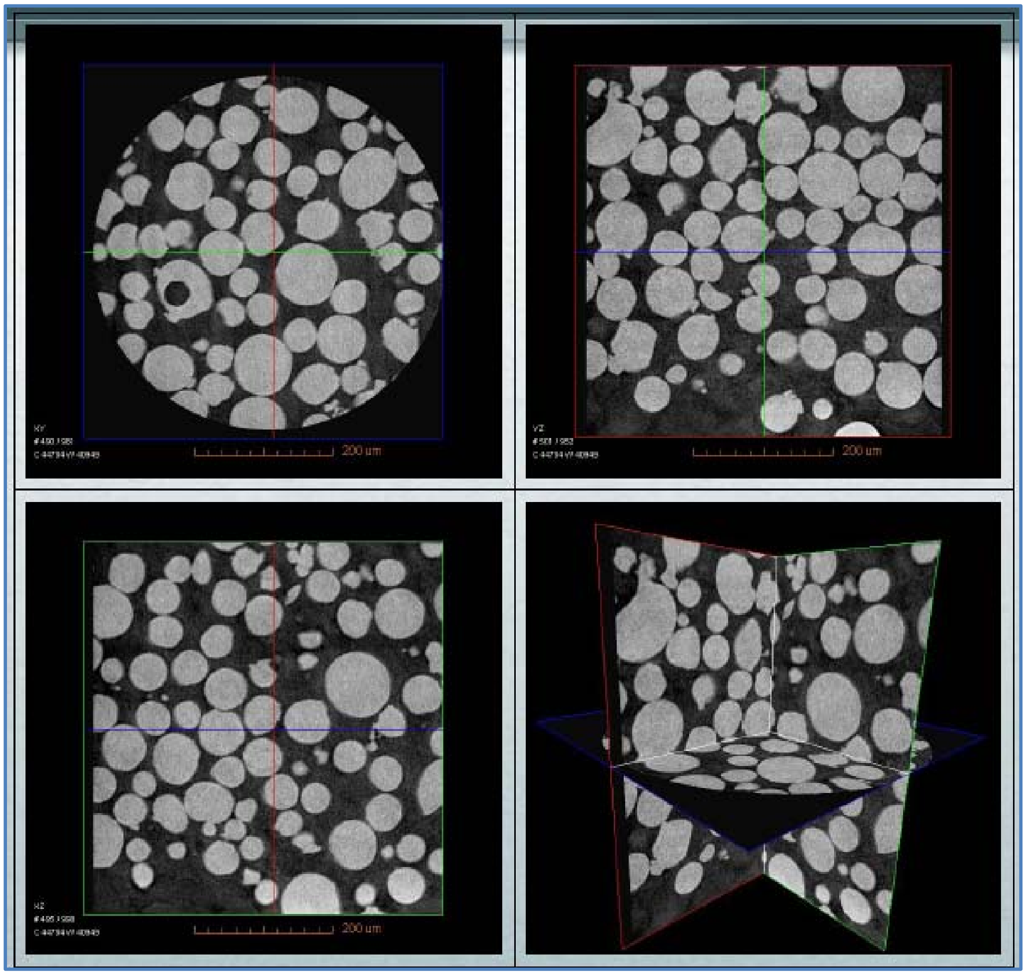

Figure 3.3. **Computed tomography images. Reconstructed 2D slices from sintered Ti6Al4V (GA) powder. Each of the quadrants represents a different orthogonal virtual slice. The colored lines correspond to slices with the same border color.**

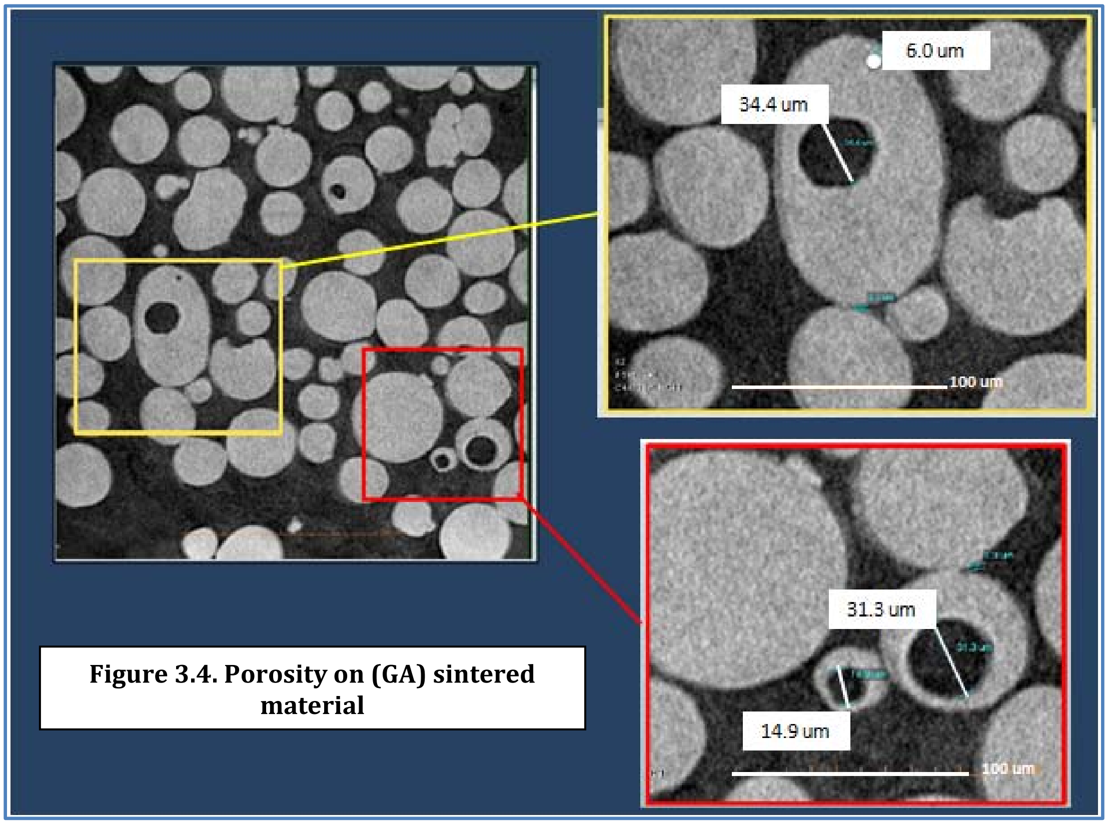

Figure 3.4. Porosity on (GA) sintered material

Particle inner porosity size range was found between 5 to 40 microns in diameter (see Figure 3.4) on the GA sintered powder and no correlation between particle size and porosity was observed in the samples prepared.

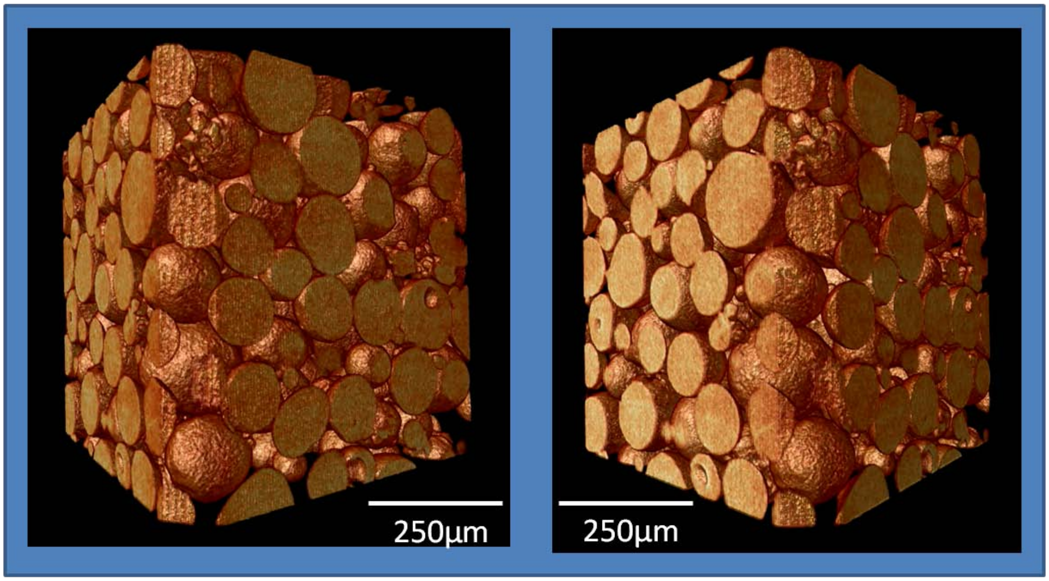

Figure 3.5. 3D volume rendering on Ti6Al4V sintered GA powder material

On the other hand previous data from PREP powder supports the fact that particle porosity is present to a lesser degree compared to gas atomized powder particles, enabling the build of solid parts with less porosity if the right process conditions are applied [97]. *Zhao* and *Zheng* [97, 98] presented the same findings for gas entrapment on Inconel produced by gas atomization, but no evidence of this defect was ever found on PREP powder, leading to a conclusion that the plasma rotated electrode process will not produce this type of particle defect, or at least the inner porosity is present to a lower degree than in the gas atomized processes, facilitating a low-porosity part.

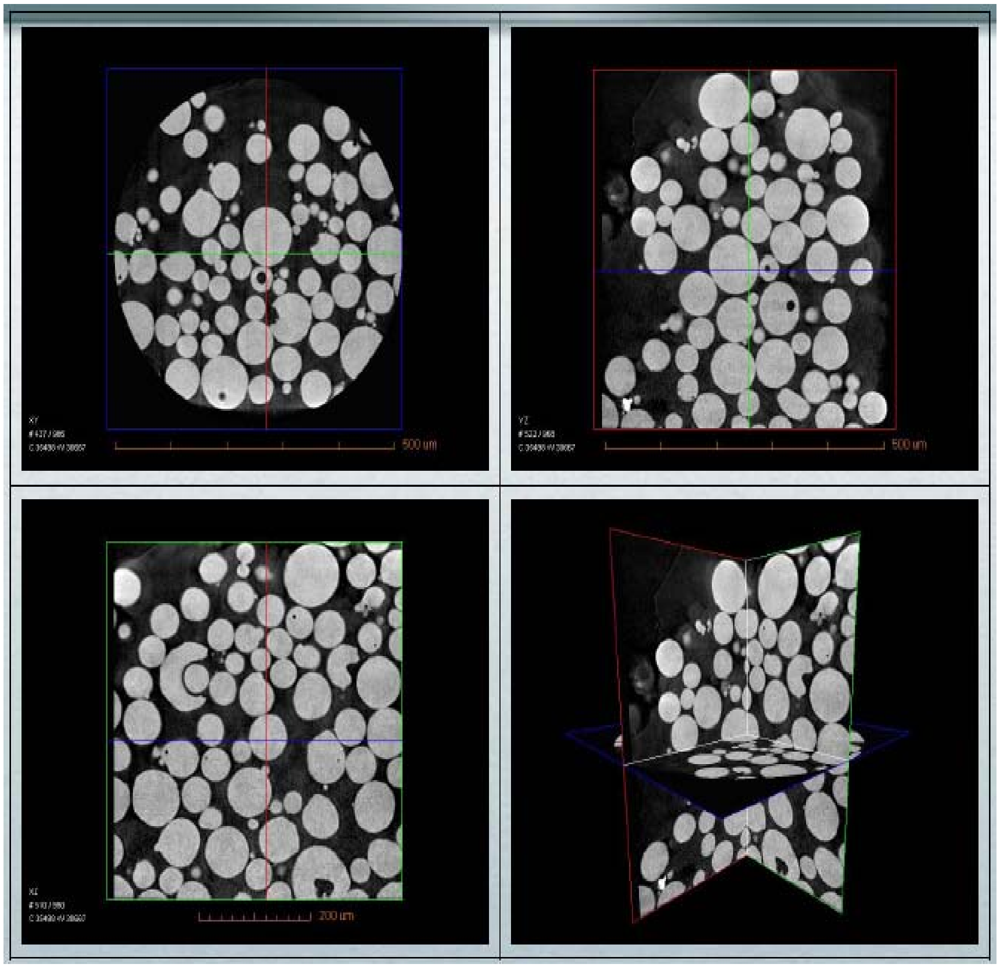

Figure 3.6. Reconstructed 2D slices from sintered Ti6Al4V PREP powder. Each of the quadrants represents a different orthogonal virtual slice. The colored lines correspond to slices with the same border color.

Figure 3.6 showed the random distribution of the particles pores with no specific location or size; a closer look to the cross sectional images in Figure 3.7 reveals inner porosity values in PREP sintered powder ranging from 2 to 20 microns.

Despite the fact that porosity is present on PREP powder; the observed pore diameters were smaller than those obtained with GA powder.

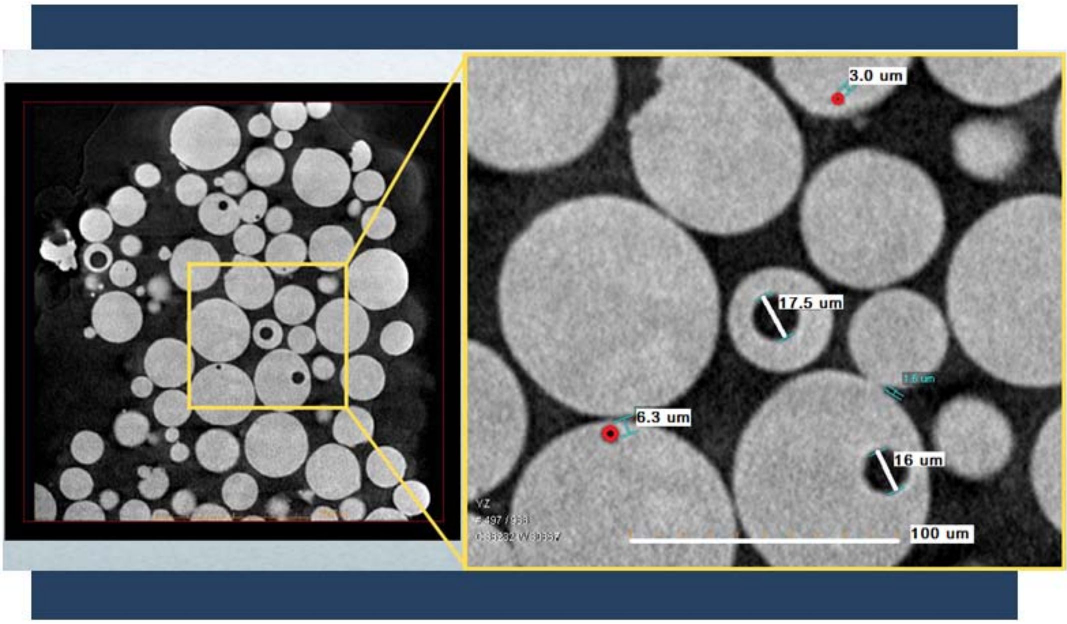

Figure 3.7. Porosity view on PREP powder material

Not until the findings from *Ashan et al.* [99] were the same defect analysis between PREP and GA Ti6Al4V powder was conducted; the presence of inner porosity on Ti6Al4V PREP powder was reported. This showed that not only the gas atomization system creates hollow cavities within the powder particles but also the PREP powder manufacturing method is susceptible to this type of material flaw.

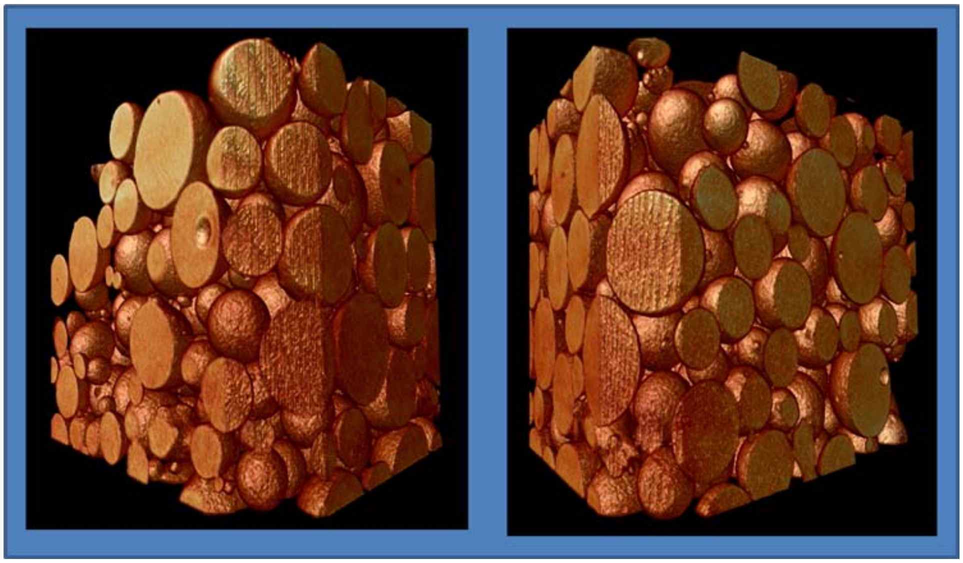

Figure 3.8. PREP powder 3D rendering

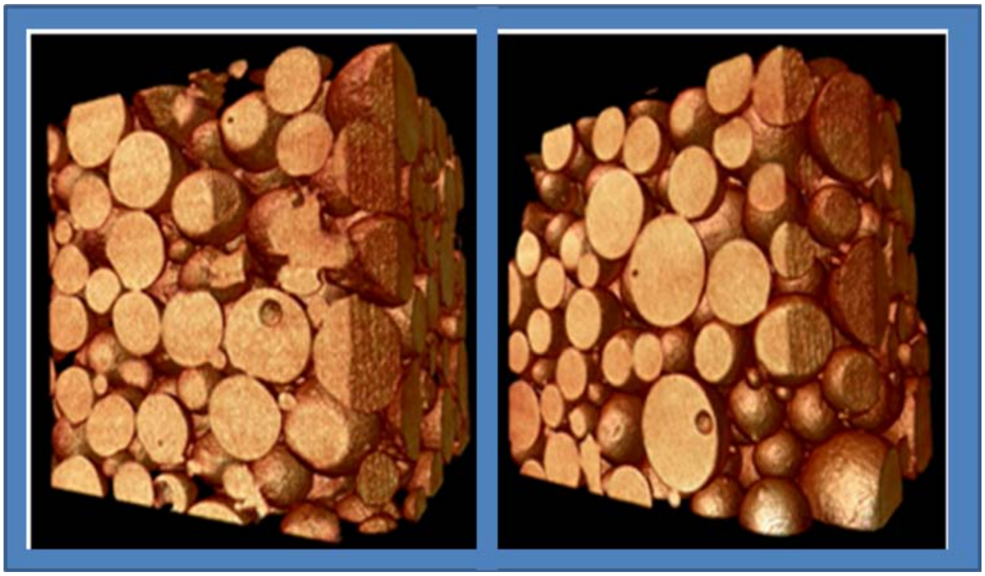

Figure 3.9. 3D Image rendering for both PREP and GA powder. PREP (left) and GA (right) sintered powder

The presence of particle porosity in the powder feedstock material represents an important factor for consideration during the (EBSM) process. Since most of the powder feedstock initial particle porosity is commonly retained in the final part, it has a deleterious effect by decreasing ductility and stress rupture properties [97]. Despite the fact porosity evolution mechanism is not fully understood, some methods to mitigate this effect are proposed such as: using a larger powder particle porosity/powder particle diameter ratio; use of an appropriate remelting strategy [100]; using only new powder, since recycled powder is commonly contaminated, and finally regulating the use of shielding gas (on selective laser based methods), an exacerbating factor for porosity formation[98]. It is of note that these findings come from laser assisted additive manufacturing technologies, where the environment is quite different from the (EBSM) process. The electron beam selective melting process includes a vacuum system, diminishing the deleterious effect of the shielding gas found in laser assisted technologies.

3.3. Bulk Density

Mercury pycnometry was used to calculate the bulk density from powder porosity volume measurements on GA and PREP powders. Liquid pycnometry, is based on the principle of volume displacement, which considers that mercury at atmospheric pressure will not enter pores smaller than 15 microns in diameter and will fill all pores larger than 15 microns. The density of the sample is calculated by the volume difference between the sample container and the intruded mercury volume; together with the mass of the sample.

Table 3.1. Mercury Pycnometry results for PREP and GA powder density

Property	**GA Powder**	**GA Sintered Powder***	**PREP Loose Powder**	**PREP Sintered Powder***
Total intruded volume (cm^3/g)	0.1509	0.1360	0.1573	0.1373
Bulk Particle Density (g/cm^3)	2.6054	2.8764	2.5998	2.6674
Total Surface Area (m^2/g)	0.0259	0.0162	0.0222	0.0173
Apparent Density (g/cm3)	4.2920	4.6556	4.2979	4.2080

**Powder material was sintered at 800°C.*

Additionally, porosity values were calculated using the ratio between bulk density and apparent density seen in equation(3.1), for a better representation of the subtle densification process occurring between the powder particles. As seen in Table 3.2 porosity values are similar in both powders, but the difference in porosity reduction is slightly larger in GA powder, mainly due to its smaller particle size.

$$Porosity(\%) = \left[1 - \frac{Bulk\,Density}{Particle\,Density}\right] * 100 \qquad (3.1)$$

Table 3.2. Porosity Calculation between PREP and GA Powder

Material	***Porosity %***	***Porosity Reduction During Sintering %***
PREP Powder	38.2	0.3
PREP Sintered	37.9	
GA Powder	39.3	1.1
GA Sintered	38.2	

A better view of the porosity dependence on powder sintering can be observed in Figure 3.10 followed by a linear fit for the total porosity, where two types of samples (3 per group) of loose powder as well as powder sintered at 800 °C were measured. Similar porosity values were initially observed on PREP Ti6Al4V powder by [101] and the small differences between PREP and GA are accounted for the dissimilar particle size fraction used in this study.

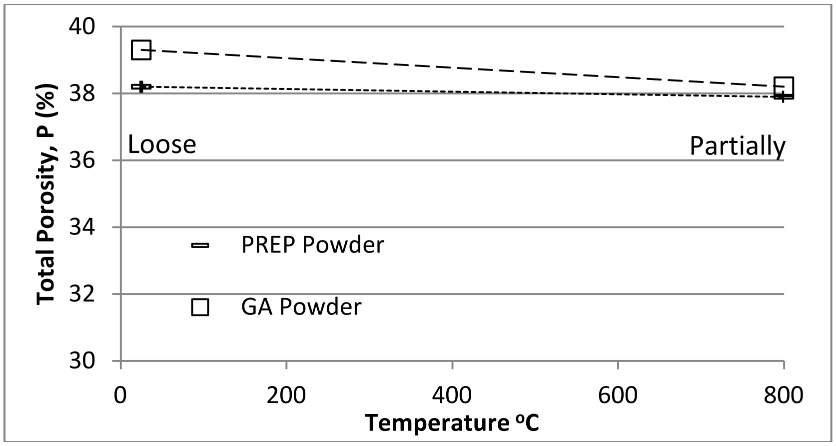

Figure 3.10. Temperature dependence of the total porosity content of sintered PREP and GA Ti6Al4V alloy powder

3.4. True Density

Data was obtained from gas pycnometry using helium at 10 psi. Average values were found for GA loose and sintered powder of 4.47 g/cm^3 and 4.39 g/cm^3 for loose and sintered PREP powder. These values can be attributed to the limited size of the sample and the occasional appearance of particle inner porosity.

3.5. Surface Area

The *specific surface area* is defined as the area of solid surface per unit mass of material. In practice, what is actually determined is the accessible (or detectable) area of solid surface per unit mass of material. This distinction is important because the value determined in a measurement is dependent on the method, the experimental conditions employed, and the size of the probe [81].

Surface area analysis was conducted on both types of Ti6Al4V powders (GA and PREP) in loose and sintered states, to later evaluate the different stages of radiation losses during the manufacturing process. As mentioned in sections 2.2.2 , geometric density measurement by mercury and surface area by the BET method were used for comparison purposes. Previous data available on surface area, found using BET surface analysis, was published by *Engel* and *Bourell* [102] to correlate this property to outgassing rates during SLS processing where GA and PREP powder were used, and values ranging from 0.04 – 0.06 m^2/g were found.

Table 3.3 Comparison between calculated surface area for Ti6Al4V powder and sintered material using BET and liquid pycnometry method

Material	Surface Area (m2 / gram) - BET	Hg Intrusion
Loose GA Powder	0.023	0.0259
Loose PREP Powder	0.016	0.0222
Sintered GA Powder	0.016	0.0162
Sintered PREP Powder	0.013	0.0173

Differences are seen between the values obtained by krypton (gas) adsorption and mercury intrusion (Table 3.3). Higher values would be expected from gas absorption than mercury intrusion. The differences are believed to be due to the pores outside the range of mercury pycnometry, which, while low in pore volume, still contribute to surface area [103]. In our case, the partially sintered material will behave differently in the BET method than in the mercury intrusion, mainly due to the nature of the measurement. In the BET method, low pressures (up to 10^{-9} Torr) and low temperatures (77 Kelvin) are used during the measurement process where an inert gas is used as an adsorbate and little damage is done to the low cohesive particles (partially sintered powder). On the other hand, the mercury intrusion make use of high positive pressures (50 psi), increasing the chance to partially damage the weakly *pressureless* sintered structure. Even though it is well known that BET and mercury intrusion possess a linear relationship only at high surface area values from 10 m^2/g to 100 m^2/g [104], mercury intrusion represents a practical alternative for porosity, surface area, bulk density, and apparent density calculations on the same tests. Surface area values were also calculated using the laser diffraction system, where values of 0.0721 and 0.0055 m^2/grams were found for GA and PREP respectively on loose powder condition. Again, higher values of surface area were found for GA powder over PREP but the effect of sample and accuracy of the method creates significant divergence from the data obtained by BET and liquid pycnometry.

3.6. Particle Size Distribution

The powder particle size distribution has been a subject of evaluation in additive manufacturing showing its effect on part density, surface finishing and mechanical properties such as tensile strength[105]. This properties are the result of process variables such as heat source energy absorption, powder bed density and spreading [106]. Concerning to Ti6Al4V powder, particle size studies have been previously conducted by *Ziya et al.* [101] in which a comparison was made between PREP processed CP-Titanium and Ti6Al4V alloys. These powder fractions showed a Gaussian like granulometry with a bi-modal distribution for the former and a mono-size distribution for the latter, with a higher average diameter size observed on Ti6Al4V powder. Subsequently, *Ahsan et al.* [99] conducted a study on Ti6Al4V powder produced by the PREP and GA method showing smaller particle diameter values for PREP material. A particle size correlation was made by this author respective to the advantages of using smaller particle sizes to improve bulk interlayer porosity, deposition rates and surface roughness, the last conclusion also supported by *Karlsson et al.* [107].

Table 3.4. Ti6Al4V powder particle size distribution comparison chart

Powder Supplier	Powder Manufacturing Method	Particle Size Range (um)	Reference
LPW Technology Ltd.	PREP	0 – 200 72 (Average)	[108] [99]
American Specialty Metals Inc. (ASM)	PREP	45-150 50-150	[109] [110]
Phelly Materials Inc.	PREP	45-250 107 (Average)	[101]
Starmet Corporation	PREP	8 – 118 67 (Average)	[111]
ARCAM-AB	GA	45-100	[112]
LPW Technology Ltd.	GA	20-150 94 (Average)	[108] [99]

Particle size distribution influence on the process conditions and final product properties is clear. However, there is controversy on the data reported by most authors using either PREP or GA Ti6Al4V powder materials as observed in Table 3.4 reported by some powder manufacturers and research literature.

Additional authors reported the use of Ti6Al4V powder particle sizes between 45-250 microns [113] and 45-150 microns [114] for PREP and GA powder respectively. As seen in Table 3.4, there is not a general consensus on the particle size distribution for powders produced by either method; therefore, making a general statement about differences between their average size distributions is not possible. Data scattering in particle size distribution resides in factors such different process conditions used by a determined powder manufacturing provider and the lack of specific values requirements on initial standards, initially created for powder material to be processed by laser based technologies (i.e. ASTM F1580-01, AMS4999A) and a lack of current standards for particle size distribution specifically designed for the EBSM process like (ASTM F2924 – 12 section 7.1.). These standards mainly state that the particle size range should be determined between the vendor and the customer, based on the application. This means the particle size distribution will be controlled through a classification method (sieving) restricting upper and lower particle size values. For this reason, a study on the powders used for our validation process was conducted and reported here, with the aim of improving the existing database on Ti6Al4V powders.

As mentioned in section 2.2, plasma rotating electrode PREP powder and gas atomized GA powder and was the subject of evaluation in this study. Based on published data from Table 3.4, it is found that neither evaluation has been done comparing powder sizes from different suppliers or the effect of the particle size characterization technique and sample quantity. Some methods used for particle size distribution consisted on the digital imaging quantification of a small fraction of powder particles [111], and some others by using a few grams of material hardly representing the powder batch used during the build.

The method used to obtain particle size distribution on PREP and GA Ti6Al4V powder material was laser diffraction. This technique is based on the spectral analysis from diffracted light coming from a dry powder flow; when the laser beam passes through this particle dispersion in air, the angle of diffraction increases as particle size decreases. Two particle dispersion methods were used in this analysis (wet and dry); the main difference between these two techniques being the amount of sample used for the analysis and the dwell time of the sample in front of the diffraction system. Better said, the amount of sample required to run a wet test is 5 grams, compared to 250 grams used for the dry test. Both GA and PREP powder were analyzed first using the wet mode (see Figure 3.11).

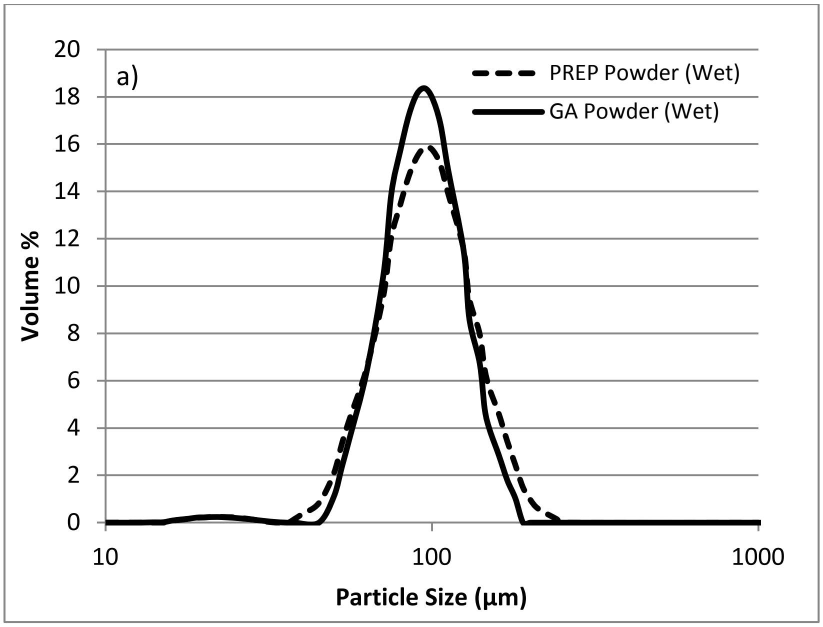

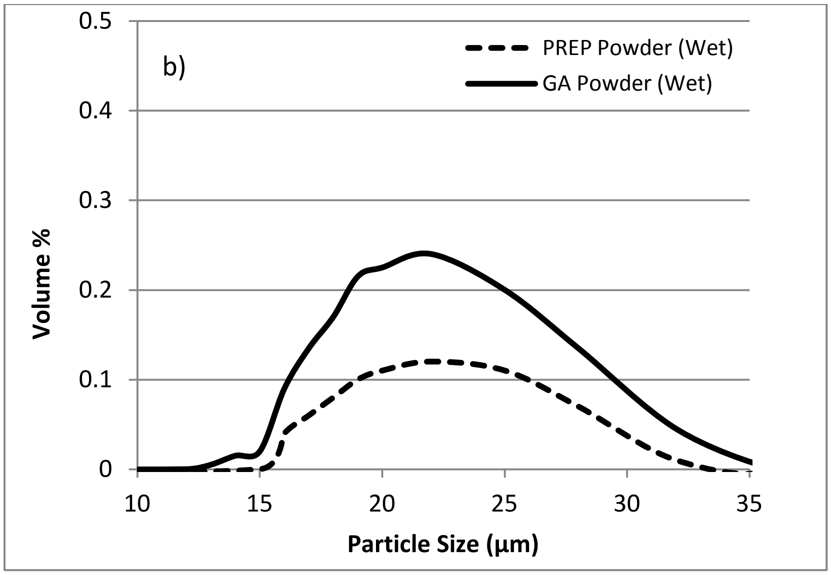

Figure 3.11. Bimodal Particle Size Distribution for PREP and GA powder using laser diffraction in wet mode. (a) Total distribution, (b) Smaller particle distribution

In the wet dispersion mode, no major difference was observed between PREP and GA powder material, save a lower volume percentage from the PREP powder at 50% of the distribution (approximately 100 microns in size). The same observation applies to the bimodal distribution of particles ranging from 15 to 35 microns in size, where the PREP powder seems to have a lower volume percentage. A second test was conducted between PREP and GA powders, this time using a dry laser diffraction mode and a larger sample (250 grams).

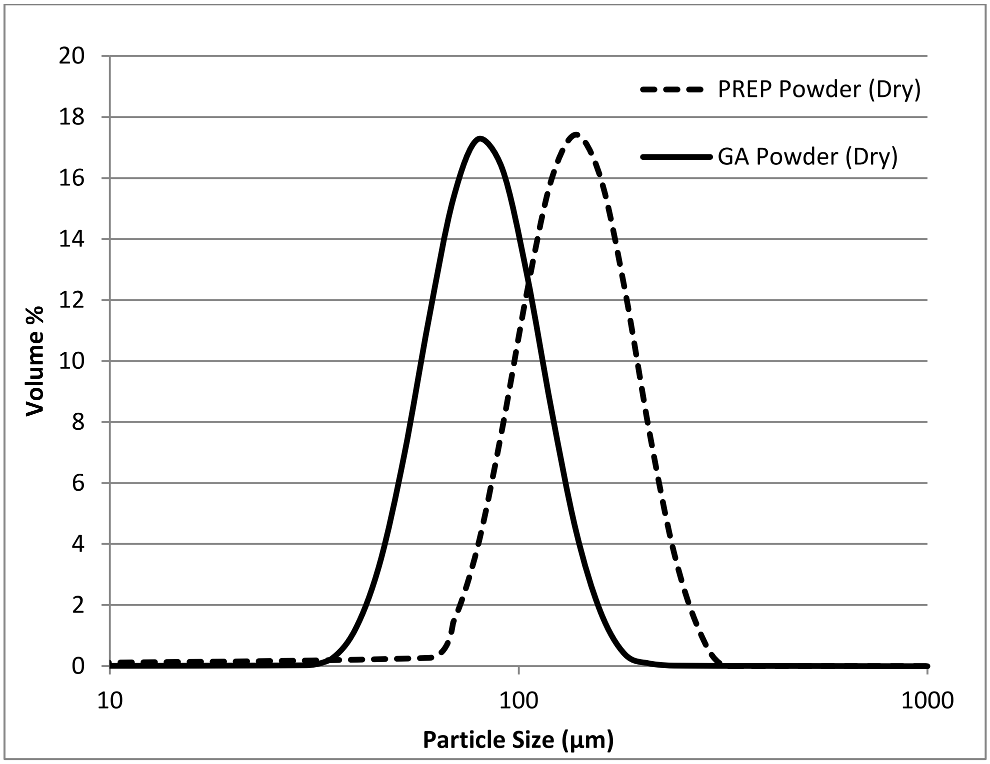

Figure 3.12. Particle size distribution comparison between PREP and GA powder material obtained by laser diffraction in dry mode

As observed in Figure 3.12, the average size of the PREP powder is greater than GA, contrary to the findings from *Ahsan et al.* [99]. A more detailed description on the differences of powder sizes based on the dispersion method is seen below (Table 3.5).

Table 3.5. Laser Diffraction Particle size distribution for PREP and GA powder based on histogram data

Powder Type	Dispersion Mode	Diameter at		
		10%	50%	90%
PREP	Wet	59.53	92.03	139.37
GA	Wet	62.59	90.13	128.31
PREP	Dry	86.58	128.49	189.24
GA	Dry	58.62	87.18	129.70

Comparison data between the same powder using wet and dry method is depicted in Figure 3.13 and Figure 3.14.

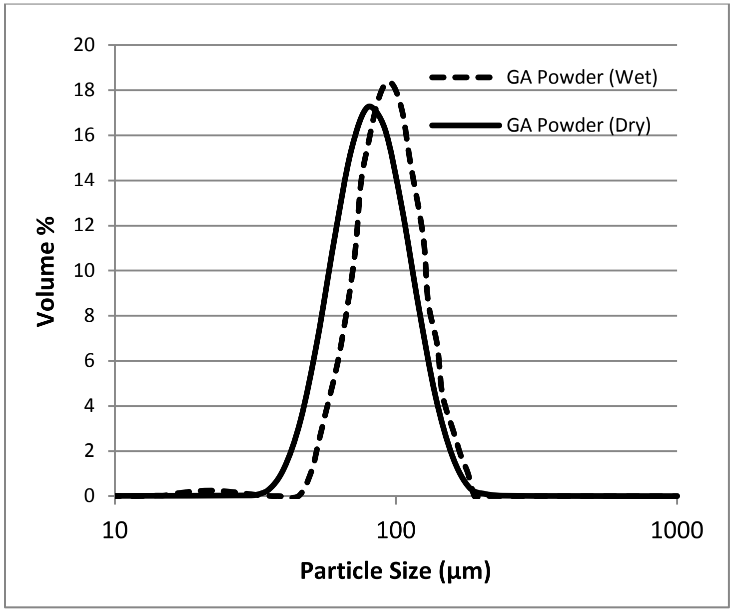

Figure 3.13. Particle size distribution by laser diffraction on GA powder using wet and dry analysis

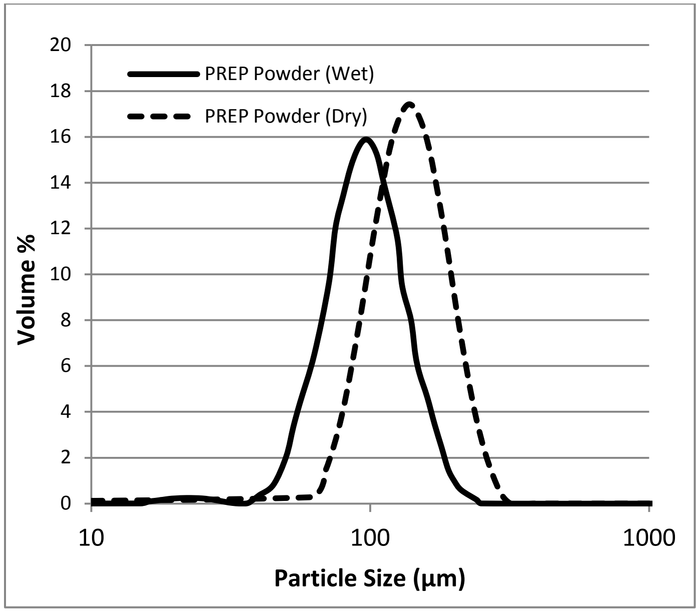

Figure 3.14. Particle size distribution by laser diffraction on PREP powder using wet and dry analysis

Differences in values obtained by wet and dry methods were previously reported by *Gackstetter* [115]; showing the main cause to be the nature of the dispersion mode and the sample dwell time facing the detector, as previously described. In a wet measurement, the same particles are being analyzed over multiple measurements, increasing the statistical probability for small particles sizes to be detected. This differs from dry measurement, in which a different set of particles is analyzed each time and final results rely more on reproducibility than sample recirculation.

3.7. Summary

Powder particle morphology and particle inner porosity manufactured by PREP and GA processes were analyzed in this chapter. Inner particle porosity was found on both processed powder particles, with a lesser size and frequency on the plasma rotating electrode (PREP) processed material. Average particle sizes for GA powder were found to be smaller than PREP and the effect of the particle dispersion mechanism and sample size on the data was obtained. Higher density values using smaller powder fractions due to more efficient particle packing was observed including its effect on surface area changes.

4. Thermal Properties Characterization of Ti6Al4V Powder Materials

During the EBSM process, material properties of the alloy in the powder, molten and solid state condition, play an important role on the additive manufacturing process. Initially, a set amount of particulate material is placed underneath the built plate and used as a support and thermal isolation during the build plate pre-heating stage. Later as the additive process continues, additional powder is placed on top of the build plate followed by an electron beam selective melting. Therefore the cooling process of the built part (factor controlling its microstructure and thus final properties) is determined by how fast the heat is removed from the solid surface of the built. This heat removal, takes place in different locations in a different way. At the top of the build part (melt front) heat is lost by direct radiation to the vacuum chamber and the radiation shield; on the orthogonal and parallel build direction heat is transferred by conduction and radiation to the powder for the former and conduction through the heat sink complex comprised between the built plate and the supporting powder located underneath it for the latter.

Thus, thermal properties data such as heat capacity, thermal conductivity and surface emissivity are crucial information required when modeling the temperature evolution during the additive process is desired.

Early results on thermal properties of Ti6Al4V alloys, dating from 1961, were obtained on heat capacity at low temperatures, close to the *apha-beta* transformation[116]. Later, considering the high reactivity for Ti6Al4V at elevated temperatures >1450^{o}K, *Cezairliyan et al.* measured the heat capacity using a transient millisecond heating technique[117]. Other authors reported heat capacity values and thermal conductivities in solid and liquid state, using DSC for low temperatures and high speed heating pulses for liquid material, interpolating the values between 1000^{o}K and 1500^{o}K, [78, 118-120].

Recently, the effect of heat treatment temperatures and cooling rates on heat capacity were also evaluated by *Homporova et al.* [121]. These studies showed higher enthalpies of formation for the *beta* phase from the alpha-beta region as the cooling rate increased, as well as the presence of a martensite exothermic decomposition at temperatures close to 750^{o}K. However, heat loss is not only caused by conduction in the EBSM manufacturing system; an important amount of heat is also lost through radiation of the powder bed and solid material during the simultaneous heating of several powder layers, which most current models and simulations do not include in their calculations. For this, initial emissivity evaluation on solid Ti6Al4V, alloy plates were tested by *Coppa* and *Consorti* [122] and later re-evaluated during laser machining process by *Yang et al.* [123].

Considering how sensitive the thermal history of a metal alloy is to material properties such as heat capacity and thermal conductivity; data commonly obtained from invested casts (or quenched and annealed) Ti6Al4V materials are not representative of the powder process conditions and resulting particle microstructure of materials used for EBSM applications; even the use of these bulk values to predict thermal properties such as thermal conductivity based on emissivity values [124], powder emissivity based on bulk material values [125], thermal conductivity based on bulk properties [71] or sintered state [64] showed not to be accurate enough, mainly by discrepancies on the radiative contribution of the heat transfer model when validated with experimental data.

Therefore, direct measurements on the thermal properties for powder feedstock (as-received) and the final solid EBSM produced part by the additive process (as-built) was required to improve previous EBSM model misrepresentations produced from assigning powder properties approximations from the material in bulk and using the same thermal properties as the solid material disregarding the effect of thermal history. As a result, heat capacity as well as thermal diffusivity, thermal conductivity and surface emissivity of Ti6Al4V powder produced by the PREP and GA process, as well as its respective solid properties of this material after been produced by EBSM, were reviewed here.

4.1. Specific Heat Capacity

Differential scanning calorimetry was performed on PREP and GA powder material in as-received (new) condition, as well as recycled (used) and solid EBSM-produced parts. The DSC specific heat capacity curve measured in argon was recorded using an oxygen trapping system (OTS). This trapping system is very efficient in removing traces of oxygen from the purge gas preventing the oxidation of the sample at high temperatures.

4.1.1. Heat Capacity on PREP and GA Powder Feedstock

The first set of samples corresponding to the as-received powder material is plotted in Figure 4.1. Heat capacity (C_p) curves showed endothermic peaks at 950°C for GA and 1000°C for PREP powder corresponding to $\alpha + \beta \rightarrow \beta$ transition (*beta transus)*. Additional endothermic peaks were found, representing the partial transformation of alpha into beta occurring at 672°C in GA powder and 735°C in PREP. Generally, changes in heat capacity values from PREP and GA powder are believed to be caused by a smaller GA particle size, increasing defect concentration due to a higher interfacial area [126].

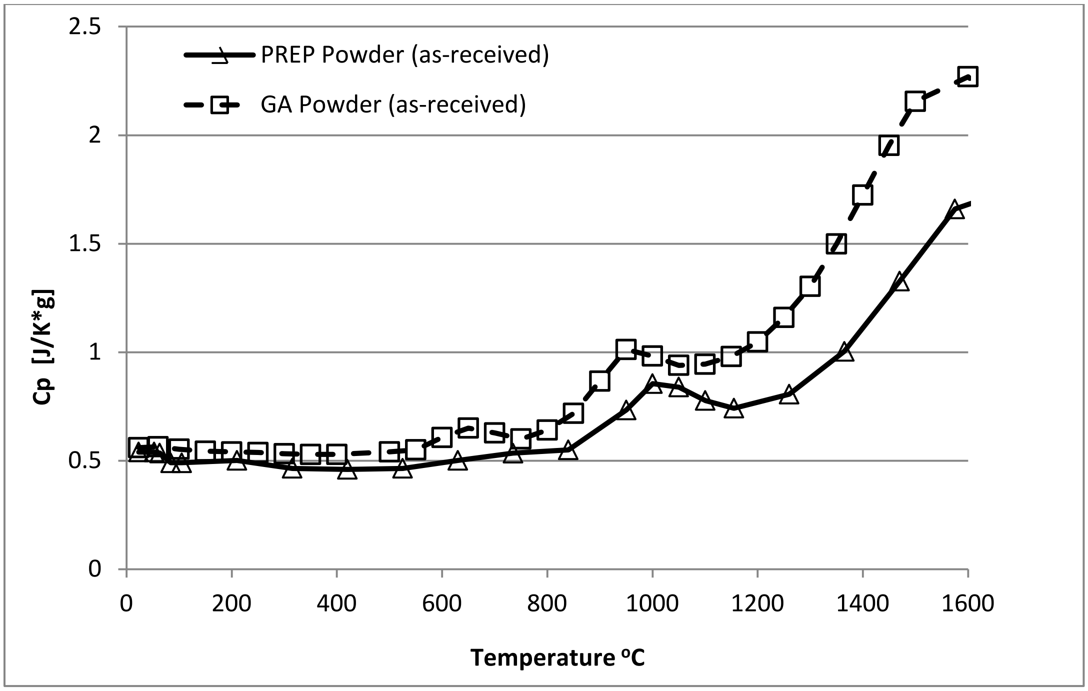

Figure 4.1. Heat capacity values on (as-received) PREP and Gas Atomized powder

The second set of samples (Figure 4.2) consisted of PREP and GA recycled powder material. The data presented the same beta *transus* temperature at 950°C. After the *beta transus* transformation took place, changes on heat capacity were not observed up to 1400°C, the temperature at which some exothermic reaction took place on the PREP powder not yet understood. Probable causes for this reaction can be attributed to surface oxide decomposition, considering previous data where a higher oxygen content was found in recycled Ti6Al4V powders [127] after the powder was processed by EBSM. Another reason is the thermal history of the powders affecting their heat capacity since its microstructure had changed from the as-received condition through an aging process coupled with a thermal cycling normal during this additive process.

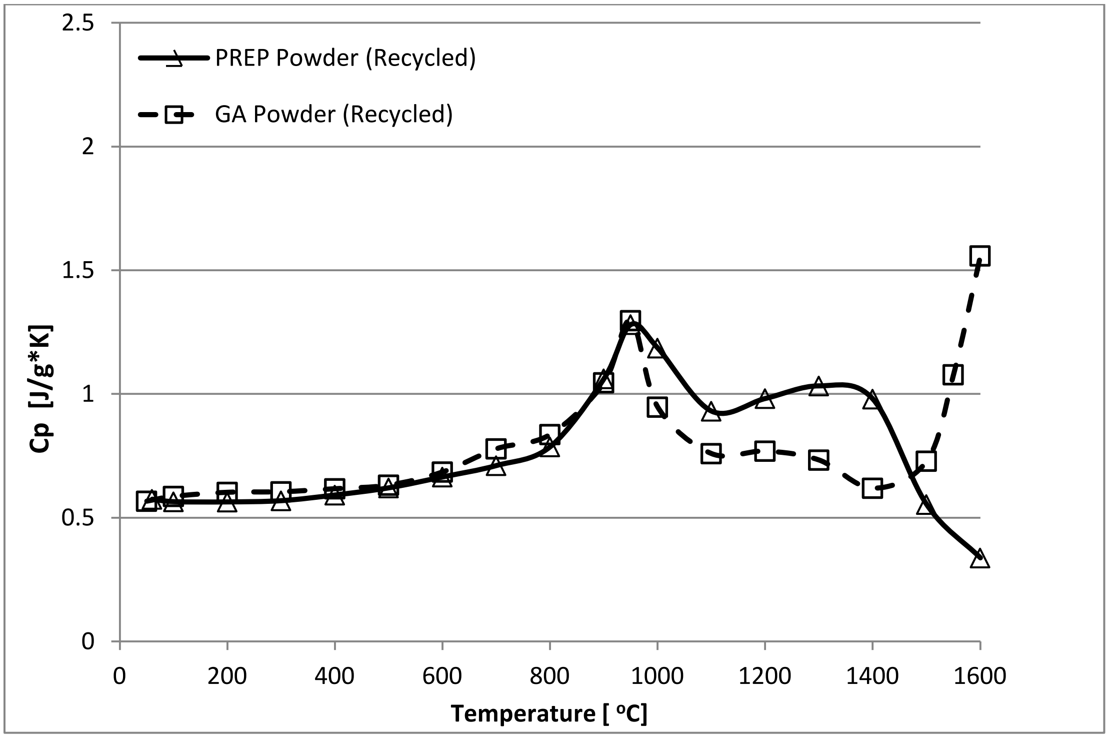

Figure 4.2. Heat capacity analysis on recycled PREP and GA powder

4.1.2. Heat Capacity on Solid EBSM parts

The third set of samples consisted of EBSM processed Ti6Al4V solid build material as seen in Figure 4.3. Samples were prepared parallel to the build direction according to Figure 2.7. The beta *transus* is represented by endothermic peaks at 980°C for PREP and 950°C for GA.

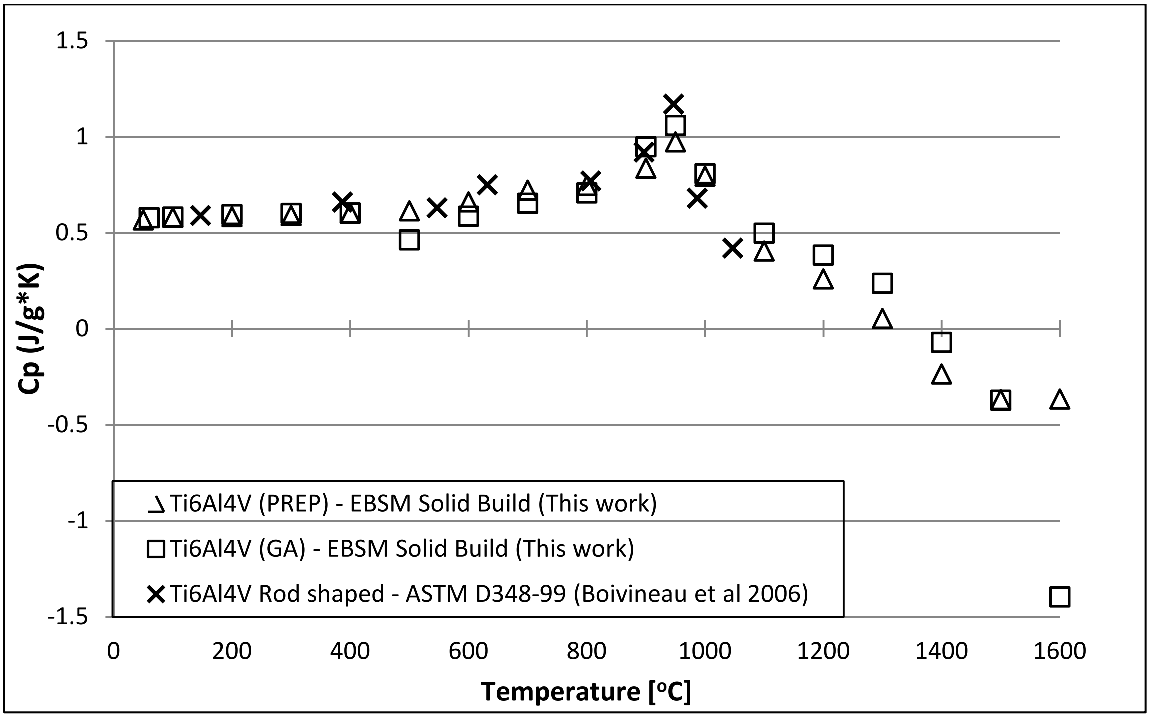

Figure 4.3. Specific heat capacity Cp comparison between solid Ti6Al4V EBSM processed (as-built) samples produced from (PREP) and (GA) powder and conventionally processed rod shaped Ti6Al4V from literature [119].

An additional exothermic peak was observed at 500°C on GA powder as a product of the transformation of martensite (α’) into α and β phase [121]. At temperatures above ~1020°C, both solid samples showed strong exothermic drift. This behavior has been shown previously only at temperatures <1200°C by *Boivineau, Cangran et al.* [119] and *Homporova et al.* [121], and appears to be related to the thermal history of the sample, normally present when heat treatment at temperatures above the β *transus* takes place coinciding with the process parameters from the EBSM system. Alpha martensite α' was present at low temperatures as a result of cooling rates from the beta region higher than 23.1°C/second [128], and retained beta was observed as a product of high cooling rates [17] later transformed into α or β. Later, during the deposition process, aging of the microstructure causes thicker alpha laths and the thermal cycling produced by the remelting process creates dislocations.

As the temperature rises, the transformation of these precipitates into beta phases creates a massive exothermic reaction where the coarsening of the beta grains takes place and re-precipitation of beta from acircular alpha phase occurs. The endothermic peak previous to the exothermic event is attributed to the formation of beta grains from primary alpha grains formerly precipitated during the aging process. Figure 4.3, also shows a comparison between the EBSM process Ti6Al4V material and conventionally processed material, showed that the additive process do not change the heat capacity of the material. Finally, it is important to consider oxygen contamination content found in EBSM parts [129, 130] and its effect on Ti6Al4V thermal properties.

4.1.3. Heat capacity measurement under vacuum

To replicate the heating process occurring during the EBSM process, an attempt to measure the C_p of the sample in vacuum was performed. Unfortunately the baseline data and sapphire runs contained a high noise to signal ratio not completely reproducible; therefore it was decided not to run the Ti6Al4V sample under these conditions, since the results would be unreliable. Among other factors, vacuum removes the gas that resides between the crucible and the sensor, which seems to disturb the DSC signal quite significantly.

It is been observed that the effect of measuring heat capacities on materials presenting strong exothermic drift probably caused by oxidation and recrystalization processes, makes it difficult to calculate values for heat capacity at temperatures above the beta *transus*. The heating rates used during the differential heat capacity measurements (20^{o}K/min) are slow enough to capture these microstructural evolution events, being required a higher heating rates to evaluate heat capacities at temperatures beyond the β *transus*, especially for used powder and EBSM as-built parts.

4.2. Laser Flash Calorimetry

Considering the data previously obtained, it is necessary to use a characterization technique for which the heating rates for the evaluation are fast enough to neglect the effect of phase transformation and grain growth evolution on the heat capacity for thermal conductivity calculations (see Figure 4.4.).

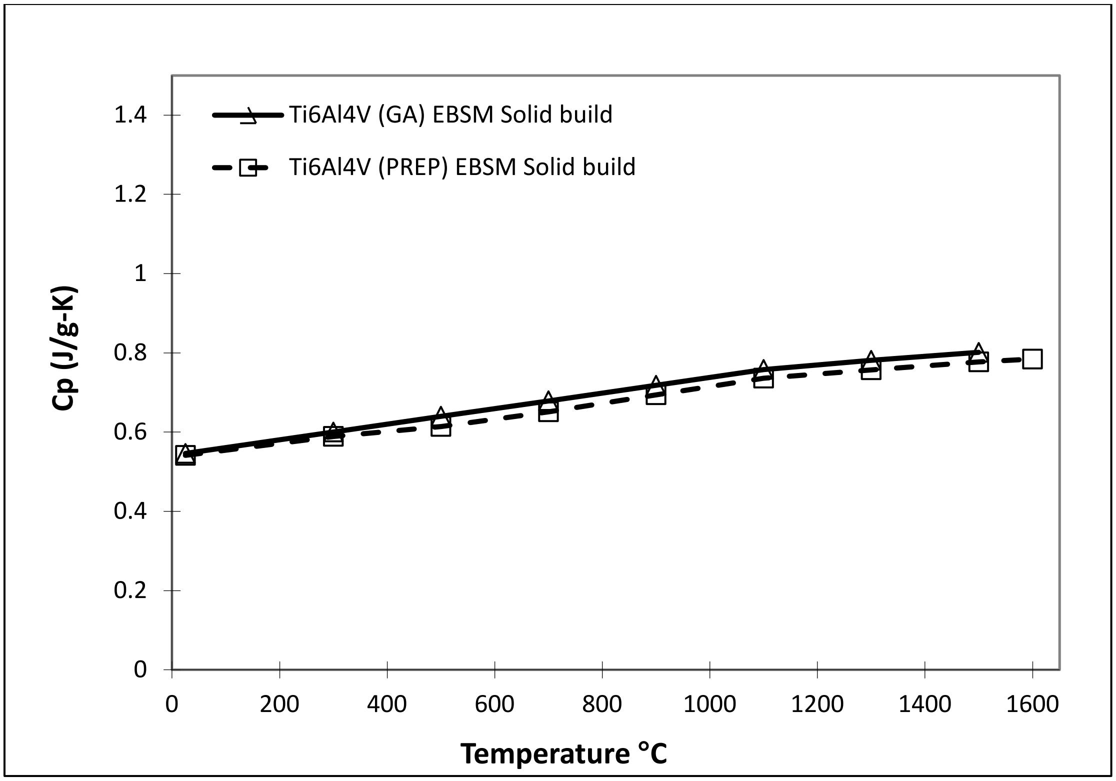

Figure 4.4. Specific heat capacity values using the laser flash method on EBSM processed Ti6Al4V using PREP and GA powder as a raw material

The heat capacity obtained by laser flash consisted of the conventional heat capacity measurement principles previously described in section 2.3.1, where a disk shaped sample is placed in the LFA, uniformly heated to the desired temperature value, and irradiated by laser pulse, increasing its temperature by a few degrees according to:

$$\boldsymbol{C_p} = \frac{\boldsymbol{Q}}{\boldsymbol{\rho}\, \boldsymbol{L}\, \Delta\boldsymbol{T}} \tag{4.1}$$

$\boldsymbol{Q}$ corresponds to the energy density; in this case the energy per unit surface area absorbed from the laser pulse. Here, $\boldsymbol{\rho}$ is the sample density, $\boldsymbol{L}$ the thickness of the sample, and $\Delta\boldsymbol{T}$ is the maximum rise of temperature after the laser pulse took place. To solve equation(4.1), adiabatic conditions must be met; requiring some improvements to the measurement technique by modifying the energy density of the sample by the total energy absorbed by the sample and $\Delta\boldsymbol{T}$ is determined after correction for heat loss from the sample. The specific heat capacity is then given by:

$$C_p = \frac{\frac{E}{\Delta T - C}}{m} \tag{4.2}$$

where $\boldsymbol{m}$ is the sample mass and $\boldsymbol{C}$ the gross heat capacity for the sample; this absorbed energy was determined by a comparison method with a known heat capacity standard sample [131].

4.3. Thermal Diffusivity and Thermal Conductivity

Thermal diffusivity, and especially thermal conductivity, in Ti6Al4V alloys is an important piece of information when an EBSM thermal modeling depiction is desired. The thermal conductivity determines factors such as cooling rates from the melting point to the built temperature on the EBSM process (625- 700°C) and the final cooling process to room temperature when the manufacturing process is complete, controlling the resulting microstructure and final built part properties.

Previous authors have documented values for thermal diffusivity and thermal conductivity only in Ti6Al4V bulk materials at low temperatures using direct and indirect methods, like longitudinal steady heat flow [132], from RT (room temperature) to 150°C [133], and high temperatures measuring electrical resistivity and total emissivity under in vacuum [117, 119, 134], and throughout the same temperature range by a data review obtained by *Mills* [78]. There is also an evident scatter in the results reported for solid materials, mainly due to thermal and mechanical history, impurity levels, and chemical composition.

In view of the differences in thermal diffusivity and thermal conductivity values in materials with dissimilar chemical composition and thermal history, it is expected to have the same trend of these values for EBSM powder feedstock produced by PREP, GA powder and the solid materials produced by the additive process which microstructures quite different from conventional alloys (while meeting the mechanical standards).

Another subject for discussion is the thermal conductivity in particulate media, for which no experimental data is available. Only numerical and analytical models exists based on bulk properties and geometrical considerations [71, 125, 135]. The thermal conductivity on a disperse medium occurs through the contact and partial sintering between the particles as a result of high temperature exposure with no applied pressure *(pressureless)*. This system can be thought as a network of contact resistances, between neighboring particles including the contribution from surface radiation. This powder *pressureless* consolidation surrounding the built act as a thermal isolation system determining the heat transfer in a perpendicular orientation to the build direction assuring a constant built temperature that, if changed, it will affect the final mechanical properties of the built part [17].

4.3.1. Thermal Diffusivity

Thermal diffusivity data was obtained using the laser flash technique (LFA) according to section 2.3.3. Tests were conducted on Ti6Al4V powder produced by PREP and GA process as well as EBSM solid built samples (as-built) manufactured using both powder types as seen in Figure 4.5.. Powder and solid samples were held in a sapphire container during the measurement; independently measured in argon atmosphere at normal pressure (760 Torr). PREP and GA powder samples materials were partially sintered during heating up to 1600°C in a high temperature furnace. The change in bulk density was reflected in a change in slope of the thermal diffusivity versus temperature curve. No correction for the thermal expansion was made. Total relative expanded uncertainty (k = 2) of the thermal diffusivity determination is ± 5%.

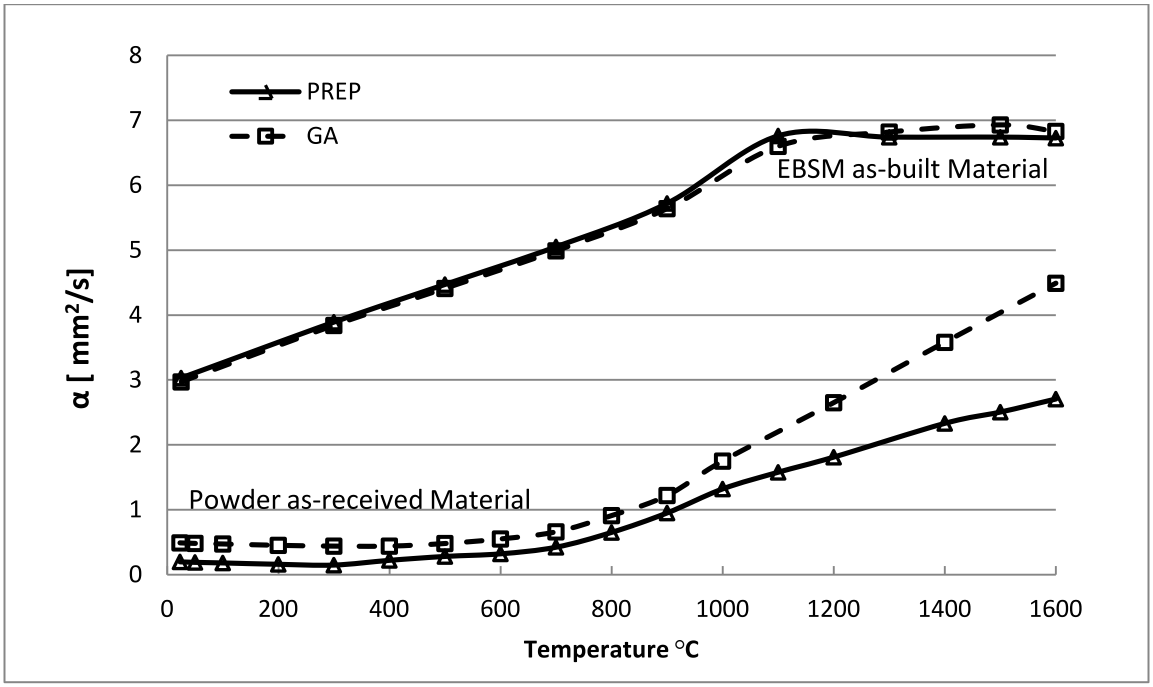

Figure 4.5. Thermal diffusivity PREP and GA Ti6Al4V material in powder (as-received) and EBSM processed (as-built) solid condition.

The lower thermal conductivity of the Ti6Al4V in powder condition can be observed. These values support the process design for low heat losses orthogonal to the built direction, which aids in maintaining a uniform built temperature. Major differences are also observed between the PREP and GA powder material, where factors such as particle size distribution within the sample plays an important role, especially during the sintering process dynamics where the PREP powder's thermal resistance due to particle contact clearly deviates from that of the GA powder.

4.3.2. Thermal Conductivity

The heat conductivity corresponds to the heat transport using as a transference media, crystalline lattice vibrations (phonons) and charge carriers (electrons), when a thermal gradient is present on a metal. Thus, the overall thermal conductivity of a metallic material is governed by the partial contribution of phonons and the electronic component of the conductivity [136]. Although, the thermal conduction of phonons and electrons particles are influenced by scattering processes caused by electron-electron, electron-phonon, and electron/phonon interaction with lattice waves, conduction electrons and with crystal imperfections and solute atoms (in the case of alloyed materials) [137]. As the temperature increases the average particle velocity increases as well as its scattering for what it is expected to obtain a decrease in thermal conductivity as the temperature increases.

On the contrary an increase in the thermal conductivity in transition metals such as titanium alloys is thought to be partially the result of a combined effect between electronic heat carriers and lattice vibrations. The electronic heat contribution is affected by the defect structure of the material but mainly by a temperature dependent carrier concentration determined by the *d*-electron level configuration [138] causing smearing and broaden of the density of states near the Fermi energy level [139]; a second factor affecting this phenomena will correspond to the lattice vibration contribution which increases as the temperature rises.

Thermal conductivity values were obtained indirectly by heat capacity and thermal diffusivity measurements on non-recycled powder (as-received) and EBSM processed solid material (as-built) through the setup described in section 2.3.1. Figure 4.6, depicts a thermal conductivity comparison between Ti6Al4V solid samples produced by EBSM and conventional cast and wrought process. As seen in the diagram, no substantial thermal conductivity differences are present when the EBSM process is used as a manufacturing method; increasing the reliability of the parts manufactured with this technique.

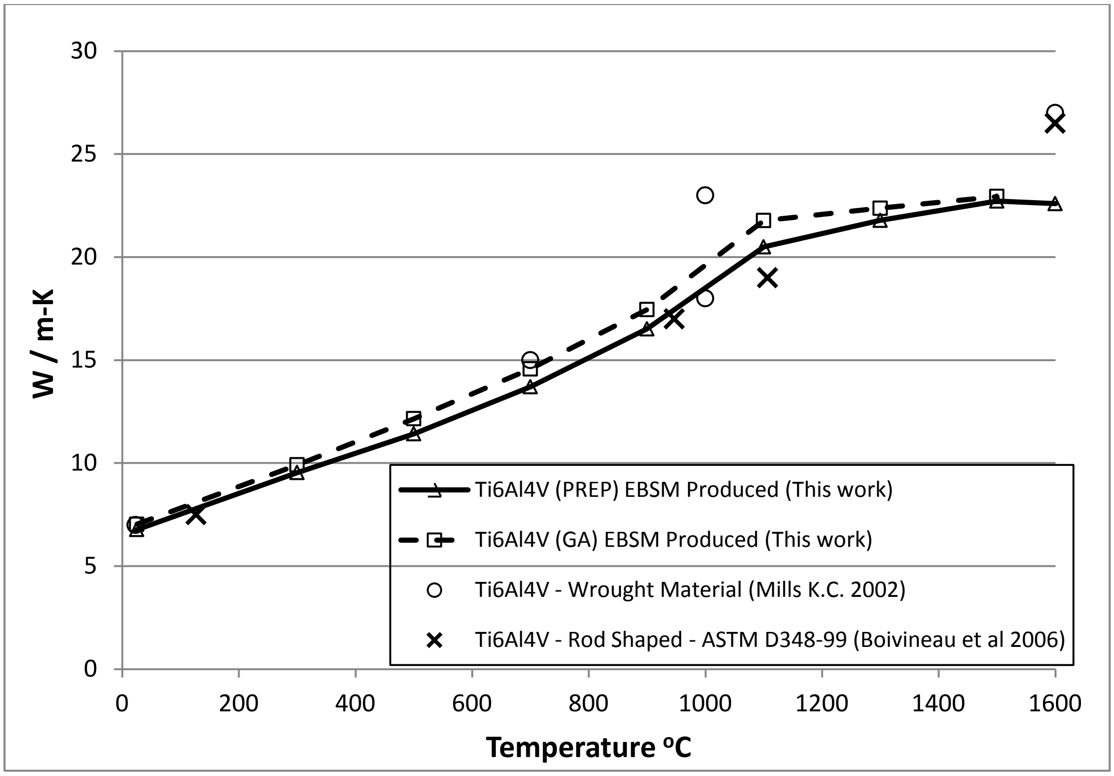

Figure 4.6. Thermal conductivity values on solid Ti6Al4V processed by EBSM from powder using a laser flash system and compared with published data on wrought Ti6Al4V [78, 119].

Another comparison was performed between EBSM processed parts and powder material as seen Figure 4.7. No major differences were observed within the powder values at temperatures lower than ~700°C; this temperature is believed to be the start of the sintering process through the titanium self-diffusion on the particles' surface, increasing the contact area and thus raising the thermal conductivity. Solid sample data showed changes in slope at temperatures close to ~900°C followed by another change at ~1100°C, representing the beta *transus* transformation. Data on solid samples showed no substantial differences between EBSM samples produced by different powder processing (PREP and GA) indicating that differences on thermal conductivity at high temperatures observed on the powder samples is a direct effect of the particle size distribution.

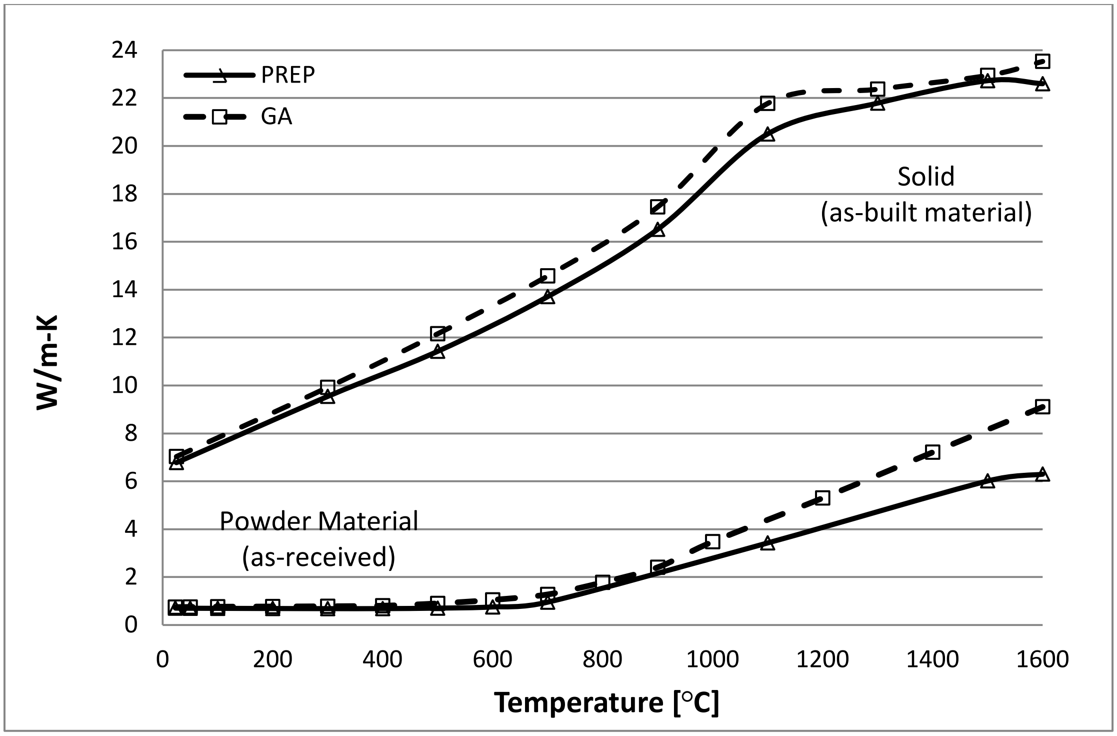

Figure 4.7. Thermal Conductivity comparison of (PREP) and (GA) Ti6Al4V powder and solid (as-built) EBSM produced samples using (PREP) and (GA) powder as a raw material using laser flash technique.

4.3.3. Effect of sample orientation on thermal conductivity on solid Ti6Al4V PREP material

So far, EBSM processed Ti6Al4V solid samples had been prepared and analyzed parallel to the build direction for comparison purposes between PREP and GA powders. Since the model and simulation will be only performed on PREP material, an extra set of EBSM produced solid samples were prepared to compare the effect on thermal conductivity due to grain growth orientation parallel and orthogonal to the built direction.

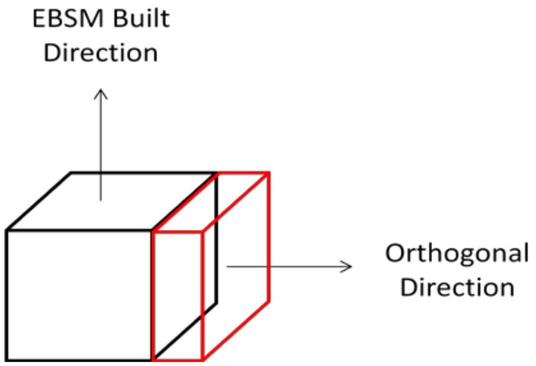

Figure 4.8. Sample orientation representation orthogonal to the EBSM built direction

Mono-oriented heat fluxes produced as a result of thermal conductivity differences between the surrounding powder and the build plate are responsible for a columnar orientation of grains produced during powder bed rapid prototyping and manufacturing. This columnar grain growth was reported early on in direct laser fabrication by *Kobryn* and *Semiatin* [140], and later in electron beam melting [13, 141, 142].

Solid samples prepared by the EBSM process using PREP powder were evaluated at temperatures in the range between 25 - 900°C, using a laser flash analysis system (LFA 457) from Netzsch Instruments Inc. as previously described in section 2.3.3. Three measurements were taken at each temperature point (n=3) with a standard deviation of 0.5 on the obtained values. The analysis temperature range was chosen considering the built temperature values, from where the main cooling of the part takes place (up to 750°C). Values from 900°C to the melting point at 1650°C were extrapolated during the modeling and simulation stage according to Table 5.2 and Table 5.3. These results were later used to create an anisotropic matrix for thermal conductivity while modeling the EBSM process, using only the data obtained from Ti6Al4V PREP solid EBSM produced (as-built) material.

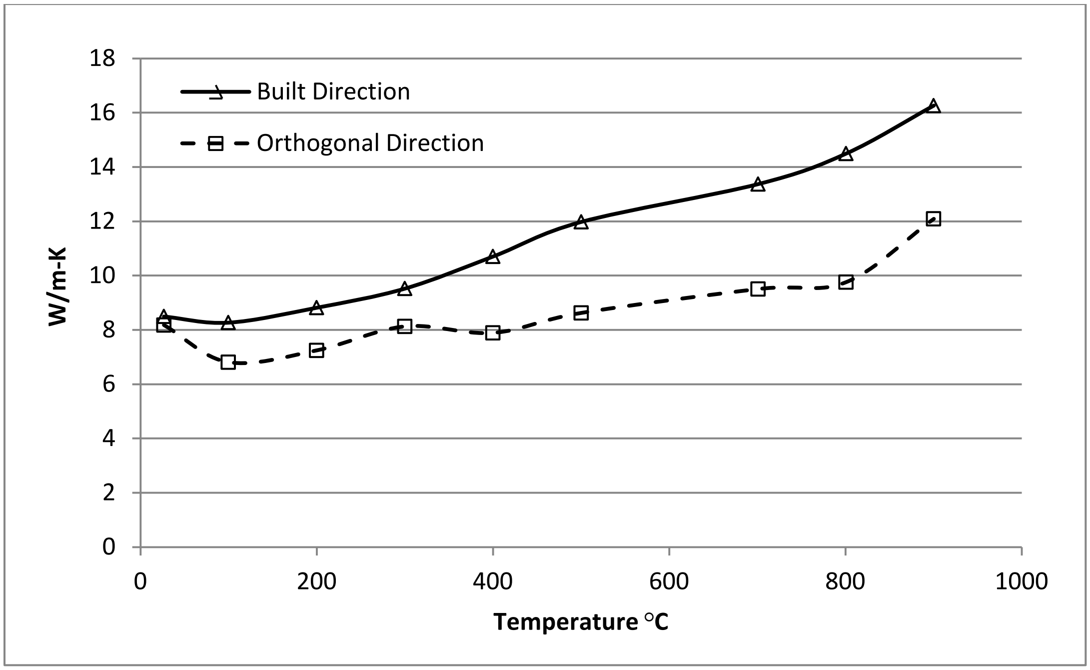

Figure 4.9. Laser flash data for thermal conductivity of Ti6Al4V EBSM processed solid samples parallel (z-axis) and perpendicular (x) to the build direction.

Differences in thermal conductivity as observed in Figure 4.9., are attributed to the presence of columnar grains parallel to the build direction as previously shown by *Al-Bermani et al.* [17]. Columnar growth is shown in this process as a product of remelting cycles of several layers at a time, creating the proper conditions and temperature gradients required for a quasi-unidirectional heat flux. This preferential heat flux on the EBSM process is additionally aided by the efficiency of heat conduction on the *z* axis compared with the *x-y* direction. The heat loss on the orthogonal build direction *(x-y)* occurs from the recently solid build part through the lightly sintered and low conductive powder material. On the contrary, the heat losses on the *z* axis are led between the solid material previously sintered and the build plate, both acting as the main heat sink of the energy applied by the electron beam creating a longitudinal cooling process thus a preferential grain growth process.

Higher thermal conductivity values along columnar grains *(z axis)* are expected due to lower crystal defects and grain boundaries interfering with the electron and lattice vibrations compared to the orthogonal orientation[136] where grain boundaries creates a lack of crystal symmetry contributing in a higher degree to the electron and phonon scattering.

4.4. Radiation in solid and particle media

The microstructure resulting from the EBSM process relies on thermal dynamics from the heat input obtained by the electron beam heat source and its interaction with the particulate media; but mostly on heat losses occurring during the build. These heat losses are caused by thermal conduction and surface radiation both being material and temperature-dependant. Manufacturing process involving the *pressureless* sintering of powder particles followed by melting and rapid cooling to a solid state was subject of study here.

To model and simulate the thermal evolution during the EBSM process, not only the heat losses by conduction (as seen in section 4.3), but also by radiation, were considered.

The radiation heat loss rate can be expressed as:

$$Q_{Radiation} = \varepsilon_{(T)}\sigma \left(T_{(Ti6Al4V)}{}^{4} - T_{(vacuum\ system)}{}^{4}\right) A_{(Ti6Al4V)} \tag{4.3}$$

where;

$\varepsilon_{(T)}$ = *temperature dependant total surface emissivity*

σ = *stefan-boltzmann constant 5.6703 10^{-8} (W/m^2K^4)*

$T_{(Ti6Al4V)}$ = *powder or solid material temperature (K)*

$T_{(vacuum\ system)}$ = *cold surroundings absolute temperature (K)*

$A_{(Ti6Al4V)}$ = *surface area of the radiating object (m^2)*

4.4.1. Radiative Losses in Particulate Media

If the particulate medium is actively participating in a heat transfer process during heating and cooling of an EBSM build part, determination of irradiative exchange between surfaces becomes quite complicated. This evaluation will require a solution of the heat radiation transfer equation (4.3) for the corresponding geometry with proper boundary conditions. In addition, the emissivity values at the process working temperatures for the particulate media (PREP and GA powder) constituting the heat transfer medium must be evaluated, including the effect of particle size distribution as a strong function of temperature [143].

4.4.2. Factors Affecting Emissivity

Emissivity is the efficiency to emit energy by radiation and its value depend on factors such as angle, wavelength and temperature. The angle from which the temperature is being measured from an angle perpendicular to the surface, known as the Lambert's Emission Law[144] considerably affects the measured emissivity. Despite no angular correlation was performed during this study, temperature measurements were conducted at an angle of 12° (see measurement setup in Figure 2.11), and the calculated emissivity is shown below.

The overall contribution to heat transport by emissivity increases with temperature and it can be observed by a shift on the wavelength from large values (infrared) towards shorter wavelengths (visible light). In contrast, factors such as surface finish and contamination adversely affects emissivity; as the surface roughness increases multiple radiation reflections takes place, increasing the measured emissivity. Additionally, surface contamination produced as a result of water vapor absorption [102] and chemical reactions with the environment, produces a thin oxide layer also resulting in high emissivity values [143].

4.4.3. Ti6Al4V Emissivity Values

Directional emissivity values were evaluated by remote temperature measurements in the infrared range between 2.5 to 5.1 microns, and later corrected as previously explained in section 2.3.6. Ti6Al4V alloy powder prepared by PREP and GA process and solid samples using the same feedstock material were used in this analysis. Sample in solid state were inspected in tow different surfaces; the rough surface area in contact with the surrounding powder and the smooth surfaces produced by the melting front. Non-contact profilometry was performed on these surfaces with root mean square – RMS values of 54 and 12 microns respectively as seen in Figure 4.10.

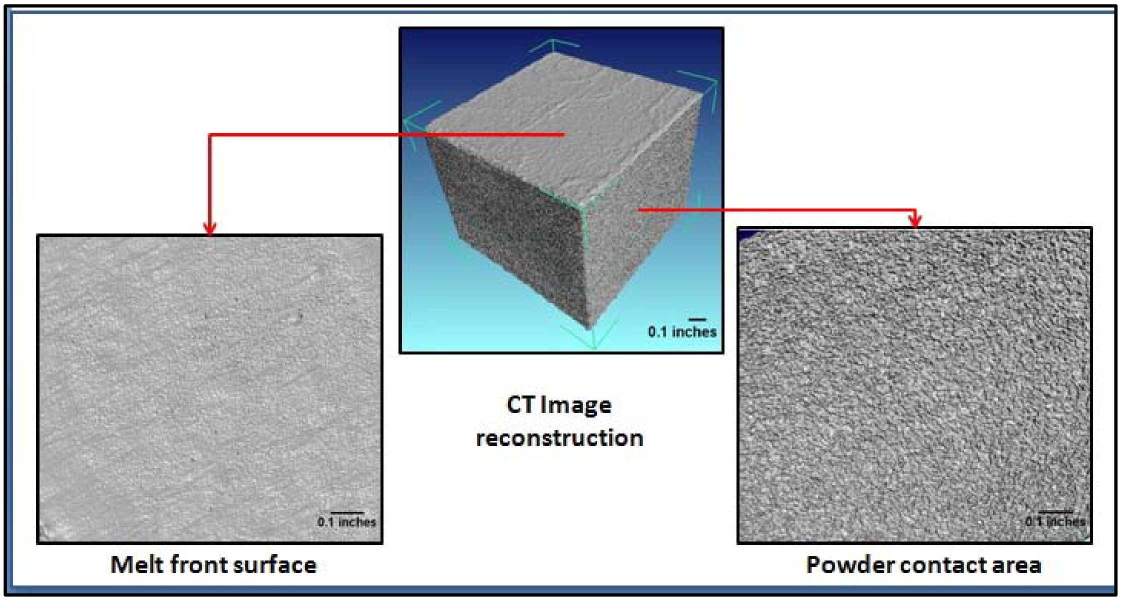

Figure 4.10. Surface imaging on EBSM sample using computed tomography (as described in section 2.2.5)

Calculated emissivity measurements on PREP and GA powder fractions are shown in Figure 4.11. The initial decrease observed in emissivity is thought to be a combined effect of the exitance angle (12 degrees), particle packing (as a result of particle size distribution) and spectral temperature measurement range (2 – 5 μms); where multiple light scattering occurring on a rough powder surface is very sensitive to its measurement angle. A sudden increase in emissivity is observed in both powders at temperatures close to ~750°C, as a result of a particle sintering process [101] decreasing the porosity, thus the total radiative surface[125].

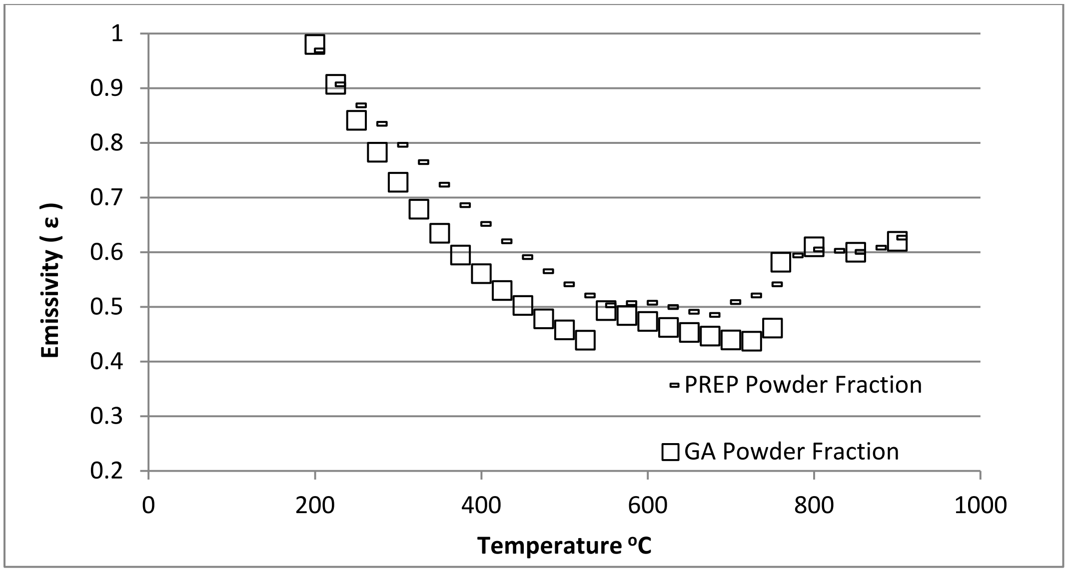

Figure 4.11. Calculated emissivity on Ti6Al4V PREP and GA powder material

Emissivity value differences between the two powders is attributed to higher surface area values observed on GA powder (see section 3.5) together with a smaller particle size distribution (as seen in section 3.6) compared to the PREP powder. For modeling purposes, the emissivity value measured at 900°C from partial sintered powder material of **ε=**0.6 was held constant, for heat loss calculation.

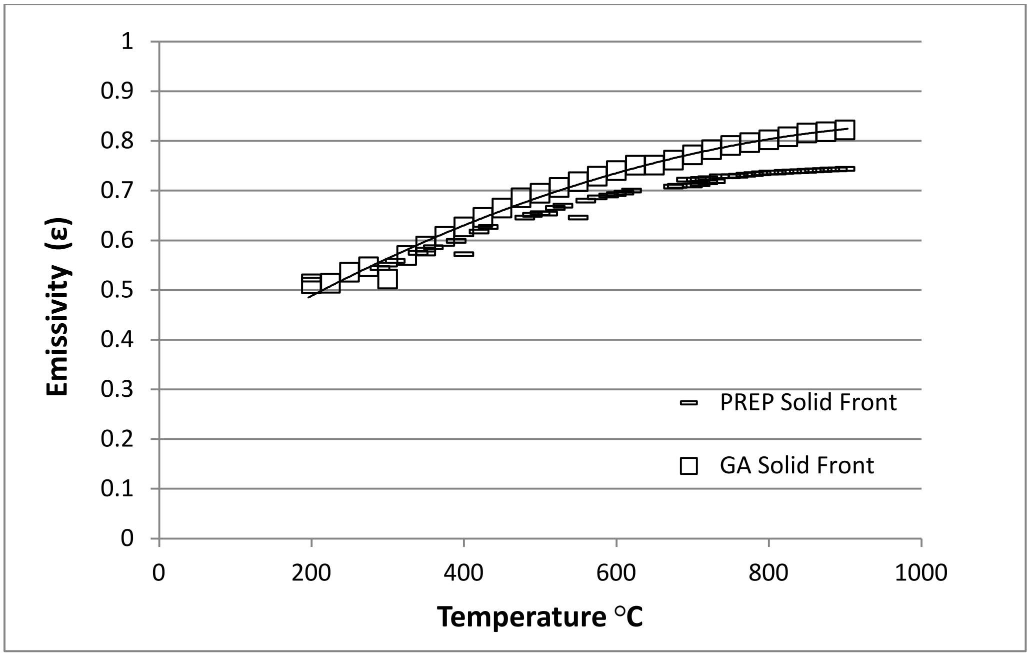

Figure 4.12. Calculated emissivity values for molten front surface in Ti6Al4V material

Figure 4.12, shows the calculated emissivity values for solid samples made from PREP and GA powder. The increase on emissivity on the molten front surface as the temperature progresses is common for metal conductor materials, with no major differences between GA and PREP. The data presented here show a qualitative agreement with previous data on Ti6Al4V alloys as evaluated by *Coppa* and *Consorti* [122] and to some extent at high temperatures by *Yang et al.* [123].

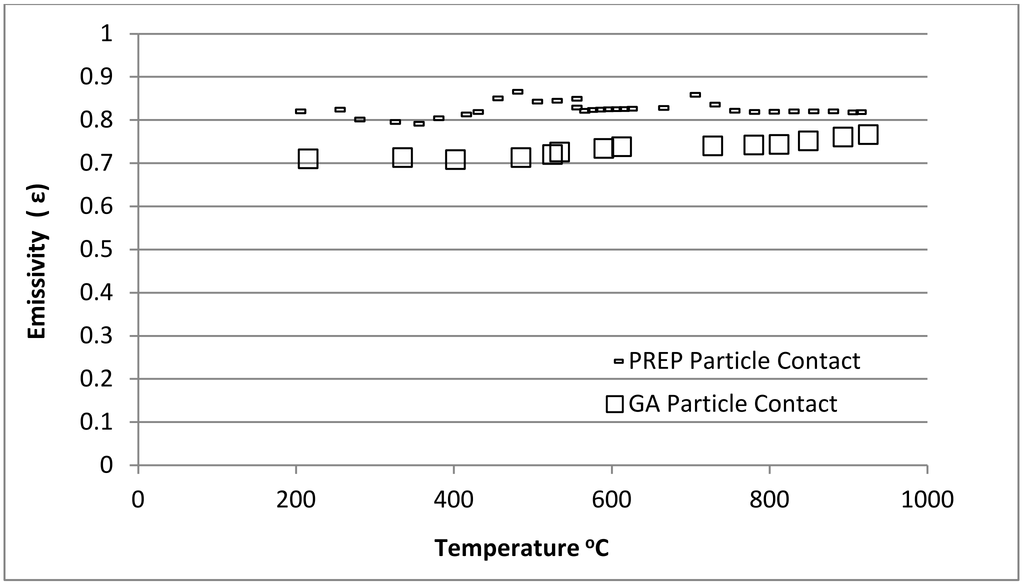

Figure 4.13. Calculated emissivity on particle contact surfaces for PREP and GA material

Figure 4.13 also shows the effect on surface roughness produced by the increased contact between molten metal and powder material, where the resulting surface roughness is directly proportional to the powder particle fractions size [107]. In this case PREP powder showed a higher particle size (with cumulative values at 50%) of 128.49, versus 87.18 microns for GA (see Table 3.5). Even though higher surface roughness is expected from the PREP surface compared to that of the GA, no major differences in emissivity were found on both surfaces.

4.5. Summary

The temperature dependant properties reviewed in this section, consider the different Ti6Al4V material conditions encountered during the EBSM process. PREP and GA powder feedstock was evaluated for heat capacity, thermal diffusivity and thermal conductivity, using differential scanning calorimetry and laser flash techniques. Beta *transus* temperatures were observed for both powder materials, as well as partial transformation from the alpha to the beta phase at temperatures lower than the beta *transus*. Recycled powder was also studied, where the effect of thermal history and surface contamination was observed. Strong exothermic peaks were found in (as-built) EBSM produced solid samples, possibly as a product of columnar grain re-crystallization as evidenced in the effect of process thermal history on heat capacity values. Furthermore, thermal diffusivity and thermal conductivity measurements by laser flash analysis were performed; showing differences in thermal conductivities between EBSM processed Ti6Al4V solid samples and loose PREP and GA powder. Even though PREP and GA processed powders previously showed differences in particle size distribution, no remarkable differences were found in thermal properties values including after being processed by EBSM.

The effect of sample orientation parallel and orthogonal to the build direction was also observed, and laser calorimetry was used to calculate heat capacity values at temperatures above the beta *transus*. Finally, directional emissivity measurements were obtained from PREP and GA powder and solid samples, where the effect of factors such as exitance angle, spectral range, powder particle size, porosity and surface roughness could be observed.

5. Modeling and Simulation of Electron Beam Selective Deposition of a Ti6Al4V Alloy

The use of titanium alloys for high performance applications such as aerospace and biomedical products have shown the advantages this material offers in terms of material properties, durability and reliability. As a result, new market trends demands this high performance alloy to be used in a wider range of products such as automotive, power generation and chemical processing among others[145]. Despite the excellent results initially obtained during the evaluation of this material, its cost remains to be a challenge to be overcome enabling the use of this metal in large scale applications. Therefore, the main strategy developed to make the use of titanium alloys possible, is mainly focused on the development of low cost manufacturing methods like additive processes assisted by electron beam (EBSM).

This process is attractive for development, testing and implementation of new materials, on account of its low material consumption and low waste. However, as with any other novel process, the level of reproducibility and control over the final material properties is still a matter of research, for what the use of tools such as thermal modeling and simulation by the finite element method (FEM) to design and improve the final product characteristics has proven to be the fastest and most cost-effective approach to make of EBSM an industrial production technology.

As previously discussed in *chapter 1*, the use of numerical methods by finite element analysis allowed to obtain approximate numerical solutions for additive manufacturing processes; using three dimensional differential equations with minor losses of accuracy. Although, current models depicting laser and electron beam based additive processes are limited by:

a. *Material properties:* Model input data regarding temperature dependant characteristics on Ti6Al4V in powder and EBSM processed solid condition required to solve the heat transfer equation such as heat capacity, thermal conductivity and surface emissivity.

b. *Model Idealization:* Only the powder to be melted is considered disregarding the thermal process control effect played by the partially sintered powder surrounding the build as well as the coupled interaction of the build supporting plate and the powder contained underneath both acting as a heat sink.

c. Model size: Comprising the manufacturing of a couple of metal layers or a small vertical wall, limiting its use for industrial applications where the amount of required layers for the build material is extremely high (i.e. 254 layers per inch built).

Consequently, a physical and thermal evaluation was performed in chapters 3 and 4 on two Ti6Al4V powders manufactured by the PREP and GA process. Despite differences found on particle size distribution between the powders, no substantial changes were found on the thermal properties, hence PREP powder and solid values were use for this model and simulation analysis.

Regarding the model idealization, this model includes the effect of the base powder supporting the build plate, the temperature dependence thermal properties for the stainless steel (SS-316) build plate and two additional domain types representing each additive layer. One domain comprises the powder layer and within the area to be contoured and completely melted by the electron beam.

Lastly, the model size representation of the layer-by-layer process included the numerical solution during the built of a 1x1x1 inch Ti6Al4V part composed by a layer thickness of 100 microns for a total of 254 layers of build material previously depicted in section 2.4.

5.1. The EBSM Process

Before discussing the strategies used to model the (EBSM) system, a brief description of the process is outlined in this section. A cubic sample (1”x1”x1”) was manufactured using an Arcam A2 system (see Figure 5.1) using Ti6Al4V powder produced by plasma rotating electrode process (PREP). The cubic shape was chosen to facilitate uniform heat distribution throughout the part, ruling out thermal gradients as a determining factor.

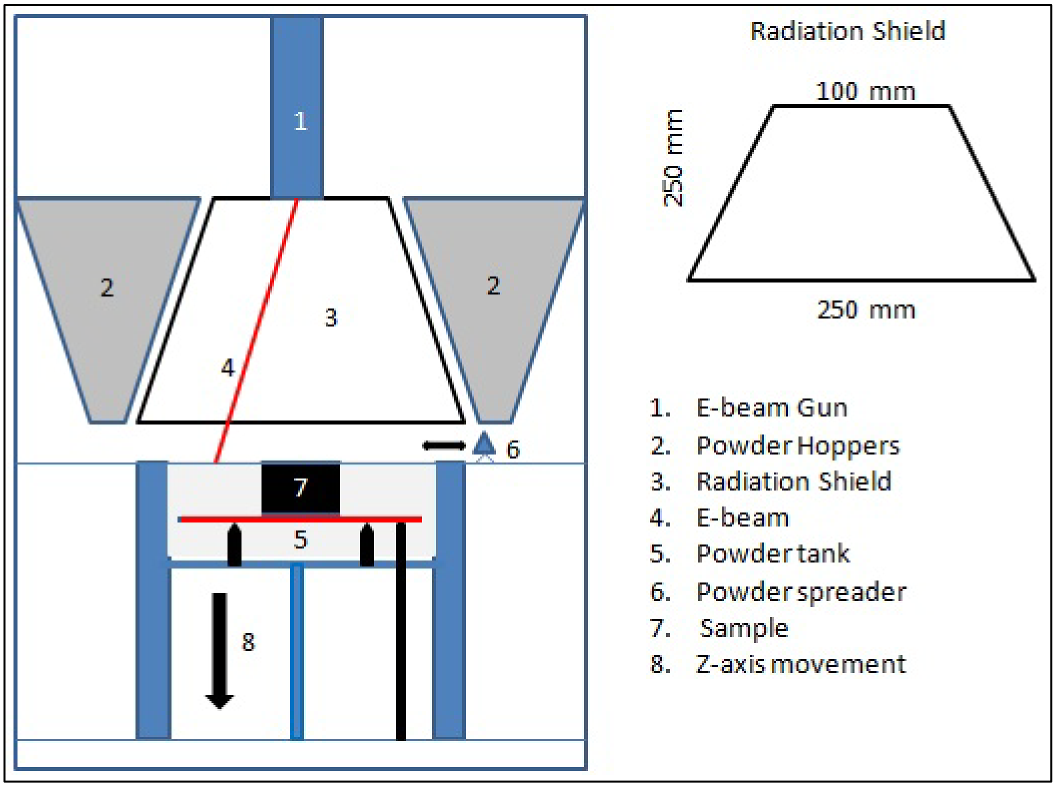

Figure 5.1. Arcam A2 EBSM System Layout

This build system is composed by a powder tank 250mm long by 250mm width and 350 mm in height. Initially the *z-axis* movement base (marked in green) was lowered 50mm comprised by the 40mm of supporting powder and 10mm of the build plate. Subsequently Ti6Al4V powder material (marked in grey) was filled inside the cavity followed by the placement of a stainless steel build plate (marked in black) with dimensions, 210mm long by 210mm width and 10mm thickness, procuring that the only area exposed from the plate is the top surface and the bottom of it is in contact with the thermocouple (marked in red) as depicted in Figure 5.2. This setup limits the total manufacturing height to only 300mm.

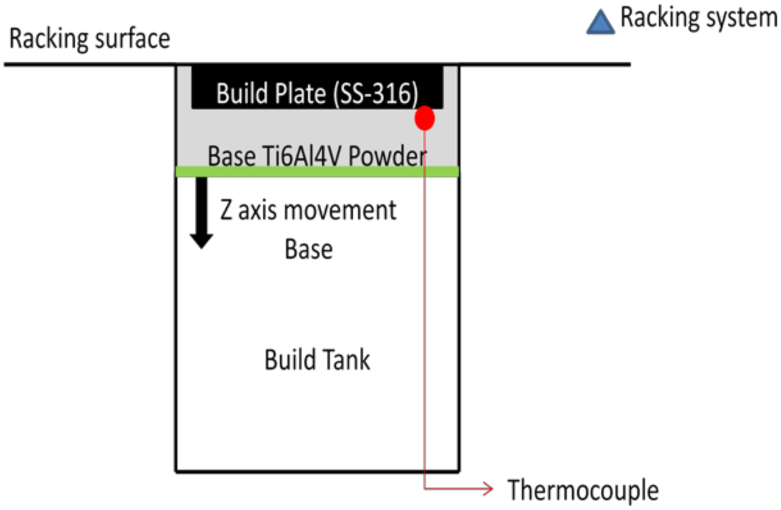

Figure 5.2. Cross sectional view representing the base powder material (in grey) supporting the built plate (in black) and the z-axis movement plate (in green) including the thermocouple location (marked in red).

Once the build plate has been properly aligned within the metal powder, the EBSM process is initiated by closing the system and pumping down the process camera to ~ 1x10^{-3} mBar. When this base pressure is attained, the build plate is heated by the electron beam from room temperature to ~475°C using a defocused electron beam (see Figure 5.3). Afterwards, a degassing process takes place for 10 minutes, so species like water vapor can be desorbed from the surface of the plate. Once degassing is concluded, the temperature of the build plate is increased by the electron beam until it reaches 734°C, corresponding to the initial build temperature.

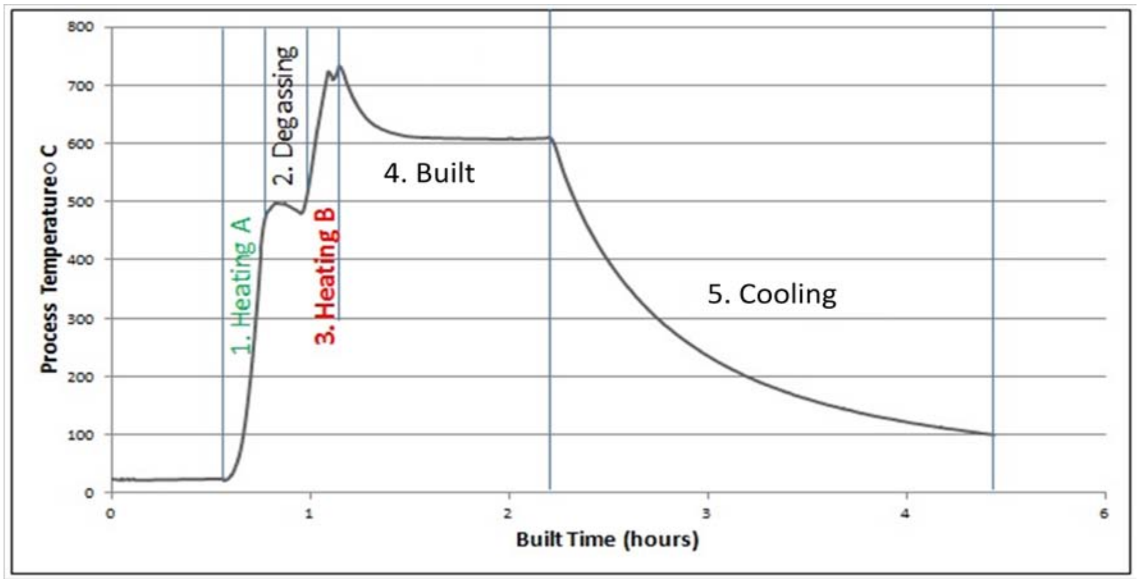

Figure 5.3 **EBSM build temperature versus time diagram obtained from the thermocouple located at the bottom of the build plate of the A2 Arcam system**

After the build plate pre-heating process is finished, the *z-axis* movement base is lowered 100 microns, and the first powder layer (with a powder thickness larger than 100 microns, considering the gap between the racking system and the racking surface seen in Figure 5.2) is placed by the racking system and subsequently pre-heated to induce a partial sintering, improving the thermal conductivity during the build and diminishing the possibility for particle charging and powder spreading [146]. Finally, the electron beam selectively melts the powder according to the build part geometry previously established (see Figure 5.4. for process steps) and layer by layer the build part is deposited until the part melting is finished, followed by a slow cooling process taking place under vacuum until the sample part reaches 100°C.

Processing times measured during each step of the EBSM build process are listed in Table 5.1:

Table 5.1. EBSM Processing time steps

Step	**Time (sec.)**
Powder Racking	7.5
Powder Heating and Pre-Sintering	10.5
Powder Melting (contour + area)	7.0

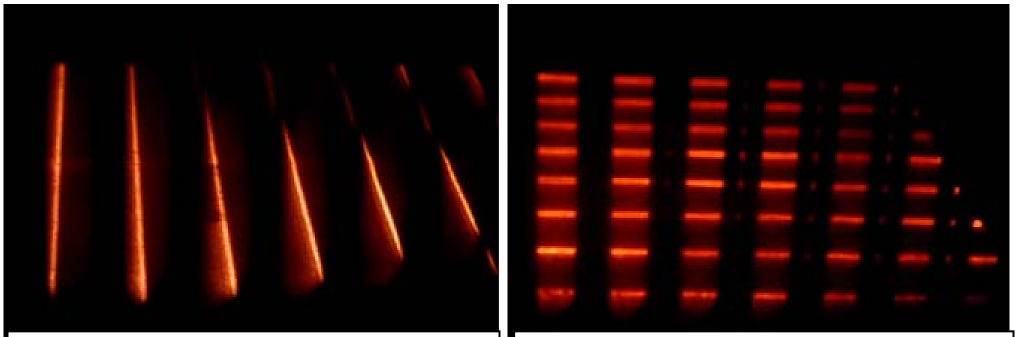

Powder heating and pre-sintering (vertical)

Powder heating and pre-sintering (horizontal)

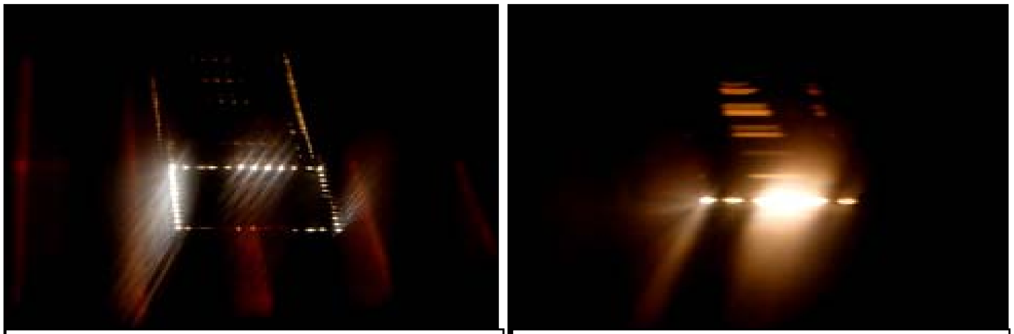

Sample contour melting

Sample inner volume melting

Figure 5.4. EBSM Process images taken from the view port though the radiation shield

As seen in Table 5.1, the overall process time per deposited layer was 25 seconds, at which time the *z-axis* movement base is lowered a distance of 100 microns and a new cycle of heating and melting starts. This time, the electron beam is oriented in an orthogonal direction in order to maintain heat distribution equilibrium. The same process cycle will continue 254 times, until the final sample height is reached.

5.2. Modeling the Physical Phenomena on EBSM Process

The physical phenomena complexity involved during the EBSM process such as the electron beam particle interaction, energy distribution through particulate media, capillary forces, wetting and de-wetting of the molten metal, powder melting and solidification shrinkage and heat transfer by conduction and radiation among others, requires a simplification in such a way that a numerical approximation can be used on the most influential process variables. Modeling the thermal evolution on a particulate media, with a size distribution, implies the numerical solution of large amounts of discrete domains (representing spherical particles) demanding enormous computing resources [65]; however *Winterberg* and *Tsotsas* showed that the powder material can be treated as a continuum media for thermal calculation purposes [147], thus, decreasing the amount of elements to only one domain, representing an individual powder layer. On the other hand, modeling the electron beam – powder interaction requires a different strategy enable to solve the movement of a molten metal at high scan beam speeds during the pre-heating and further melting of the powder material. With this purpose two alternatives were evaluated to simplify the effect of the electron beam over the powder surface as shown below.

5.2.1. EBSM Heat Source Discretization

<u>Volumetric Heat Source</u>

The first electron beam melting model strategy here presented, consist on the representation of the heat source as a discrete volume within the powder layer domain at temperature above the melting point. Once the powder layer has been discretized as a high conductive uniform layer, the selective melting area caused by the electron beam is depicted as an array of sub-domains called (*voxels*). Each *voxel* individually acts as a heat source, representing the melt pool location at a specific place in time with time-dependent boundary conditions. These sub-domains are subjected to a prescribed heat flux, ***Q,*** until the domain reaches the material melting point at an arbitrary temperature above the melting point, while the elements not yet melted were assigned a thermal conductivity of zero (k = 0). This boundary condition allowed the *voxel* domains to be solved only on the desired area.

The movement of the heat source in this model was obtained by coupling the dwell time of the individual cube at melting temperature followed by a cooling process representing the heat source no longer in that domain. Afterwards, a new element is activated for heating until reaching the melting point, repeating the process until the entire array is solved. Heat losses by conduction or radiation were not considered here, and only one powder layer represented as a continuous media was simulated.

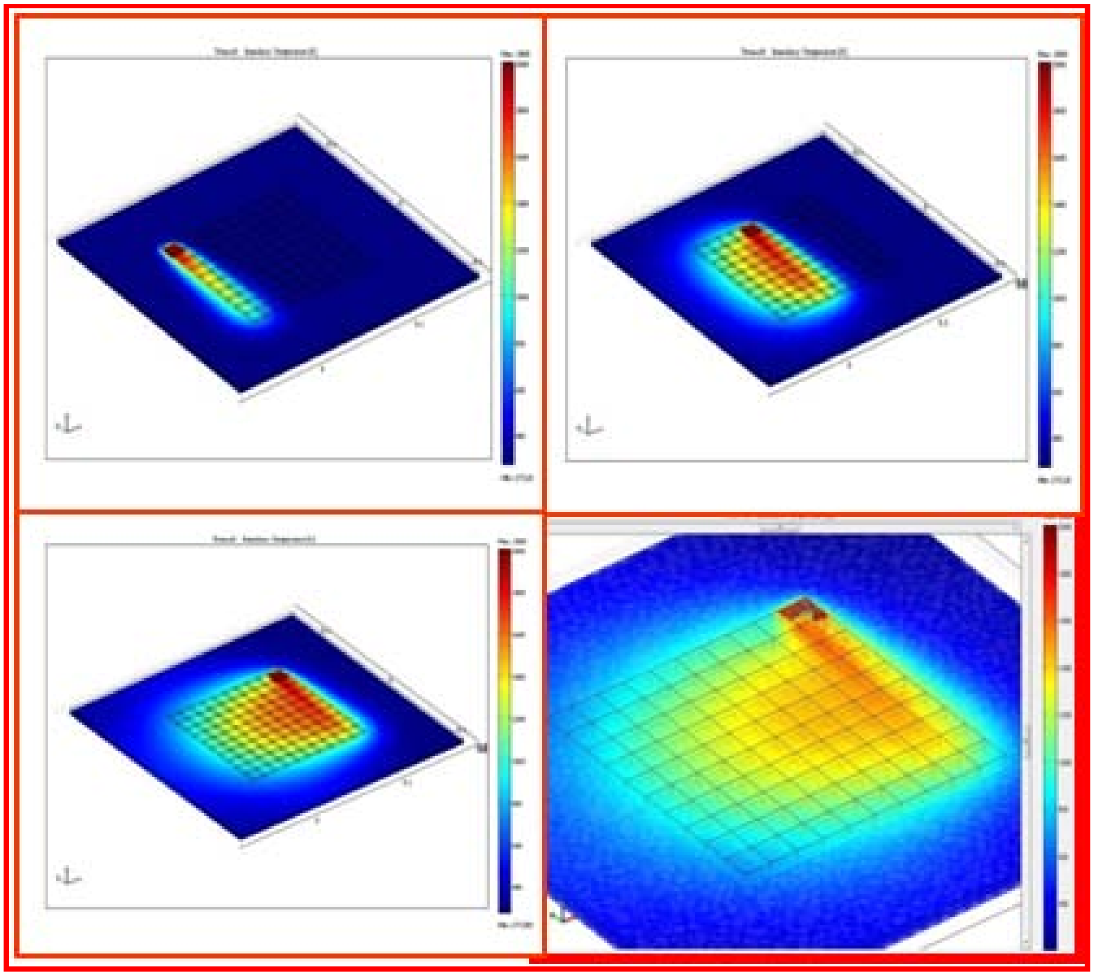

Figure 5.5. 3D - Step simulation on an array of elements called *voxels*. Heat evolution solving individual domains representing a moving heat source.

Initial results were obtained using three-dimensional, 10 by 10 cubic *voxel* array using the upper boundary as surface heat source. Every time a singular cube was solved, the respective integration result was saved in Comsol Multiphysics and later used as the initial condition for the next cube to be heated.

Even though modeling a moving heat source as a discrete volume is possible, a large computational resource is required to solve this type of model sequence since the whole domain must be numerically solved each time a new *voxel* domain is heated. To solve a large number of discrete elements, the Comsol Multiphysics file model was saved in *Matlab* format (*.m) and modified to run a *loop* subroutine in which a specific solutions at a prescribed time was obtained. This approach was found to decrease the modeling time, though only one solution for individual *voxel* cube is possible at a specific time. However, the use of this strategy to model a heat source requires the use of large computational resources, including additional sub-routines to model scan paths by activating or deactivating selective *voxels*. This voxel discretization will later prove to be inefficient to model EBSM process applications, since it comprises the solution of hundred of layers, translated into an order of magnitude higher amount of *voxels* to be built and solved individually.

Due to this limitation, it is then required to find a way to model a moving heat source with a high aspect ratio layer similar to the electron beam with no limitations in domain size, followed by a strategy to model the layer-by-layer process. This is the subject of the next section describing a method known as linear hear source modeling.

Linear Heat Source

The second strategy consisted of the combination of two types of domains, one representing the powder layer as a continuous domain and the second element is represented by a one dimensional element depicting the electron beam high aspect ratio penetration into the powder with a length equal to the layer thickness (100 microns). The heat transfer model was then resolved as a numerical integration of a moving linear heat source that is temperature- and time-dependent. This is a more versatile model for an electron beam process simulation, in which scan trajectories can be customized to better fit the sample geometry requirements. As an output, results, temperature distribution through the powder layer was obtained.

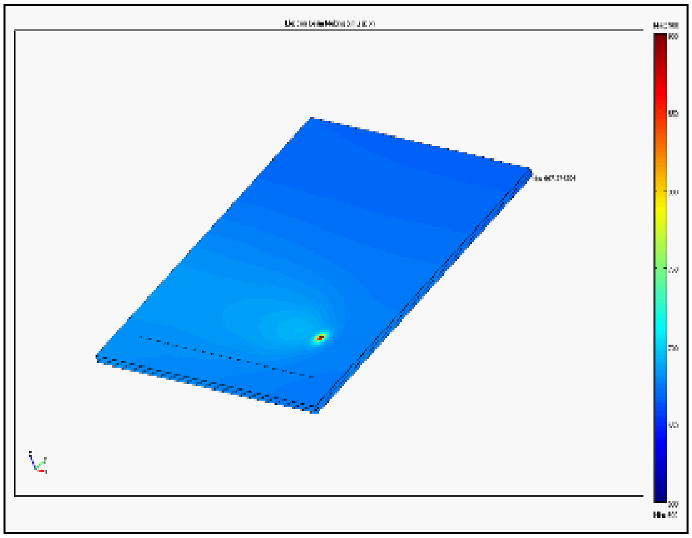

Figure 5.6. Comsol multiphysics graphical representation of a line heat source model moving trhough the continuous powder media

The layer by layer process

Once a feasible approximation of the electron beam heat source and its movement along a singular representation of a powder layer is been determined, there is still an additional limitation to the model regarding the ability to solve multiple layers. To solve this, initially all the continuous powder layers were staked on the model, and only the first layer is assigned with thermal conductivity values different from zero, assigning the remaining layers with thermal isolation values (thermal conductivity equals to zero), representing the non-yet deposited material.

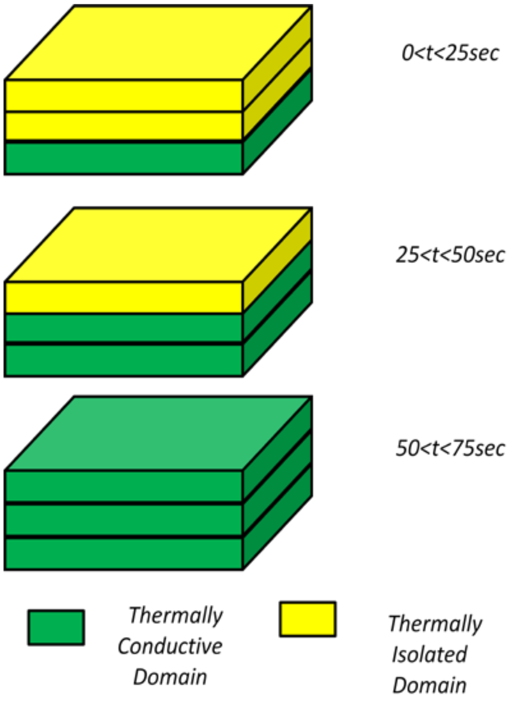

Figure 5.7. Graphical representation of the multilayer domain time-dependent thermal activation

As previously described in Table 5.1 each layer deposition, preheating and melting, lasts a period of 25 seconds, for which an initial solution for the first layer is obtained and saved as initial conditions for the process of the subsequent layer for which at *t >25 seconds,* thermal conductivity values different from zero are assigned. In this manner, each layer is subsequently activated as the additive process progresses. This time dependent model solution was possible by using a similar approach developed on the volumetric heat source, to numerically solve individual *voxels* consisting on the use of a for loop function in *Matlab* file containing the

Comsol model information. This for loop option makes possible to control the thermal conductivity in intervals of 25 seconds, assigning layer by layer thermal conductive values as they progress during the build.

5.3. Material Properties

The material properties pertaining the thermal modeling of Ti6Al4V during the EBSM process were previously measured in chapter 3, in powder and electron beam processed solid state. For the ease of the model, the results were used as a set of temperature dependant polynomial functions representing the thermal behavior of this alloy including their linear fit values. Remaining information required to complete the material data set for the model was also included from literature for heat capacity of molten Ti6Al4V as well as density values for solid as liquid state [78] and the thermal conductivity and spectral emissivity in liquid state [119] as seen in Table 5.3.

Values for heat capacity, thermal conductivity and density for the stainless steel (SS-316) build plate were obtained from *Song et al.* [148] and shown in Table 5.2; where only heat losses by conduction and no by radiation, were included.

Table 5.2. Thermal properties for Stainless Steel 316 at Different Temperatures (20<T<1000°C). Adapted from [148]

Property	***Polynomial Function (y = A + B*T + C*T² + D*T³)***	***Linear Fit (R²)***
Heat Capacity (J/g.K)	$C_p = 0.02283 + (0.01547)T(°\mathrm{C}) - (7.50298 * 10^{-5})T^2(°\mathrm{C}) + (9.23922 * 10^{-8})T^3(°\mathrm{C})$	*0.97*
Thermal Conductivity (W/m.K)	$k = 47.9219 - 0.0447T(°\mathrm{C}) - (4.1206 * 10^{-5})T^2(°\mathrm{C}) + (8.48165 * 10^{-8})T^3(°\mathrm{C})$	*0.98*
Density (g/cm³)	*7.8*	--

Table 5.3. Recommended values for Ti6Al4V in the form of temperature dependant polynomial functions

Property	*Material State*	*Temperature Range (°C)*	*Polynomial Function ($y = A + B*T + C*T^2 + D*T^3$)*	*Linear Fit (R^2)*
Heat Capacity C_p (J/g.K)	*Powder*	*23<T<1650*	$C_p = 0.52036 - (8.34 * 10^{-6})T(°\text{C}) - (4.46 * 10^{-7})T^2(°\text{C}) + (5.44 * 10^{-10})T^3(°\text{C})$	*0.98167*
	Solid	*23<T<1650*	$C_p = 0.54058 + (1.02 * 10^{-4})T(°\text{C}) + (1.35 * 10^{-7})T^2(°\text{C}) - (6.50 * 10^{-11})T^3(°\text{C})$	*0.99645*
	Liquid [78]	*1650<T<1950*	*0.83*	--
Thermal Conductivity k (W/m.K)	*Powder*	*23<T<1650*	$k = 0.9315 - 0.00339T(°\text{C}) + (6.55 * 10^{-6})T^2(°\text{C}) - (1.41 * 10^{-9})T^3(°\text{C})$	*0.9894*
	Solid Parallel	*23<T<1650*	$k = 6.95757 + 0.00224T(°\text{C}) + (1.69 * 10^{-5})T^2(°\text{C}) - (7.58 * 10^{-9})T^3(°\text{C})$	*0.99138*
	Solid Orthogonal	*23<T<1650*	$k = 8.23346 - 6.30 * 10^{-3}T(°\text{C}) + (1.43 * 10^{-5})T^2(°\text{C}) - (2.97 * 10^{-9})T^3(°\text{C})$	*0.94678*
	Liquid Metal [119]	*1650<T<2700*	$k = -1.6614 + 0.0183\, T(°\text{C})$	*1.0*
Emissivity (ε)	*Melt pool front*	*23<T<1650*	$\varepsilon = 0.43356 + (2.94 * 10^{-4})T(°\text{C}) + (5.48 * 10^{-7})T^2(°\text{C}) - (5.53 * 10^{-10})T^3(°\text{C})$	*0.98625*
	Particle contact area	*23<T<1650*	*0.83*	--
	Powder	*23<T<1650*	*0.6*	--
	Melt Pool Front [119]	*1650<T<2700*	*0.4*	--
Density ρ (g/cm³)	*Powder and Solid[78]*	*23<T<1650*	$\rho_{solid} = 4.42 - 0.154\ (T - 25°\text{C})$	*0.96*
	Liquid[78]	*1650<T<2000*	$\rho_{liquid} = 3.920 - 0.68\ (T - 1650°\text{C})$	*0.98*

5.4. EBSM System Model Idealization using Comsol Multiphysics

The heat source is defined as an e-beam with sufficient current and voltage to penetrate the powder material and transfer enough energy to melt the powder and fuse the molten layer to preceding layers and previously discretized as a liner heat source. The starting material was defined earlier as an aerospace titanium alloy powder (Ti6Al4V) made from a PREP process. The powder is loosely packed together, as a result of the raking process during the spreading phase, and partially sintered after being pre-heated in the Arcam A2 system, discretized for modeling purposes as a continuous media described by a uniform domain representing an individual powder layer. The process environment surrounding the build is under vacuum conditions eliminating any convective heat flow calculations in the model, making the simulation simpler to compute. The system model representation in Comsol Multiphysics is composed by:

a. A domain representing the *base Ti6Al4V powder* in which the build plate is resting.
b. The *build plate*, a 316L stainless steel plate loosely supported by the *base powder.*
c. A point element is used to represent the thermocouple reading at the bottom of the build plate.

d. A thin layered domain representing the powder material to be placed on top of the build plate that will be slightly sintered after the pre-heating step.

e. The last element emulates the transition between the *presureless* sintered powder followed by melting and solidification. This is possible using the temperature-dependant properties evaluated in chapters 3 and 4 and later listed in Table 5.3.

A total of 254 elements of the *d* and *e* type with 100 micron thickness is respectively modeled and numerically solved and the whole element stack can be seen in Figure 5.8.

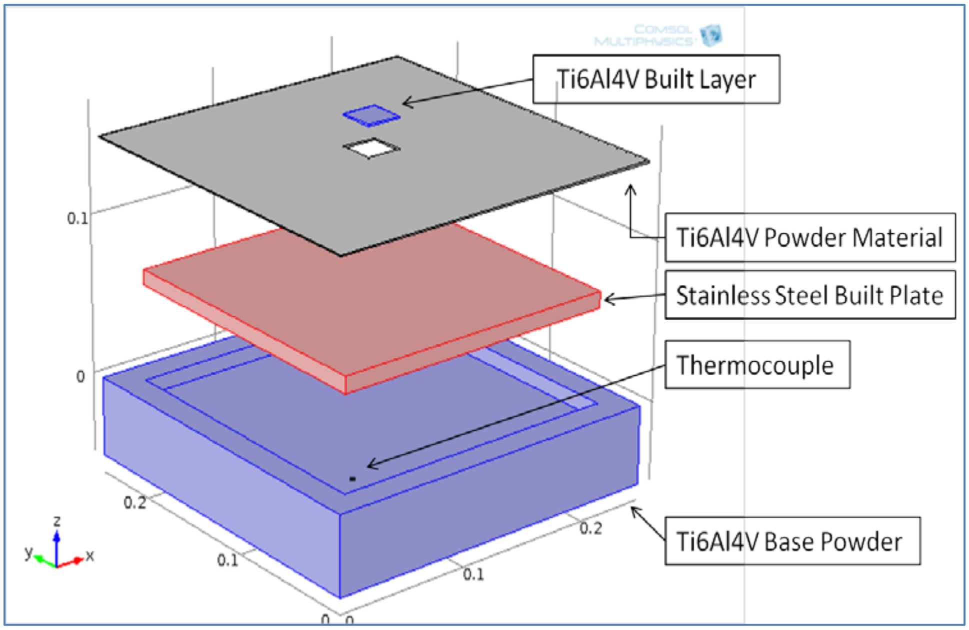

Figure 5.8. Comsol Multiphysics geometry construction for FEA analysis

The scan path of the linear heat source is given by a series of time dependent three dimensional vector coordinates depending on time and scan velocity (Figure 5.9.).

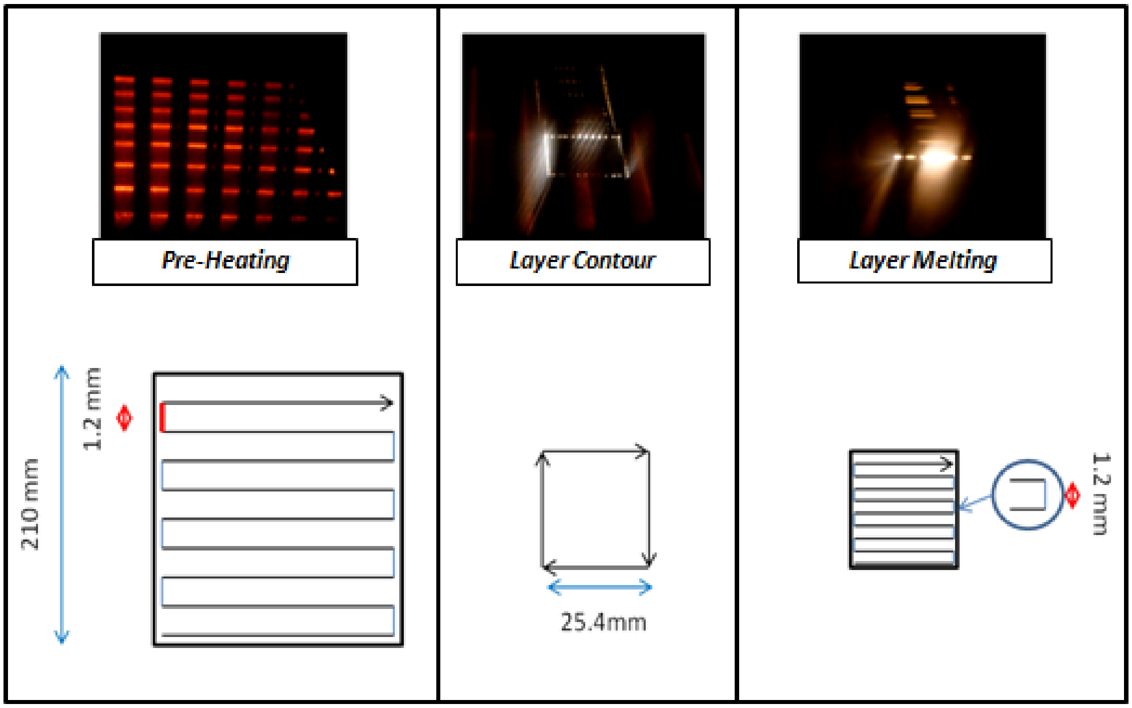

Figure 5.9. Electron Beam scan path

The scan path depicted on Figure 5.9., is based on a time dependant square wave function with a 1.2mm hatch, representing the trajectory of the electron beam and applied initially to the whole powder area for pre-heating at low power conditions and later at a higher powder and reduced area for the selective melting process.

This intermediate process is carried out by using the edge coordinates of the square build as a function of time.

Figure 5.10, shows the EBSM process been subdivided in 5 different steps. Steps 1 through 3 correspond to the stainless steel build plate heating and degassing setting up the system for the initial process conditions at 734°C. Subsequently, step 4 corresponds to the actual material deposition layer by layer followed by a cooling process depicted as a step 5.

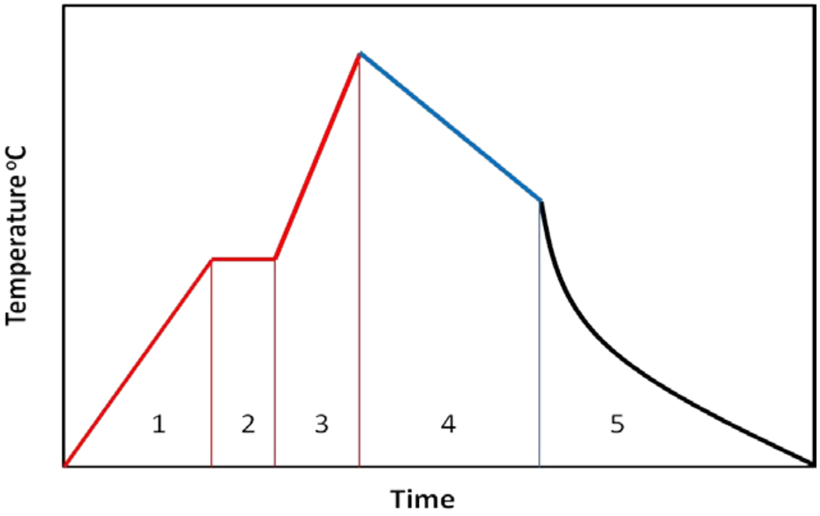

Figure 5.10. EBSM temperature distribution as a function of time

Thermal analysis is performed by a transient numerical solution of the EBSM process; thereby the data temperature log obtained from the thermocouple located at the bottom of the build plate (previously seen in Figure 5.3) was used to estimate the overall additive process time at each step o time is shown in Table 5.4.

Table 5.4. EBSM process time values required to manufacture a (1in^3) Ti6Al4V cubic sample. (Data extracted from the thermocouple temperature control system in the Arcam A2 equipment)

Step	Process	Process Time in seconds	Time in hours
1	*Pre-Heating*	*1029*	*0.29*
2	*Degassing*	*677*	*0.19*
3	*Pre-Heating*	*725*	*0.20*
Total Pre-Heating Time		*2431*	*0.68*
4	*EBSM Build*	6350	1.76
5	*EBSM part Cooling*	9624	2.67
Total Comsol Model Time (Step 4 + Step 5)		15974	4.43
Total Process Time		18405	5.11

Taking into account the EBSM total process time (~5 hours) to be numerically solved, the model was divided into three sections: pre-heating (including steps 1 through 3), part build or melting for step 4, and cooling for step 5. In order to decrease the modeling time, the pre-heating of the base powder and built plate was not simulated by the movement of the linear heat source over the build plate surface, instead the temperature profile was set as initial conditions by a time dependent function depicting the heating process, in order to setup reliable initial conditions for the simulation prior the first and consecutive powder layer spreading and selective melting. Partial solutions *(individual layers)* contained in step 4 were numerically solved and later on saved as initial conditions for the subsequent process steps. Finally, once the simulation was solved by a *Matlab* code loop, the whole domain was left to cool down as depicted by step 5 for the same amount of time as recorded during the experimental Arcam process temperature in-situ monitoring data previously shown in Figure 5.3.

5.5. Mathematical - Physical Model

The temperature distribution within the modeled domains is given by the general heat transfer equation. This model represents a physical system in which properties depend on location (x, y, z), time, and temperature. The inclusion of two or more independent variables to equation (5.1) results in a partial differential equation. This multidimensional heat diffusion equation in a cartesian coordinate system can be initially written as:

$$\rho c_p \frac{\partial T}{\partial t} = div\left[(k) grad(T)\right] + Q \tag{5.1}$$

and due to its temperature interdependencies re-written as:

$$\frac{k(T)}{\rho(T) C_p(T)}\left(\frac{\partial^2 T}{\partial x^2}+\frac{\partial^2 T}{\partial y^2}+\frac{\partial^2 T}{\partial z^2}\right)+\frac{Q^*(x,y,z,t)}{\rho(T) C_p(T)}=\frac{\partial T}{\partial t}+v_{heat\ source}\frac{\partial v}{\partial x} \tag{5.2}$$

where:

$k = Thermal\ conductivity$

$\rho = Density$

$C_p = Heat\ capacity$

$T = Temperature$

$t = Time$

$Q_{beam} = Moving\ heat\ source$

$v = Heat\ source\ rastering\ \ velocity$

$(x, y, z) = Cartesian\ coordinates$

Instead of represent an variable electron beam density by a Gaussian distribution function, due to scarce information related with the energy distribution in this EBSM system, a uniform energy distribution for a electron beam over the material surface is been experimentally determined by *Mahale* [149] and depicted by the following equation:

$$Q_{eff} = \frac{\pi \times v_{acc} \times I_{scan} \times \gamma_{abs}}{4 \times d_{beam} \times V_{scan}} \tag{5.3}$$

This energy density corresponds to the effective energy value located at the surface of the material or in our case, at the top of the linear heat source and its distribution or attenuation by the particulate media is given by the exponential Beer-Lambert electron beam energy absorption law [150], where the absorption depth $-\lambda_{abs}$ found in titanium alloys is 0.125 microns[62].

$$\frac{dQ}{dz} = -\lambda_{abs} Q_{eff} \tag{5.4}$$

The absorbed power $\gamma_{abs} = 1 - \varepsilon_{back}$, and the values for the Q_{eff} variables are given by:

Table 5.5. EBSM electron beam process conditions setup

Term	Symbol	Value
Acceleration voltage (kV)	v_{acc}	60
Current (mA)	I_{scan}	37.5
Scan melting speed (mm/sec)	$v_{scan-melting}$	223.7
Scan sintering speed (mm/sec)	$v_{scan-sintering}$	1077.3
Delivered Power (kW)	P	2.25
e-beam diameter(μm)	d_{beam}	100
Melt pool diameter (mm)	d_{pool}	1.2
Beam off-set	X	1.2
e-back scattering	ε_{back}	0.0025
Absorption percentage	γ_{abs}	0.9975

Radiation losses are calculated by using the following equation:

$$q = A\varepsilon\sigma(T^4_{radiation\ shield} - T^4_{built}) \tag{5.5}$$

$A = Surface\ area$

$\sigma = Stefan - Boltzmann\ constant$

$\varepsilon = Emissivity$ for powder and solid material

$T_{radiation\,shield} = Radiation\ shield\ temperature$
$T_{built} = Built\ temperature$

$\boldsymbol{Q}$ corresponds to the heat flux during the process, and includes the powder surface area as a function of temperature; $\boldsymbol{\sigma}$ is the Stefan-Boltzmann-constant (σ = 5.67 X 10^{-8} W/(m^2 K^4); ε is the powder emissivity as a function of temperature (described and characterized on chapters 3 and 4); $\boldsymbol{T_{build}}$ is the part temperature; and $T_{radiation\ shield}$ is the ambient process temperature, in this case set at 893K (620°C), which is close to the build temperature.

5.6. Boundary and Starting Conditions

Once the process elements to be modeled have been identified and properly discretized, some boundary conditions need to be set in order to solve the partial differential equations previously presented. For prescribed temperature values, a room temperature T_{init} = 296K (23°C) was assigned to all domains for the starting temperature at t = 0 on process step 1. A temperature T_{start} = 1007K (734 °C), was assigned to the build plate after the plate heating process step 3 concluded. Heat losses by conduction were considered between vertical domains representing each layered step. Losses by radiation where assigned according to the density of the material (sintered powder vs. solid material) and sequentially solved at the top boundary of each layer and the boundaries containing the base powder material (see Figure 5.11).

Temperature-dependent properties for Ti6Al4V such as density, $\boldsymbol{\rho}$, heat capacity, $\boldsymbol{C_p(T)}$, and thermal conductivity, $\boldsymbol{k(T)}$, previously measured were used to solve the heat transfer equation using a piecewise function which included the polynomial fits obtained in sections 4.1and 4.3.

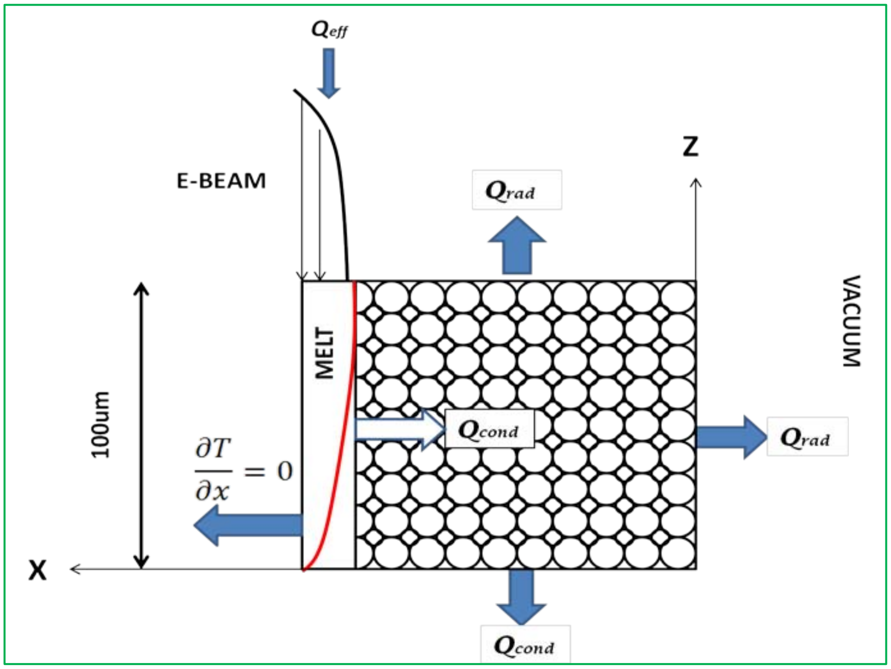

Figure 5.11. Graphical representation of the boundaries conditions used during the model and simulation of the EBSM process

The anisotropic behavior of the solid Ti6Al4V metal in thermal conductivity was solved using a [3x3] matrix array according to data obtained in section 4.3.3. Heat flux for the boundary between the layered powder and the solid sample build was set identically. This consideration assumes an identical temperature where $Q_{(powder)} = Q_{(solid)}$ at the boundary between the build solid and the surrounding powder, but different temperature gradients will be obtained due to dissimilar thermal conductivity values. Additional thermal properties for the stainless steel material are included in the model from data previously reported by *Zäh* and *Song* et al. [64, 148] and later shown in Table 5.2.

5.7. Comsol Multiphysics Setup

5.7.1. Model Meshing

The high aspect ratio of individual layers to be modeled, make the use of triangular and tetrahedral meshes not converging within the discretized element. Instead, a swept mesh was used by the generation of hexahedron elements. This element operates on a three-dimensional domain by meshing a source face and then sweeping or extruding the resulting face mesh along the domain oriented towards an opposite destination.

5.7.1. Numerical Solver

Considering the large amount of data involved in this computational analysis, a time dependent parallel sparse direct solver was used (Multifrontal Massively Parallel sparse direct Solver-*MUMPS*), to solve the temperature evolution during the EBSM process. Time steps were set at 0.1 seconds although a free time step backwards differentiation formula method BDF was chosen for been more stable and versatile than generalized alpha[151].

5.8. Post -processing Data and Results

Post-processing data obtained by Comsol simulation corresponds to the transient solution of the temperature during the EBSM process. The thermal distribution values are displayed in different directions of the discretized element and the solution for the point element depicting the location and reading of the thermocouple used for process control during the EBSM manufacture is displayed at the top right corner to be later compared with the process thermocouple data for validation purposes.

Initially, as seen in section 5.4 a prescribed heating ramp was evaluated for a period of 2431 seconds, modeling process steps 1 through 3 (see Table 5.4), to determine the thermal gradient present at the additive process initial conditions set at (734°C) prior to the powder spreading according to Figure 5.12. Later Figure 5.13, shows the results for the temperature evolution in a period of 6350 seconds, corresponding to 254 additive layered events spending 25 seconds per layer. Even though the cooling process took 9624 seconds (see), an instantaneous image was taken at t= 4900 seconds, enabling to observe the thermal gradients taking place during the cooling process until it reaches a value of 100°C as seen in Figure 5.14.

Initial temperature profile after built plate heating (Process Steps 1 through 3)

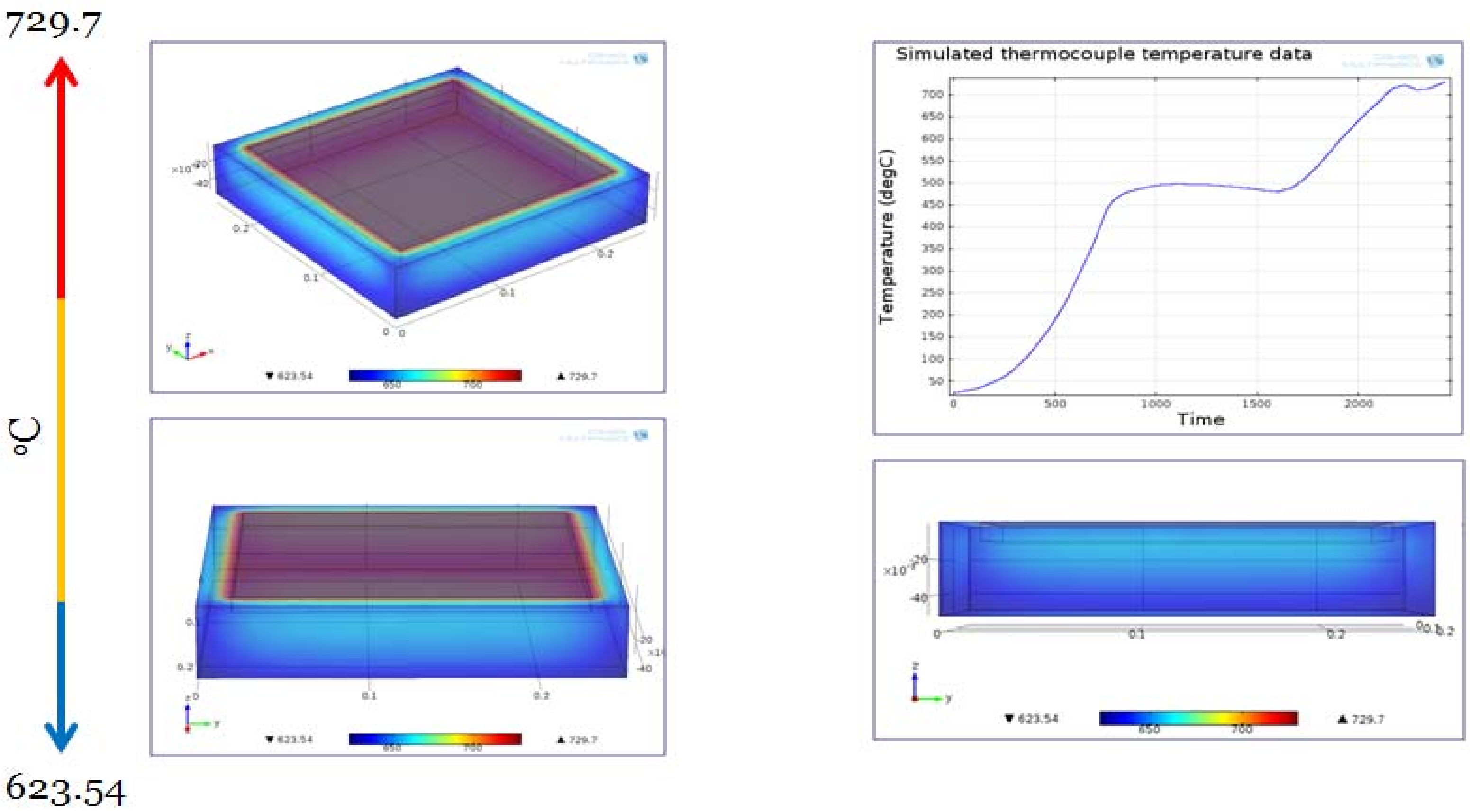

Figure 5.12. **Simulation results at time (Tpre-heating= 2431 sec; 40.51 min) for initial pre-heating of the built plate and base powder material.**

Thermal profile during layer-by layer deposition (Process Step 4)

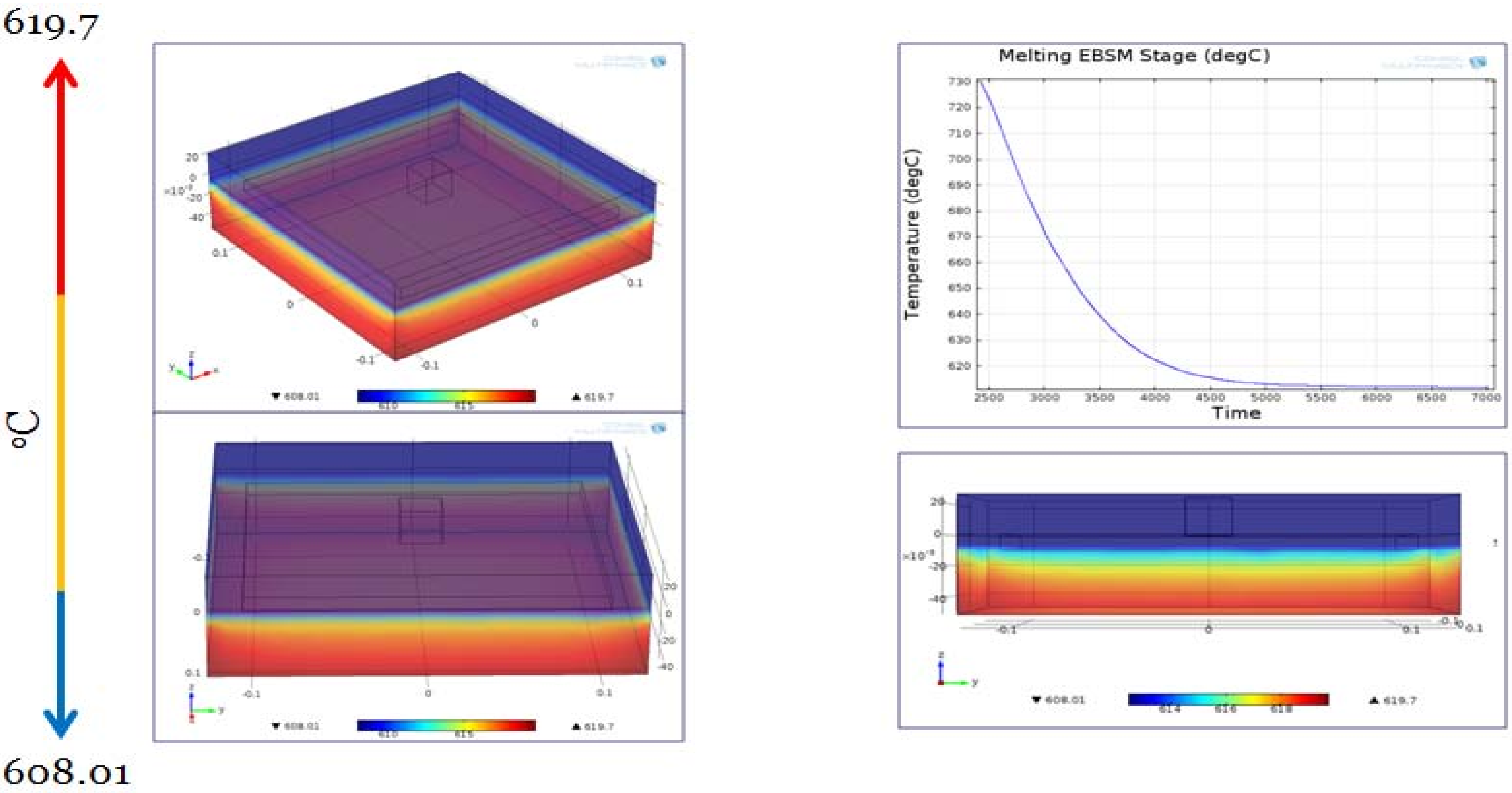

Figure 5.13. Final solution at the end of the EBSM melting process step at time (Tmelting=6350 sec; 1.76 hrs)

Temperature profile for sample cooling (Process Step 5)

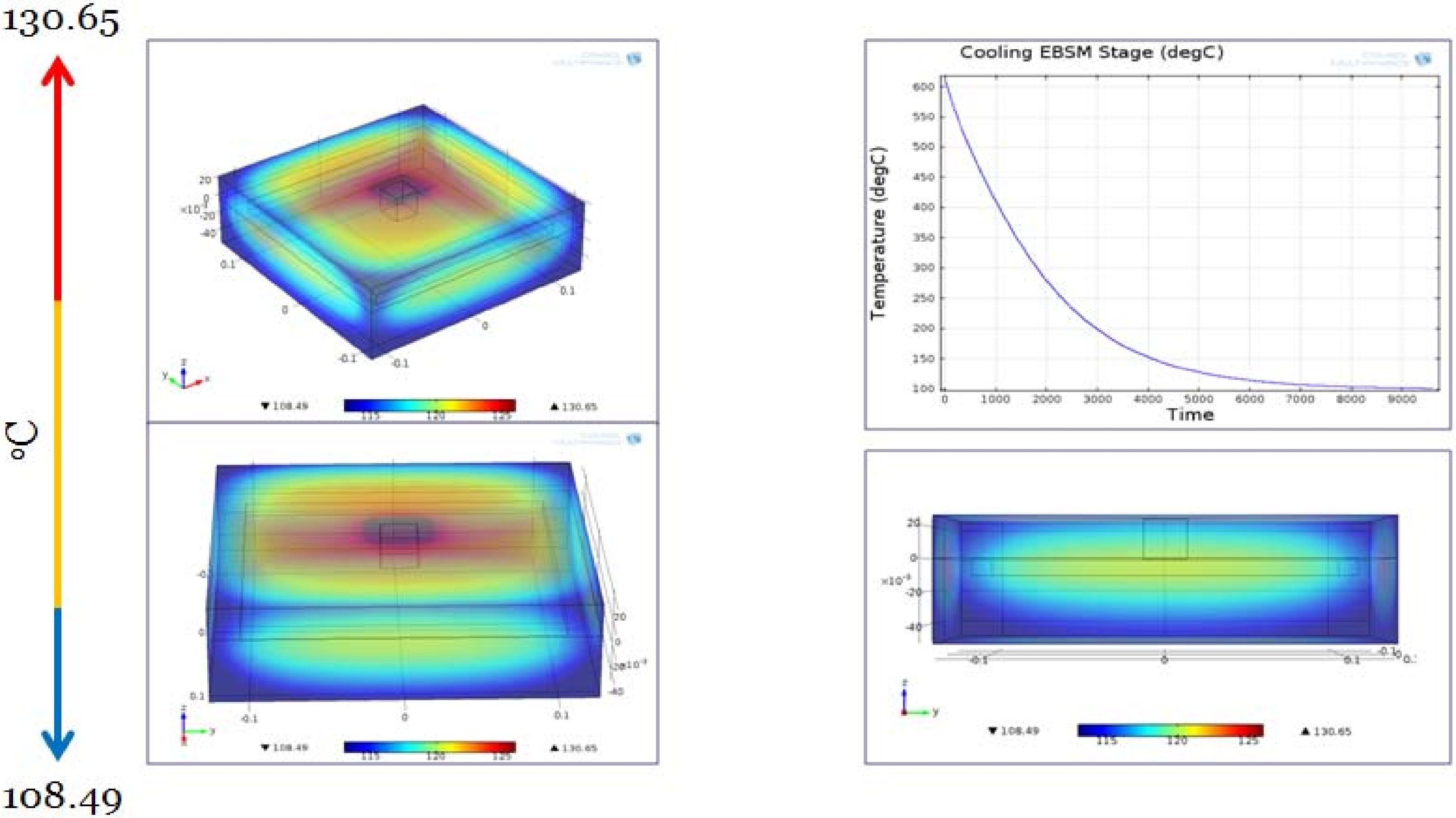

Figure 5.14. Cooling process image taken at ($T_{cooling}$*=4900sec)* into the simulation

5.9. Model Validation

5.9.1. Validation using process monitoring EBSM data

To properly validate the electron beam assisted rapid prototyping model, process monitoring data from a type K thermocouple, located at the bottom of the build plate was used to monitor the temperature during the entire process. As seen on Figure 5.17, once the start temperature was set at 734°C, it quickly decreased until it reached a stable temperature around 610°C due to a lesser power input to the system by the layer by layer process. The build then started, and 254 layers of material were deposited, layer by layer, until the final sample height was obtained. The build protocol consists of powder spreading, then powder heating (partially sintered), a contour of the sample is melted, and finally the interior of the contour is melted as well. The beam orientation was perpendicular each time a new layer was built in order to maintain temperature uniformity.

Steps 1 through 3, illustrated in Figure 5.15 are conducted to initially degas the build plate surface to avoid any further contamination within the system. Water begins to outgas from particle surfaces at roughly 75°C, and reaches a maximum rate at ~150°C. This maximum outgassing rate remains constant up to 300°C, depending on the powder surface area and the condition in which the powder had been handled. At 475°C, hydrogen starts to outgas and reaches a maximum rate at 575°C. The maximum hydrogen degassing continues to temperatures up to 635°C [102].

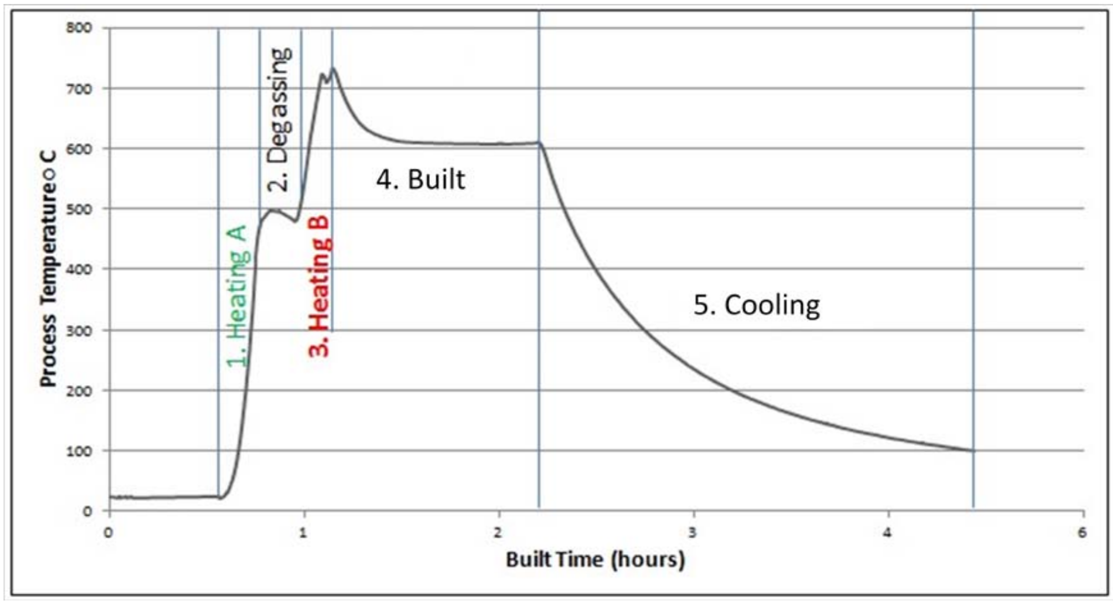

Figure 5.15. Temperature profile extracted from the A2 Arcam system using a thermocouple located at the build plate bottom.

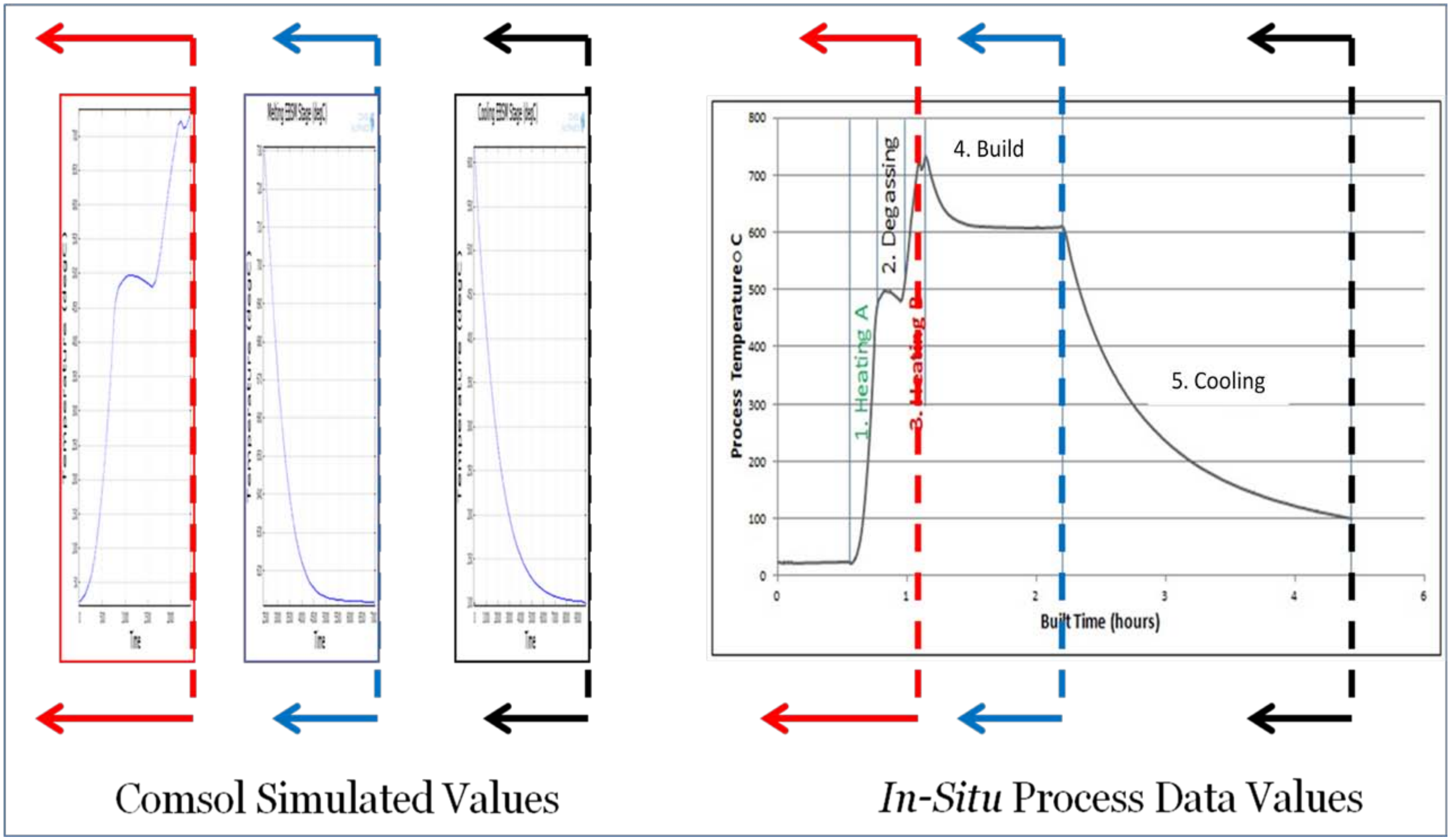

Figure 5.16 Simulated Values comparison with *in-situ* temperature measured process data from the EBSM system

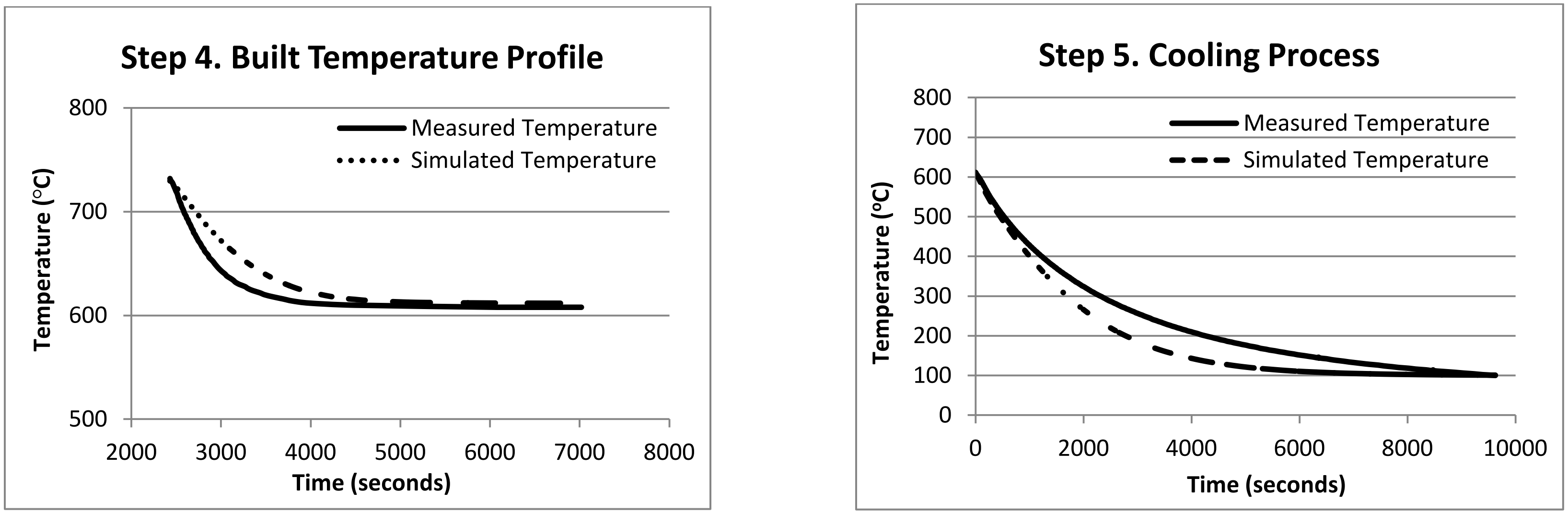

Figure 5.17. Measured and simulated temperature data for melting and cooling Ti6Al4V EBSM process

As observed in Figure 5.16 and Figure 5.17, data obtained by modeling and simulating the three main components during the EBSM built were in agreement to the experimental data. Factors' limiting the accuracy of the model resides on the limited temperature control on different locations within the system directly affecting the heat transfer during the EBSM build and cooling process. Only heat losses by radiation where included in the model between the surrounding powder material and the vacuum system, disregarding the action of the build tank as a heat sink. The evaluation of heat losses by radiation on the melt pool front (*z-axis direction)* was not possible due to the pile-up of the layers thermally isolated thereby hindering the heat losses in that direction. Moreover, the effect of the heat radiation shield located at the top of the build plate, was not included due to limited *in-situ* process control data in the system.

5.9.2. Validation through simulation of an atmospheric plasma torch

Modeling the electron beam melting process as a discretized moving heat source can be a laborious task for numerical validation in view of the difficulty on *in-situ* process data available during the process. Thus, a step towards developing a reliable model was taken by setting up a controlled experiment using a different heat source (an atmospheric plasma system) where all the necessary measurements could be obtained and the proposed model could be effectively used and evaluated.

The Plasma Torch System

Atmospheric plasma torches operate by applying an electric current energy to a gas phase producing ions and excited species[152]. The gas phase used in this particular plasma system consisted of low pressure compressed air and is currently used for paint removal on metal surfaces of naval and air vessels, as a replacement from conventional methods like grit blasting [153].

The thermal evolution of this system and its application on metal surfaces is a matter of study, whereby the modeling and simulation can elucidate how much heat builds up on the surface and how deleterious this raise in temperature can be to the metal mechanical properties and corrosion resistance. The system used was a compressed air PlasmaFlux™ (PF-5000) system activated by an electrical source with 100 kHz in frequency and approximately 1 kW in delivered power[154, 155].

Validation Setup

A steel plate (150x 100 x 6.35 mm) was used as a substrate material to be heated by an atmospheric pressure plasma torch system. Two tests were conducted, in order of complexity. First, a static heating was performed in the center of the plate and the temperature was measured by an array of 5 thermocouples (type K) placed on the back of the plate. The plasma heat source was kept on for approximately 400 seconds, and the thermocouple readings are shown in Figure 5.18.

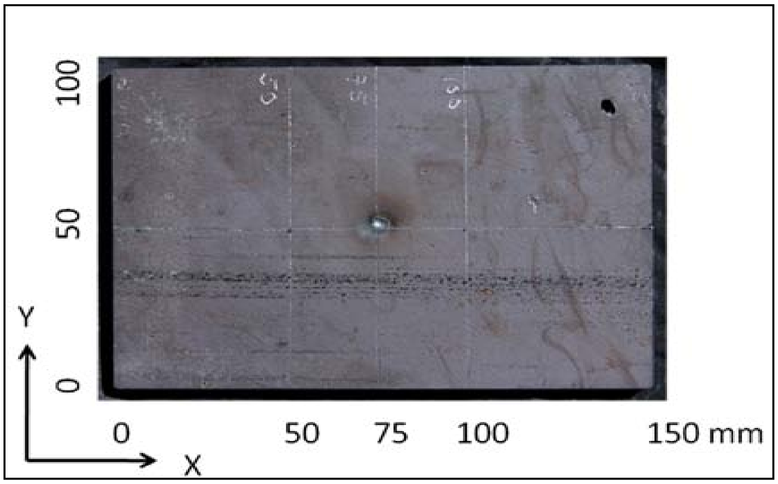

Figure 5.18. Steel plate material used for the plasma heating static test

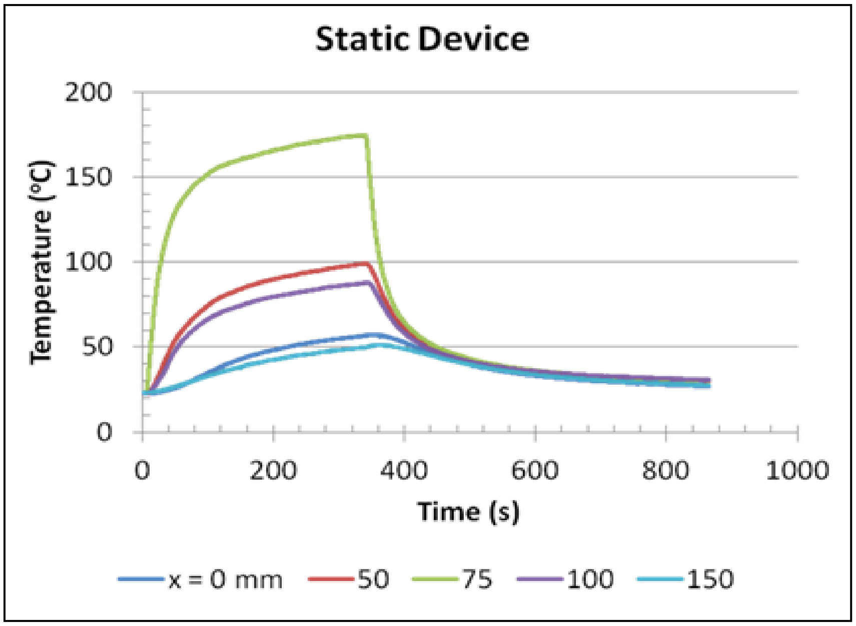

Figure 5.19. Temperature profile obtained from the 5 thermocouples during the static atmospheric plasma torch heating test.

The thermal reading, seen in Figure 5.19, shows the temperature gradient between the center of the plate (located at position 75 mm) and the edges of it (position 50, 100 mm and 0, 150 mm).

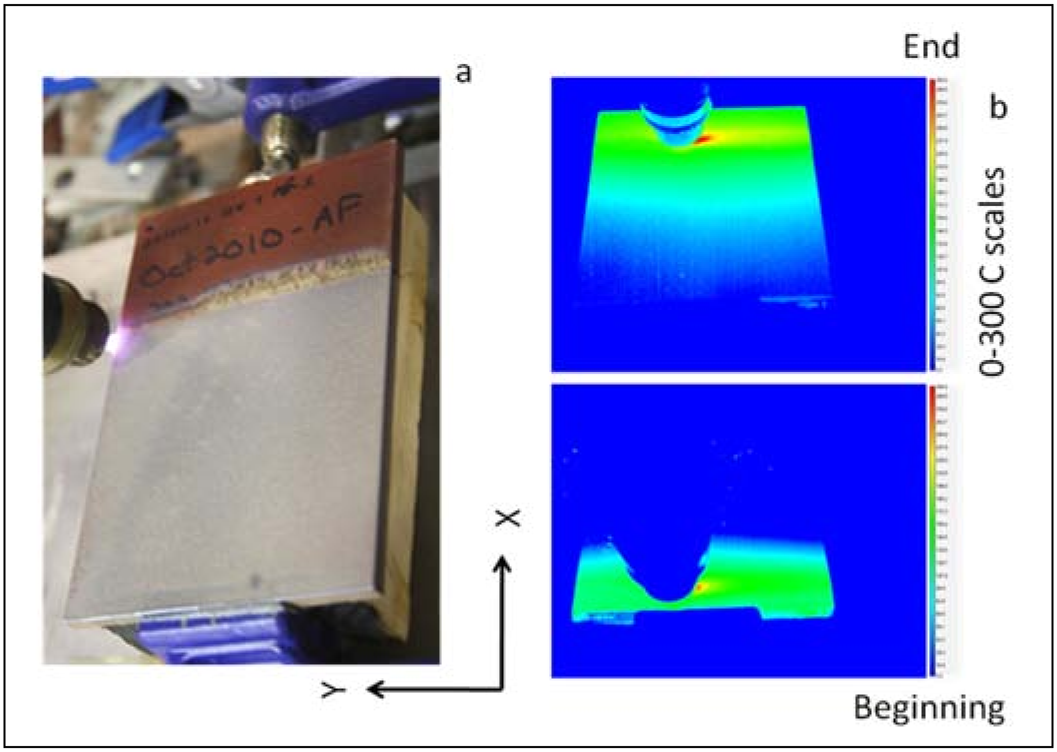

Figure 5.20. Atmospheric pressure plasma torch heating. a. Plasma scan over the steel plate; b. Infrared image from start to finish of the heating process.

The second test seen in Figure 5.20 consisted of heating a plate with the same dimensions of the first, this time following a square sine wave scan pattern with 1mm hatch distance for 500 seconds at a speed of 30 mm/ sec. Thermocouples were located in the same position as the previous test, and the time dependant T(t) thermal profile is shown in Figure 5.21.

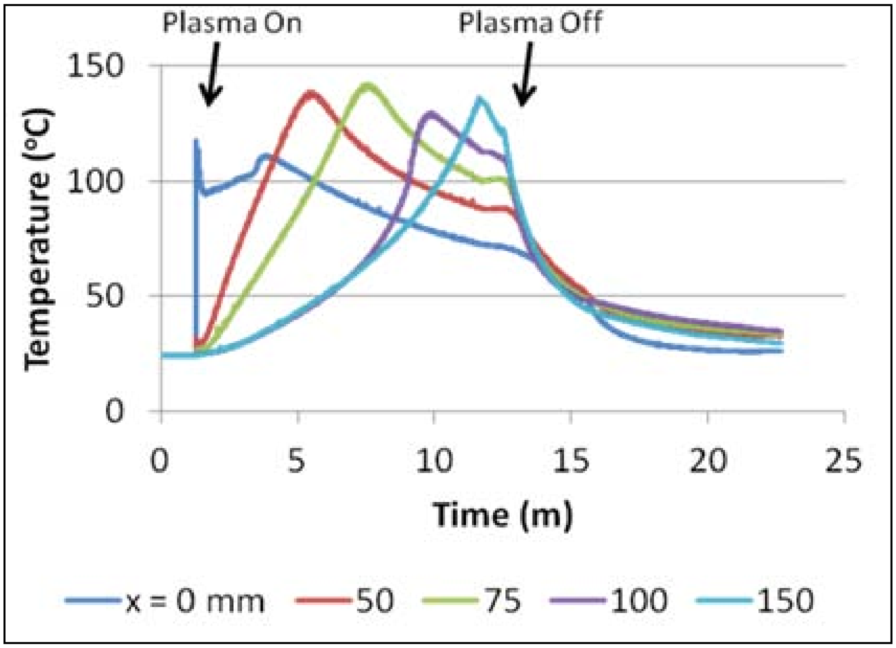

Figure 5.21. Temperature measurement for multi-pass plasma heating on steel plate

It can be observed where the plasma system start to operate and subsequent temperature peaks are registered due to the plasma movement. It can also be noted a fast cooling after the plasma torch leaves the heated area.

Model Idealization

For this numerical model, the plasma – surface interaction with the metal surface was not taken in consideration; instead a 2D surface heat source was prescribed to be numerically solved by COMSOL Multiphysics. The movement of the plasma was reproduced by a time-dependant square wave function, and heat losses by radiation and convection were taken into consideration. No heat-dependent material properties for steel were included in the model.

Mathematical – Physical Model

A transient heat transfer equation is solved along the prescribed domains of the plate based on equation (5.6).

$$\rho c_p \frac{\partial T}{\partial t} = div\left[(k) grad(T)\right] + Q* \tag{5.6}$$

Where:

$k = Thermal\ conductivity$

$\rho = Density$

$C_p = Heat\ capacity$

$T = Temperature$

$t = Time$

$Q^* = Moving\ heat\ source$

The heat source for a plasma system is represented by a 2D Gaussian distribution of energy, in the form of:

$$Q(x, y) = \frac{q}{2\pi\sigma^2} \tag{5.7}$$

Where,

$q = net\ heat\ input\ per\ unit\ time\ (power)$

$\sigma = Distribution\ parameter\ (half\ width\ of\ the\ arc)$

For radiation and convection heat losses we have,

$$q = A\varepsilon\sigma(T_{ext}^4 - T_{plate}^4) \tag{5.8}$$

$$\frac{dQ}{dt} = Q^* = h.A\ (T_{ext} - T_{plate}) \tag{5.9}$$

Where,

$\rho = Density$

$\varepsilon = Emissivity$

$T_{ext} = Temperature\ of\ the\ environment$

$T_{plate} = Plate\ temperature$

$h = Convection\ coeficcient$

$A = Surface\ area$

Boundary and Starting Conditions

Steel values used to solve the heat transfer equation were extracted by the literature. Heat capacity 440 J/kg.K, thermal conductivity *k*= 76.2 W/m.K and density 7870 kg/m^3 [156]. The initial temperature for the plate was also set to T_o = 25 °C.

Post-processing data

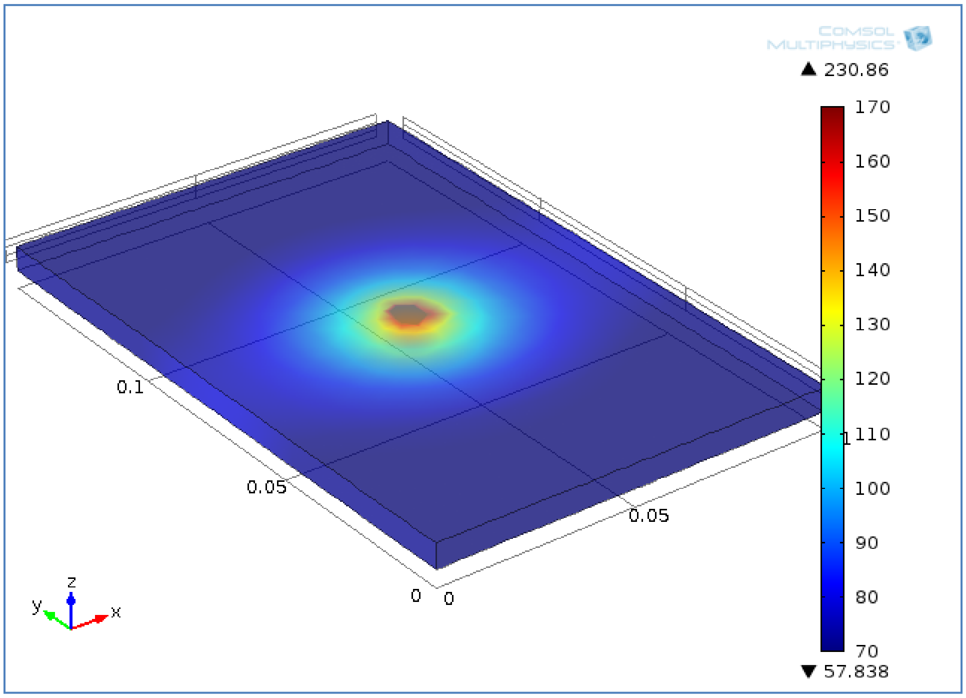

Figure 5.22. FEA representation of static heating from an atmospheric plasma torch

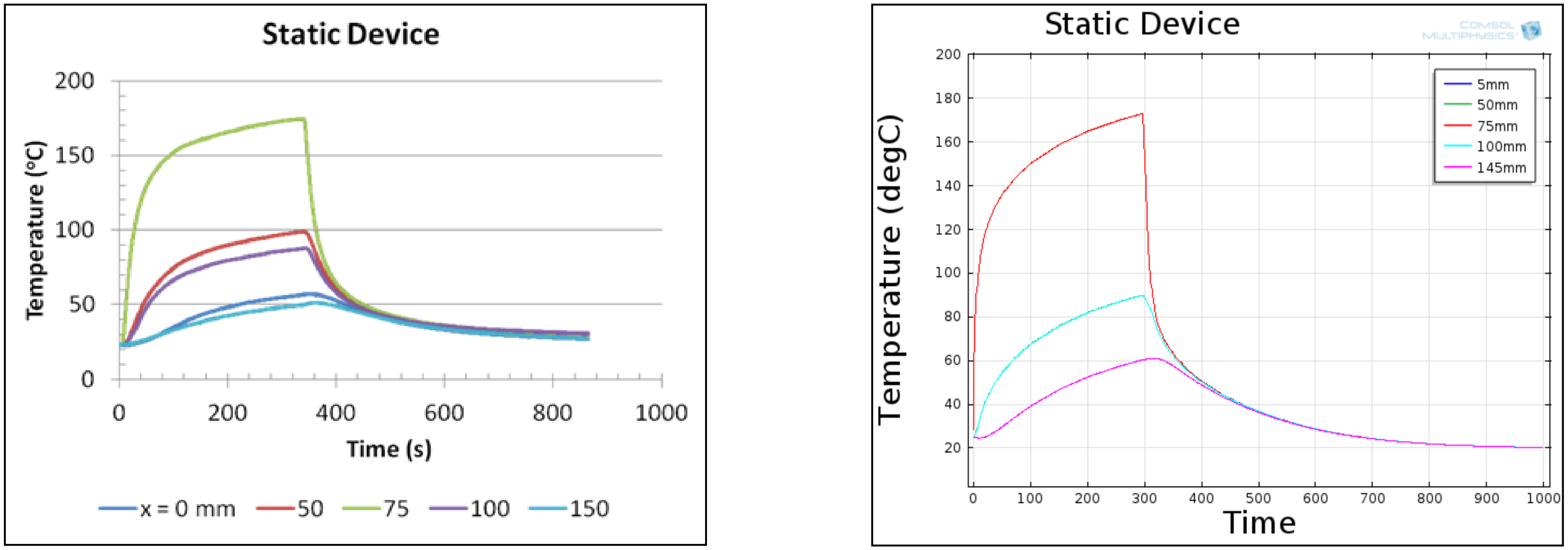

Figure 5.23. Experimental result from plasma static heating (left); FEA simulated thermal profile during plasma static heating (right)

Even though the maximum measured temperature at the back of the plate was close to ~180 °C, the simulated temperature at the top reached values of 230°C; this is caused by temperature gradients due to the shallow heat source produced by the atmospheric plasma torch, for which only surface heating is desired. A graphical representation of the static plate heating can be seen in Figure 5.22 and Figure 5.23 shows the data that later supports the reliability of the model used to represent the experimental setup. The differences observed between the experimental setup and the simulated data, especially with the temperature profile at 0, 50, 100 an 150mm where the curves are close but not overlapped as seen on the simulated data. This can be a result of non-symmetry between the thermocouples compared to the heat source location at 75mm, causing small differences on the measured temperature, contrary to the simulation setup.

Simulated data corresponding to the dynamic heating test is seen in Figure 5.24, where a time-dependent square function was used to represent the atmospheric plasma torch scan movements. A 3D solid heat distribution also observed, as a product of coupling the domains representing the steel plate and the planar heat source. The accuracy of this model can be observed in Figure 5.25, when the experimental temperature profile is compared with the simulated results; another indication of this arrangement being a proper set of conditions to model a moving heat source.

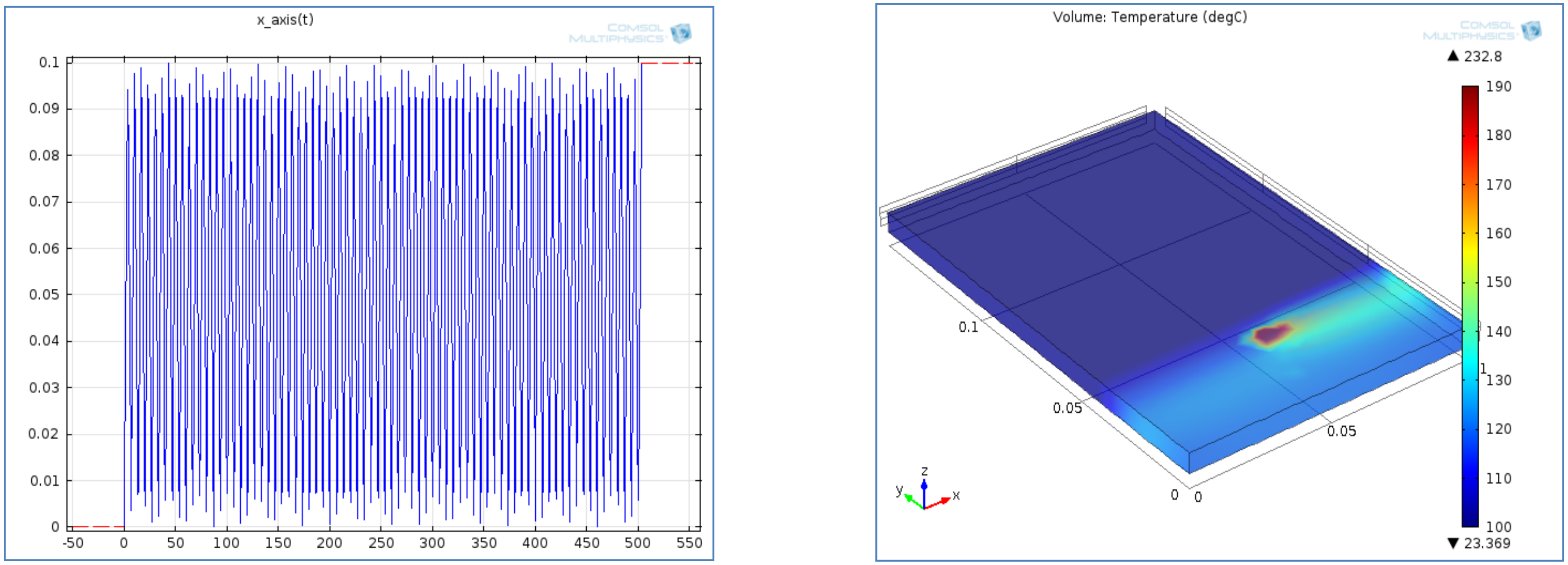

Figure 5.24. Modeled scan path (left), Moving heat source modeled by Comsol multiphysics (right)

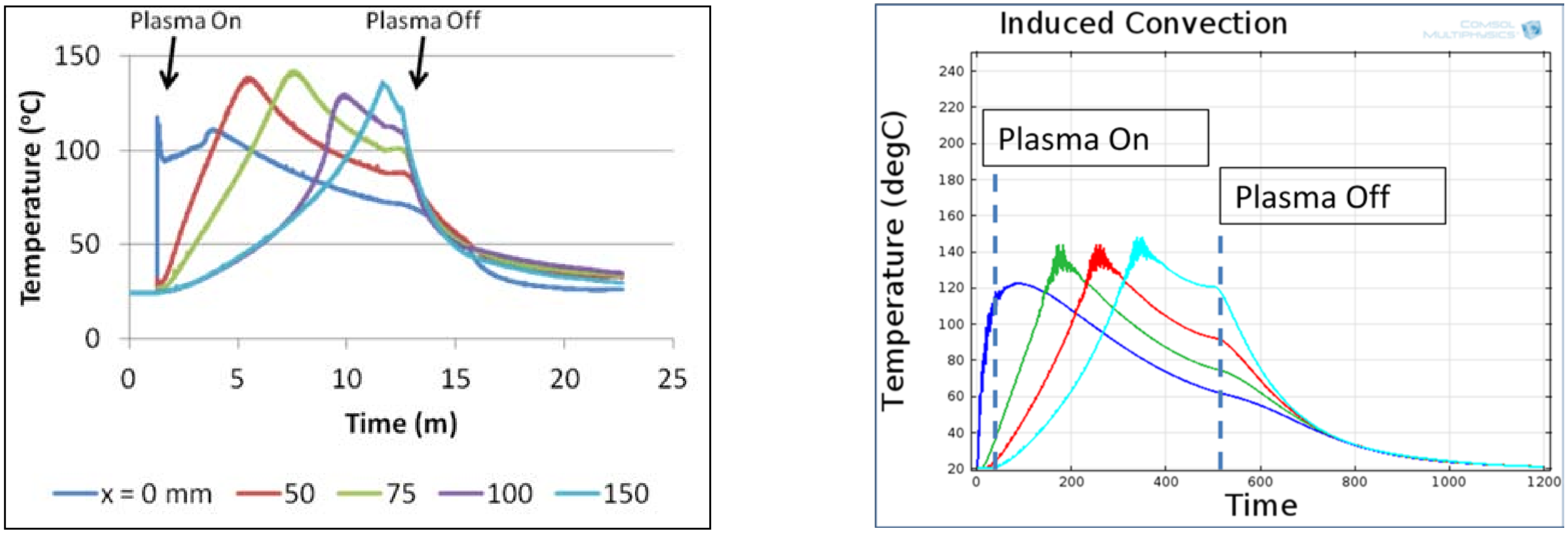

Figure 5.25. Temperature measurements comparison between natural and induced convection during plasma heating

Model Validation

The model previously described is not only applicable to an electron beam melting process, but to any moving heat source system as long as the heat source and the boundary conditions are defined correctly.

5.10. Summary

The methodology to enable the modeling and simulation of Ti6Al4V PREP powder material through the EBSM process is discussed in this chapter, starting from strategies to model a moving heat source to solving individual domains representing each additive deposited layer, and followed by the use of the partial numerical solution as an initial condition for the new layer to be deposited. A multi-axis step approach is later used to solve the heat transfer equation, using temperature dependant properties for heat capacity *Cp(T)* and thermal conductivity *k(T).* Apart from conduction heat losses, heat losses by radiation are also accounted for, using temperature-dependent emissivity *ε(T)* values previously obtained from solid and powder material surfaces. Reliable results were obtained for the three process steps consisting of pre-heating, melting, and final cooling. Finally, two validation methods were presented; the first was a direct strategy using the in-situ process monitoring temperature data during the EBSM material built, and the second consisted of using an atmospheric plasma torch in static and dynamic state where the proposed model is proven to be a good representation of the heat transfer phenomena.

6. EBSM Post-Processing Characterization of Ti6Al4V Alloys Produced by EBSM

Since the creation of additive manufacturing technology, there have been continuous improvements to meet ever-changing customer quality demands. Several examples can be seen in the form of the file formats and algorithms used to segment the CAD data to ensure high quality finished parts, from conceptual design to the manufacturing stage. New methods to improve equipment performance have been developed, mainly oriented to achieve tighter tolerances and enable complex geometries for a demanding market. However, this technology as any other novel manufacturing process, do not yet possess available standards for the powder physical characteristics like fraction size distribution and internal particle porosity percentage allowed, to be used on additive manufacturing.

Nevertheless, some standards could be used as a reference for powder quality such as ASTM F1580-12 designed for surgical applications including powder fractions manufactured by PREP, GA and hydride-dehydride processes. This standard specifies values for chemical composition, oxygen content and powder particle size, the latter still according to customer requirements. In case of the EBSM as-built condition, the standard for solid wrought annealed material contained on ASTM F1472 was used as a quality reference specifying chemical composition, microstructure and mechanical properties. Additionally non-destructive inspection by radiographic analysis was described in ASTM F29-11. Later, the creation of standards for the additive manufactured Ti6Al4V materials took place, with SAE AMS 4999a, containing not only a section dedicated to minimum tensile property requirements, but also mechanical property characteristics for process parameters and supplier qualification, enabling the use of multiple additive processes and powder feedstock [157].

The increasing number of new applications using additive technology has caused the development of new standards like the ones initiated by ASTM in 2009 by a technical committee dedicated to additive manufacturing technologies named ***F42,*** developing standards such as F-2792, F-2915 and F-2921, discussing and normalizing basic areas such as standard terminology, file formats, and coordinate systems. Still factors such as surface quality and permissible porosity remains to be specified by customer design conditions.

6.1. The effect of surface roughness and porosity

Special interest was dedicated to the non-destructive inspection of parts manufactured by the EBSM process, mainly due to the high cost linked with conventional inspection techniques for porosity and microstructure analysis like partial sectioning. The first property studied was surface roughness, since it is thought to be a cause for crack initiation and propagation under fatigue conditions [10]; as well as fatigue initiation life, final separation life, and fatigue endurance limit [158].

On the other hand, part porosity is a phenomenon mainly created by non-melted regions due to improper powder raking, e-beam scan conditions, and trapped argon gas within the particle stemming from its manufacturing method (see section 3.2), having an adverse effect on the built part's reliability [159]. As a result, two non-destructive methods were used for roughness and part porosity evaluation in a Ti6Al4V sample using PREP powder material (see procedure in section 2.4). 3D profilometry, a non-contact surface measurement technique was reviewed along with the use of computed tomography for porosity inspection.

6.2. EBSM Surface Finish Analysis

Currently, EBSM processes surface finish values are in the range of 25-35 rms, making of this technology a good alternative for structural parts as well as biomaterials applications due to early tissue response[160]. Although, in some cases lower roughness values are required to meet dimensional accuracies which may require secondary operations, depending on their intended use [161]. Attempts to improve the surface quality of additive manufactured parts started by using EBSM multi-beam strategies [162], continued with the analysis of the powder fraction's influence on surface roughness in the "as-built" condition [163], and moved on to post-processing methods like micro machined process (MMP) [164] and electrochemical machining (ECM) [165], for achievement of accurate selective surface finishes. Previous research on powder properties like particle size distribution, apparent density, and powder bed density suggests these properties heavily influence the final surface roughness of the material [107, 166]; specifically, processing of powders with coarser particles results in rougher surfaces, even after subsequent post-processing operations[105] takes place.

6.2.1. 3D Profilometry

3D profilometry was conducted on an (EBSM)-built part made from Ti6Al4V alloy PREP powder (previously described in section 2.4). Two different surface qualities are present when an EBSM part is produced. The first one corresponds to the melt pool area. This area refers to the line-of-sight where the electron beam impinges the powder layer by layer, characterized by smooth features due to high wetting values for the Ti6Al4V on the surface at melting temperatures. The cooling process in this area is governed by radiation losses into the vacuum system, axial conduction towards the built plate, and to a lower degree on conduction in a radial direction through the surrounding powder. On the other side of the build, perpendicular to the electron beam trajectory, a rough surface emerges as a result of the part outline melting area in contact with un-melted or surrounding powder. This area presents low cooling rates in the powder direction and its final finishing depends on factors such as powder particle size distribution selection, used powder recycling strategy and finally EBSM user-defined process conditions like electron beam scanning strategy and speed function among others.

Profilometry measurements were performed and roughness maps for the melt front as well as the powder contact area can be seen in Figure 6.1 and Figure 6.3. Different values are observed on the measured data between the roughness found inside of the melt front 67.882µm and the values on the contour of the part 181.76 µm, these differences emerging from the way each surface type is created.

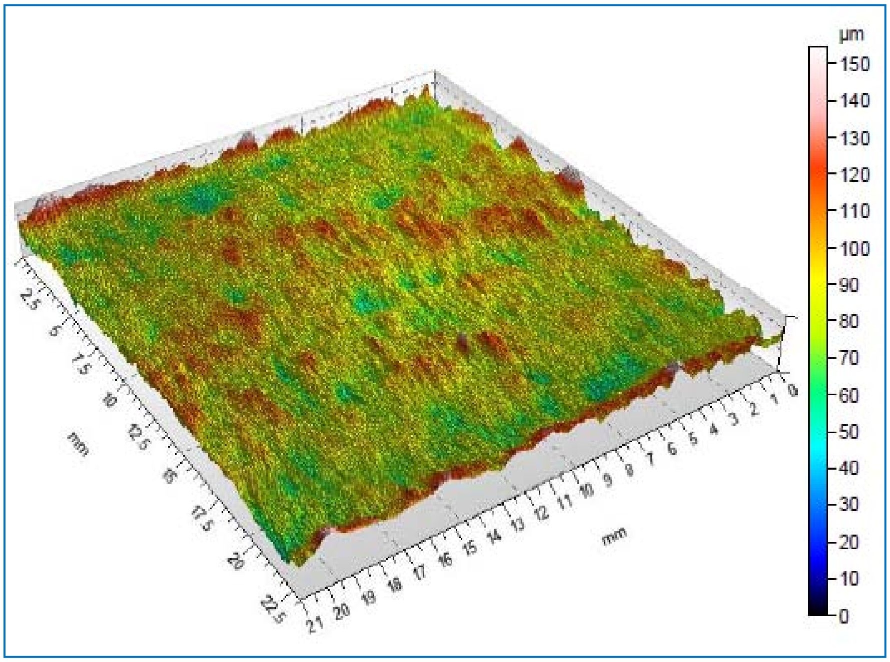

Figure 6.1 EBSM Melt front surface area 3D roughness map

During the EBSM process a part contour is demarked over the already pre-sintered powder followed by the melting of the fill area previously outlined as described in Figure 6.2. surface energy and fluid flow conditions as the metal wets the substrate surface followed by its solidification.

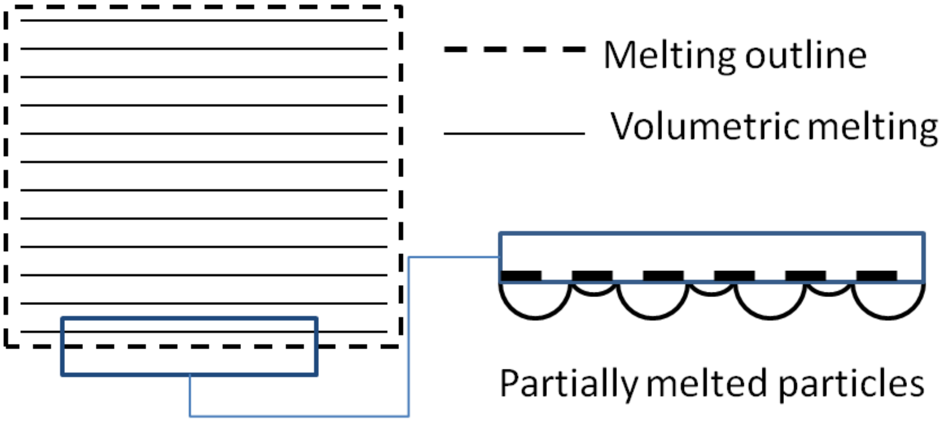

Figure 6.2 Individual layer melting sequence (top view)

Low roughness values found on the melt front or fill area, are attributed to molten metal On the other hand, the roughness found on the powder contact area is originated by the part contour stage, given that the contour melting only comprises a small powder volume, thus the resulting roughness is dictated by the specific powder fraction, the electron beam and user process conditions.

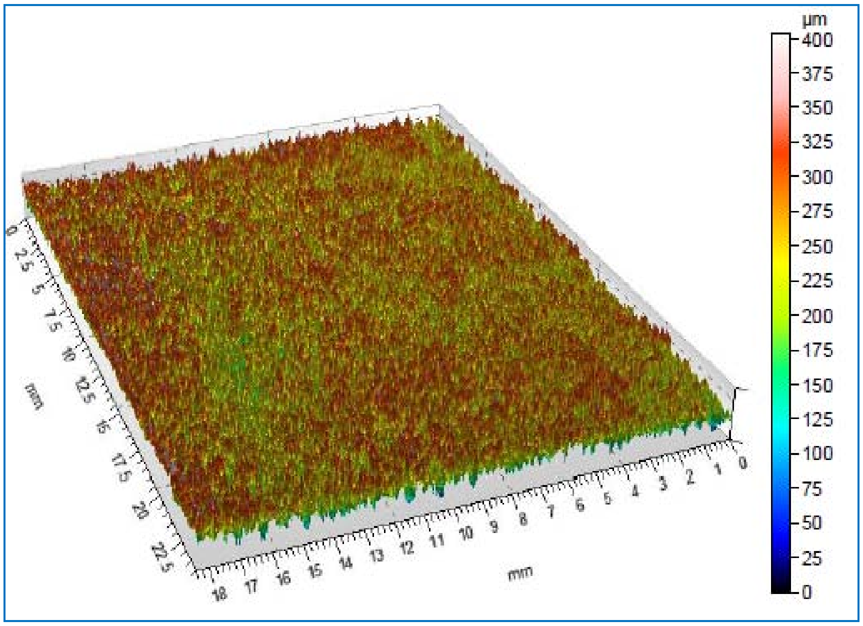

Figure 6.3 EBSM Surface roughness in contact with sintered powder material

Table 6.1. Summary Table 3D surface roughness on PREP solid parts

Measurement	**Melt Front Surface**	**Surface in contact with powder**
Root Mean Square Height (Sq)	12.791 um	54.417 um
Skewness (Ssk)	0.431	0.026
Kurtosis (Sku)	4.398	2.557
Maximum Peak Height (Sp)	67.882 um	181.76 um
Maximum Pit Height (Sv)	86.689 um	222.315 um
Maximum Height (Sz)	154.571 um	404.076 um
Arithmetical Mean Height (Sa)	9.913 um	44.497 um

Table 6.1, shows a comparison chart between the two surfaces, where value differences of up to four times the root mean square heights for the melt front, 12.791 μm, and the powder contact area, 54.417 μm, can be observed.

A comparison between conventional surface finishing obtained by casting processes and EBSM can be observed on Figure 6.2.

Table 6.2. Surface finishing comparison between EBSM process and conventional casting process [167-169]

Surface Finishing Process	Surface Area	Roughness (RMS)
EBSM Ti6Al4V PREP Powder	*Line-of-sight surface*	12.8
	Surface in contact with powder	54.4
Cast Process	*Sand Process*	40 - 125
	Metal Mold	20 - 180
	Ceramic Mold	25 - 32
Post-Processing	*Electron Beam Machining EBM*	4
	Micro Machining Process - MMP	1 - 0.01

6.3. EBSM Porosity Defect Analysis

Post-processing is usually required when a part is produced by EBSM process, mainly to reduce or porosity within the part as a product of particle packing, part shrinkage caused by differences between stainless steel and Ti6Al4V, and argon gas trapped during the powder manufacturing process[170]. To this end, processes like hot isostatic pressing (HIP) are used, which, through the application of high temperatures and high pressures in a closed vessel, create plastic flow of the material, promoting atomic diffusion that closes the pores without any effect on the microstructure [171]. Even though the use of processes like (HIP) increases the reliability for additive parts, its effect on porosity reduction was not subject of evaluation here; only the feasibility of using techniques such as serial block face scanning electron microscopy and computer tomography for pore detection was the focus of study.

6.3.1. Serial block-face scanning electron microscopy SBFSEM

A conventional method for material defect analysis to identify microstructure evolution and flaws like lack of fusion and porosity is partial sectioning. However only two dimensional information is obtained with this method and the time required for a complete analysis increases as the sample increases in size. A novel method for partial sectioning and additional 3D rendering, is now possible by the use of serial block – phase scanning electron microscopy, enabling high image resolution and the possibility to evaluate the flaw distribution within the material in an automated manner.

Operation Principle

Initially created in 2004 by Winfried Denk at the Max-Planck-Institute in Heidelberg, serial block-face scanning electron microscopy (SBFSEM) is a hybrid system consisting of a microtome and a scanning electron microscope (see Figure 6.4). In this fashion, high surface image accuracy can be attained (~2-5 nm) by using a scanning electron microscope (SEM) with a backscattered electron detector (BSED). The partial sectioning of the sample is obtained by an ultra-microtome system, were thin slices are removed from the material (30-200nm) through the use of a diamond cutter. Finally, embedding the sample on a thermoset material allows better alignment and avoids the image compression distortion, common in 3D image reconstruction, making possible the analysis of complex biological and inorganic systems with minimum losses of sample alignment [172].

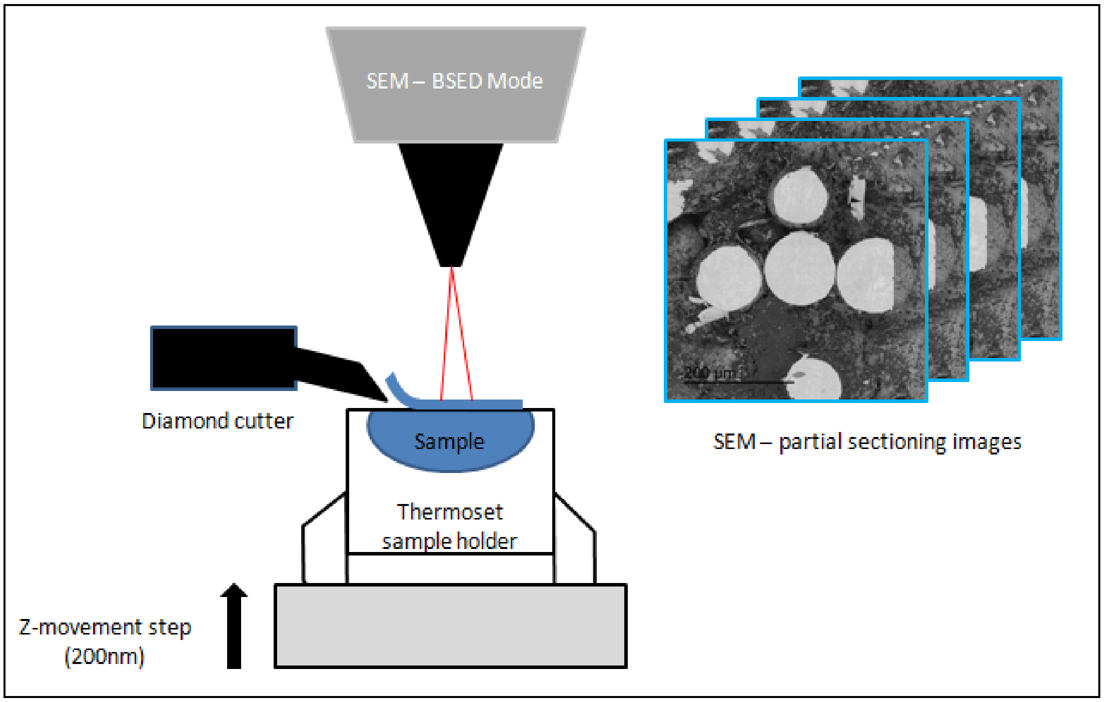

Figure 6.4. SBFSEM System setup

SBFSEM technology represents an advantage for samples requiring a higher ***z*** height and field of view control. Contrary to conventional methods for 3D material analysis like focused ion beam (FIB) and transmission electron microscopy, and even tomography, SBFSEM technology can create images of samples with a lesser height restriction, enabling the analysis of a wider area (limitation for FIB), multiple layers of material can be inspected in very short time (contrary to TEM), and the material thickness is not an issue for the partial sectioning process (different from tomography). And whereas image reconstruction is time-consuming and cumbersome in most of these techniques, SBFSEM is neither.

Sample preparation

A solid sample of PREP powder was extracted from the rough area in contact with the powder, as described in Figure 6.4, with dimensions (10 mm x 3 mm x 3 mm), and later re-dimensioned to fit the SBFSEM system. The sample was embedded in an acrylic base material for support, mounted on a removable specimen holder of 10 mm diameter, and placed on the ultra-microtome specimen stage. Considering the field of view of the system, a surface of $0.25mm^2$ was prepared by pre-cutting with a diamond knife, since the travel range for the vertical motor is only 700 μm, limiting travel to only 500 μm of material thickness. The working distance for the SEM was about 11 mm, and a piezo-actuated diamond knife from Diatome was used at an angle of 45°, with a clearance angle of 11°and a cutting edge length of 1.5 mm [173].

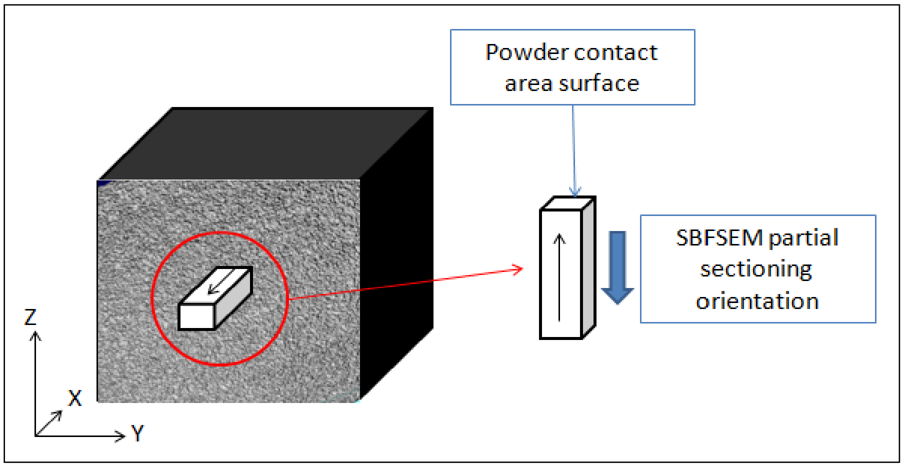

Figure 6.5. PREP - Ti6Al4V sample extraction for SBFSEM analysis

Partial sectioning was performed by removing 200 nm of solid material, and 1000 material slices were sectioned, imaged, and later used for volume rendering. Figure 6.6 shows a partial section of the powder contact area, where the porosity is shown in the partially melted particles comprising the Ti6Al4V EBSM surface.

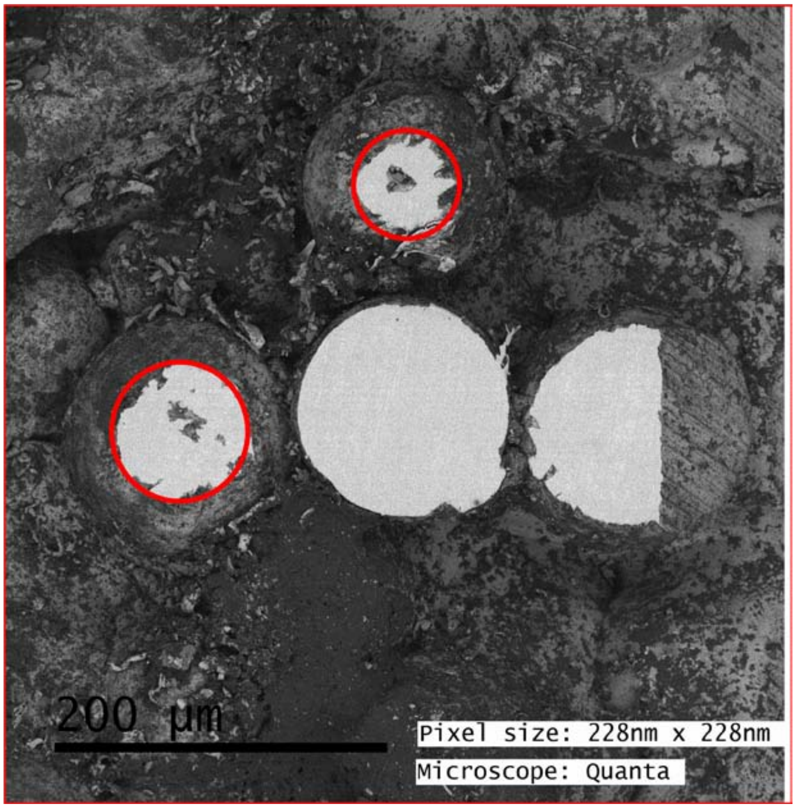

Figure 6.6. Inner particle porosity SEM image (seen in red) at the surface of a Ti6Al4V built

An image rendering was performed using 3D view software from Gatan Inc. Some partial particle sectioning can be observed as truncated shapes as a product of the sample preparation and the different layers constituting the partial sectioning reconstruction (Figure 6.7). This analysis enables an understanding of how the roughness of the EBSM processed surfaces is dictated by the particle size and the resulting surface porosity is the product of particle packing coupled with inner particle porosity.

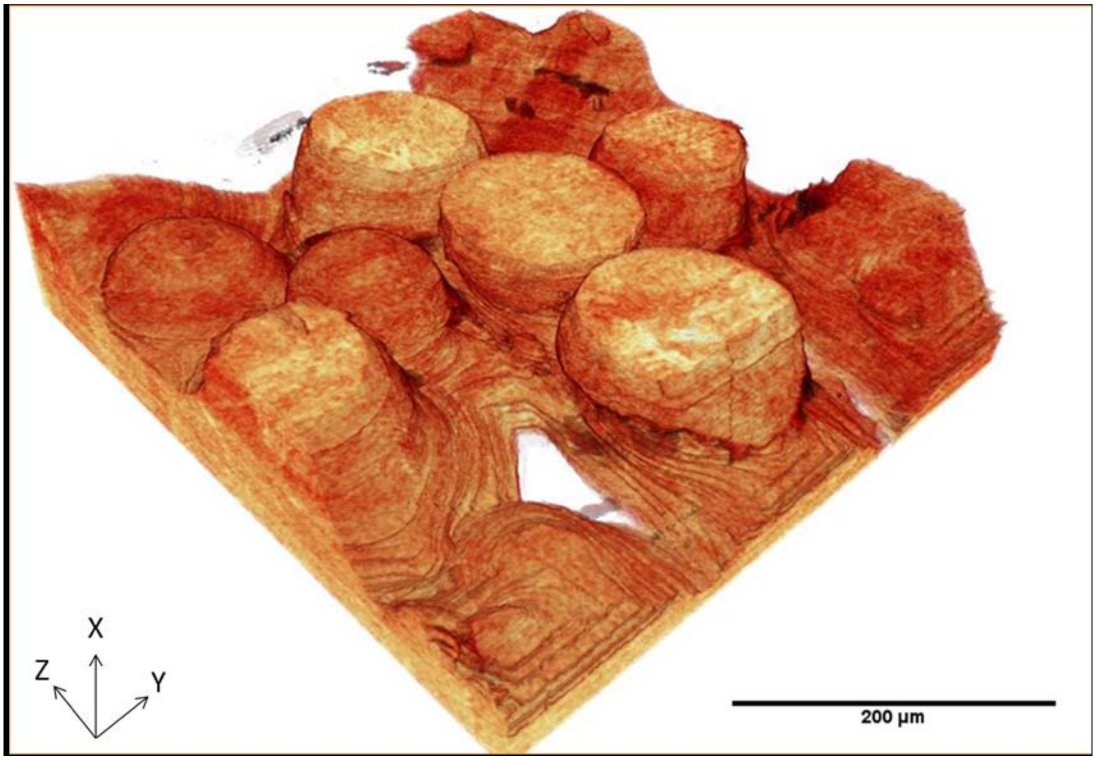

Figure 6.7 3D Image reconstruction from SBFSEM system of a EBSM Surface

Even though the EBFSEM system offers a versatile way to determine material flaws at very high imaging resolution, its destructive nature and limited analytic volume make it of narrow use as an EBSM process quality method. As a consequence the use of complementary practices is required for inspection of larger parts, equipped with high resolution and a non-destructive nature, for which computed tomography represent an excellent candidate.

6.3.2. Computer Tomography (Micro - CT Scan)

Through many years computed tomography has been used as a tool for measuring and assuring standard compliance for dimensional tolerance as a replacement to conventional methods such as coordinate measuring machine (CMM). Along with the development of rapid prototyping and manufacturing techniques, the necessity of a convenient, flexible and accurate way to measure complex shapes (i.e. inner cavities) arose, limiting conventional measuring methods, mainly for the inability to reach small areas out-of-sight. Therefore computed tomography was tested and implemented for industrial purposes. Initially used on the medical (i.e. cranial, maxillofacial procedures and auricular prosthesis among others) [174, 175] and veterinarian field for modeling and manufacture of custom made implants [176]; the transfer of this technology to industrial applications required the development of new software tools to process larger amount of data, including the development of new algorithms for surface reconstruction in a faster and efficient way [177]. That required an inspection equipment modification with higher X-ray power sources (i.e. 160-450 keV) due to its application on denser materials [178].

Data available on computed tomography used as a non-destructive inspection on rapid prototyping parts were initially reported on selective laser sintering of polymers by *Jande* [179] in metals, using laser engineered net shaping process - LENS by *Wang et al.* [180] and laser direct metal deposition by *Ahsan et al.* [99] as well as EBSM processes by *Parthasarathy et al.* [35].

Volumetric porosity analysis

The main goal for this analysis was to identify the existence of porosity and its distribution in the built part. Additionally, it was sought to determine if the porosity is likely to be localized in any specific area in the build, information that can be later used for process improvement. With this purpose, computer tomography analysis was performed using two different systems: A Versa XRM-500 from X-Radia, and a NSI X-View model X-50 from North Star Imaging. The first system was used to identify powder necking in PREP and GA powder as seen in section Table 2.5, and later used for inspection of a cubic sample prepared using PREP powder material using a 30 μm *voxel* size. Unfortunately the resolution obtained by the setup described in Table 2.6 was not high enough to resolve porosity at values less than ~60 μm (see Figure 6.8), although a surface rendering was possible, as seen in Figure6.9 .

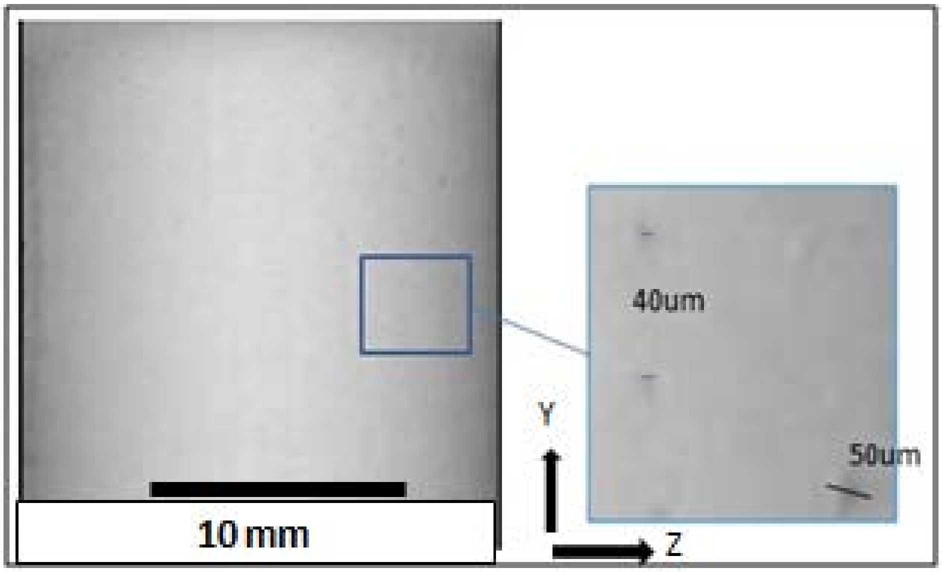

Figure 6.8 CT Scan cross section for PREP TI6Al4V sample using MicroXCT-200

This 3D solid surface information was saved as a ***.stl*** file which can be later be used as an additive file or to improve the modeling of more realistic parts by considering factors such as surface roughness, which are otherwise difficult to simulate.

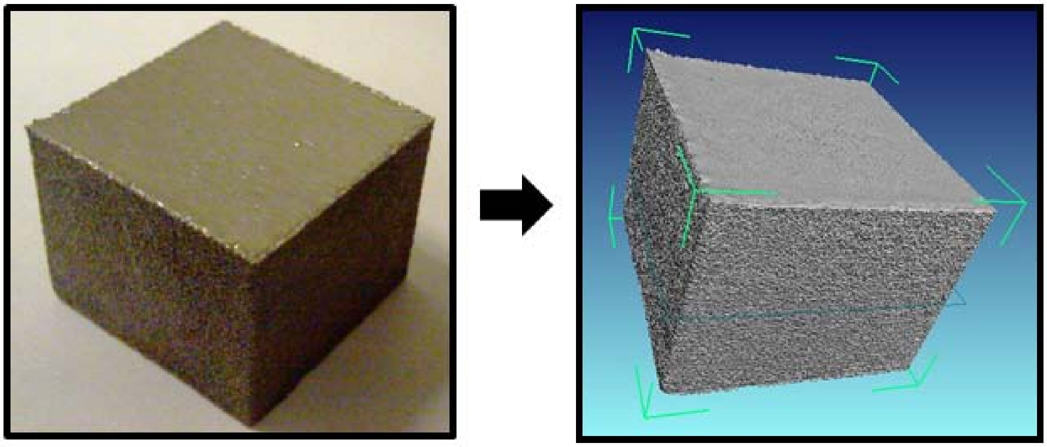

Figure6.9. As-built EBSM digital image (left); computed tomography image reconstruction (right)

Even though the system used for this analysis is capable of better resolution, it is understood that computed tomography is very sensitive to the material density and attenuation coefficient, requiring a testing protocol when a new material is being inspected. Thus several tests must be conducted to improve the resolution of the results. For that, a second system was used where two A and B scanning setups were tested, as seen in Table 2.7. The first scan setup, (A), showed an appreciable improvement in resolution; enough to identify porosity sizes down to ~80 microns (shown by the white dots marked on the figure) and lower as seen in Figure 6.10.

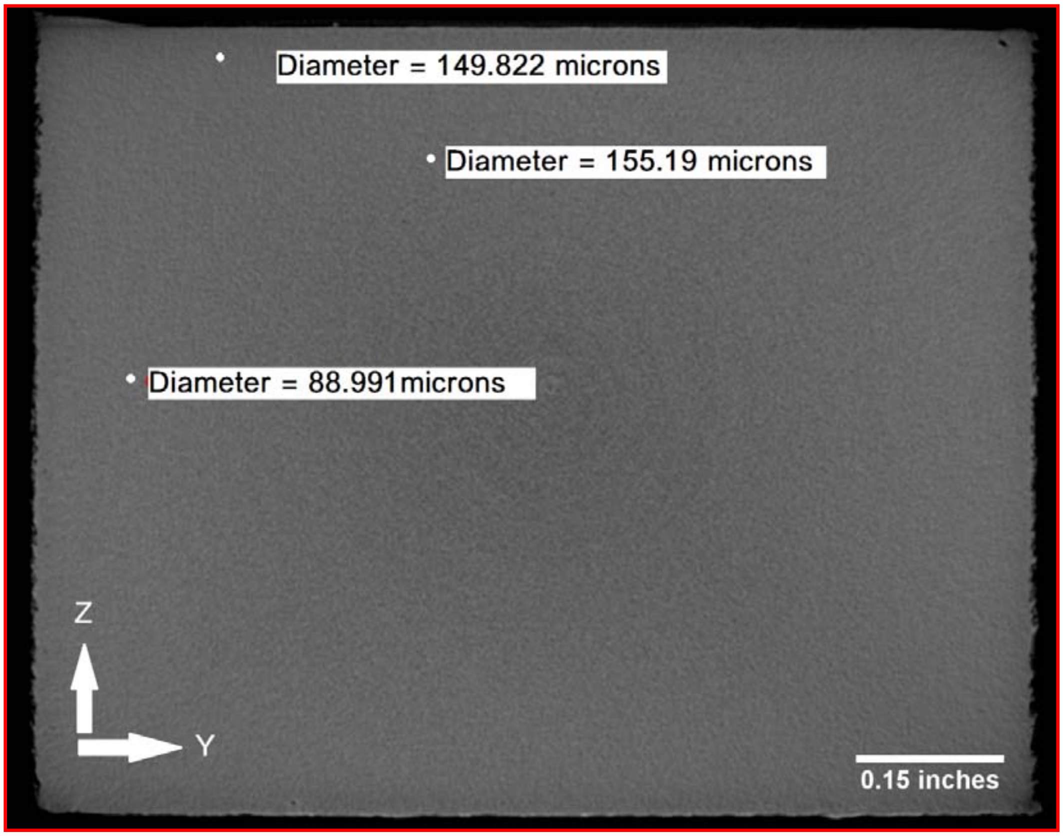

Figure 6.10. X-Y CT cross section for Ti6Al4V sample using Scan type A.

Once a set of data was obtained, a segmentation process was performed, where the digital point cloud information, called *voxel,* determines the scan resolution and stores that information in an array of grey values were a threshold is set to separate the part from the environment. The threshold process continues, this time to separate the porosity values from the rest of the part. For this process to be accurate there must be enough contrast between the pore and the circumventing grey scale values, otherwise the threshold filtering will illustrate either larger pore sizes or no pores due to not enough pixels within the pore.

After processing the scan data, it was observed that the contrast was not high enough to enable the pore filtering desired. The detector on the micro CT scanner from Varian, with a pixel resolution of [1536 x 1920], was replaced by a Pelkin Elmer detector with a better pixel resolution of [2048 x 2048], thus decreasing the *voxel* size from 25 to 20.4 μm, and a new scan (B) was performed.

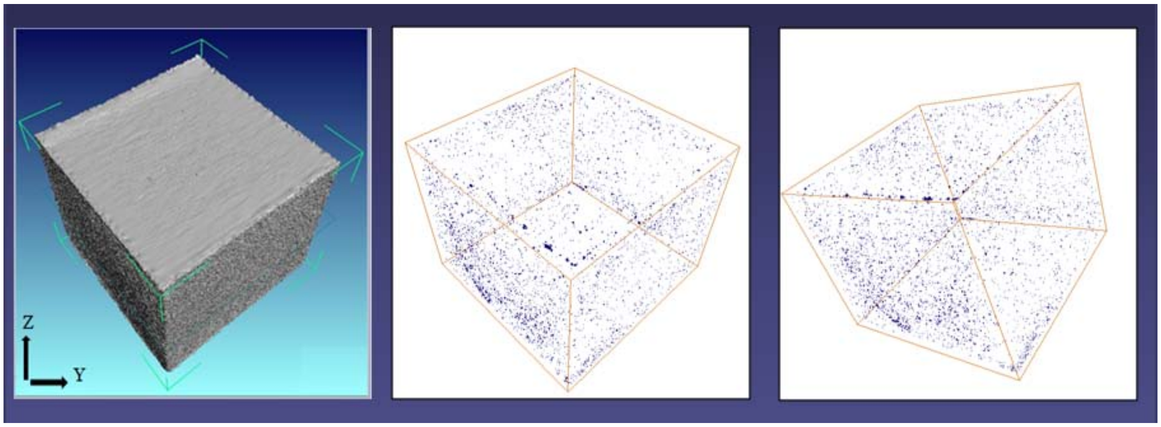

Figure 6.11. Threshold data filtering illustration. Volume rendering (left), sample porosity distribution side view (middle and right).

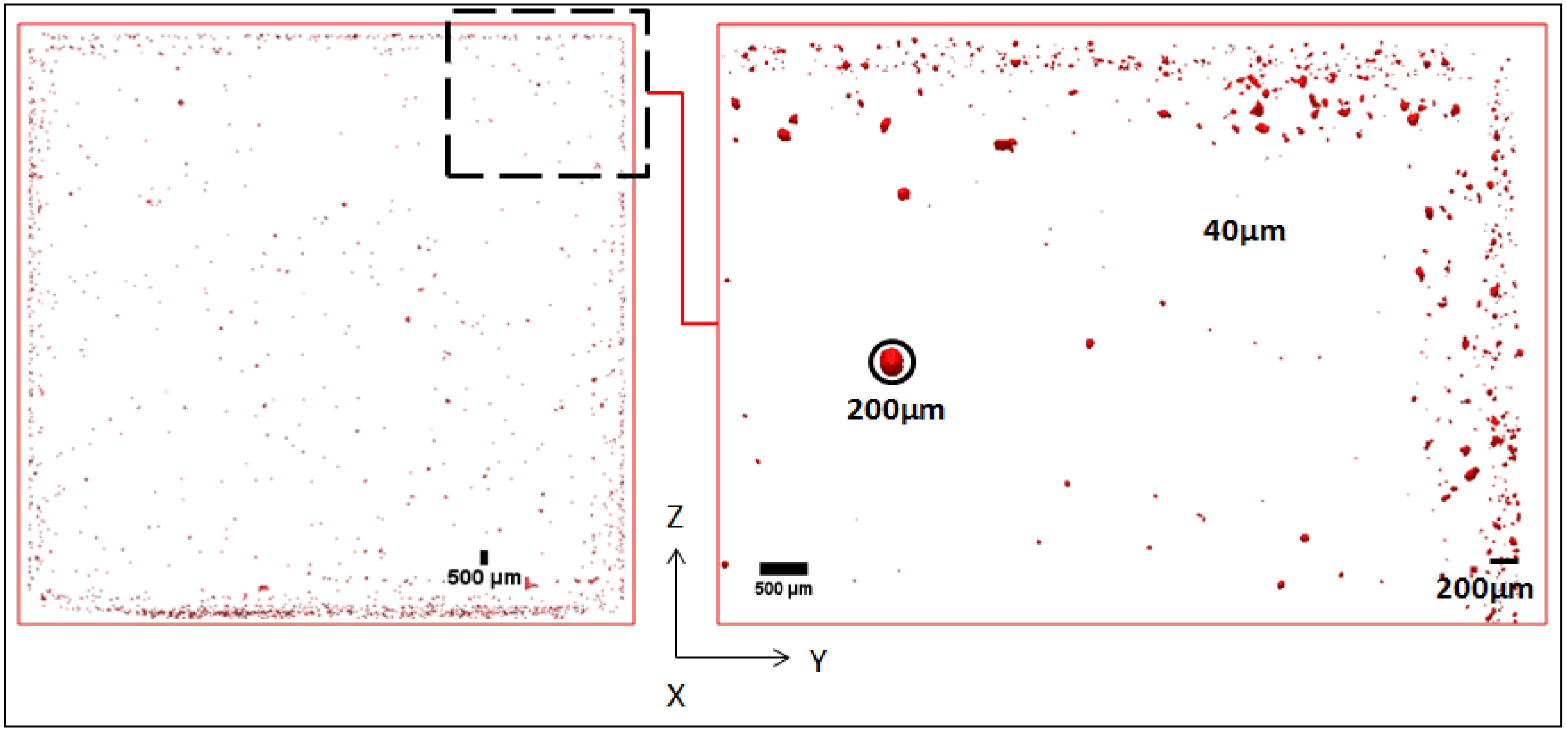

Figure 6.12. Side view of a computed tomography porosity volume rendering of a Ti6Al4V EBSM processed part using PREP powder material as a feedstock (left). Zoomed image of porosity concentration towards the EBSM part surface (right).

Porosity values were obtained using a threshold filtering range from 200 μm to 40 μm in resolution, and the inner porosity observed is thought to be a combined result of un-melted areas and gas trapped in the powder material. Finally, it is important to clarify that no HIP (Hot Isostatic Pressing) process was used to decrease the resulting porosity [181], and the data here observed was in effect the resulting EBSM process porosity.

As seen in Figure 6.12 (left side), a larger amount of porosity is observed in the lower surface area of the EBSM part (which is in contact with the stainless steel build plate), probably caused by poor wetting from the melted Ti6Al4V pool onto the stainless steel (SS) plate. This resulting porosity is also increased by differences in the thermal expansion coefficients of the two materials. It is also observed a porosity accumulation in areas immediately in contact with the sintered powder mainly caused by the interface between the powder material and the melted part during the part contour melting operation taking place at each layer deposition. Finally, the top right sample surface had been increased in size for better pore resolution (Figure 6.12 on the right side), where porosity concentration can be again observed towards the part surface. Related to the pore distribution within the part volume, a uniform distribution was observed indicating no preferential formation caused due to any process condition as previously seen in Figure 6.11.

6.4. Summary

The importance and effect of surface finishing and part porosity, as well as alternative methods for EBSM part characterization, were presented in this chapter. Surface roughness and build porosity, resulting from a specific powder particle distribution and a powder material process like plasma rotated electrode PREP, was studied and analyzed. Surface profilometry was presented as a convenient way to obtain roughness measurements and for future surface finishing comparisons, having as a main advantage its non-contact attribute, allowing the analysis of larger areas in lower times. Furthermore, a serial block-face scanning electron microscopy technique was reviewed and the advantages of this technique for surface and defect analysis were shown. However, its minimal volumetric analysis capability limits the use of this technology as a part of a quality control set for EBSM parts. As a result, micro computed tomography is proposed and discussed, showing its capabilities for surface roughness analysis, part measurement, and defect analysis at resolutions close to 40 microns in size.

7. CONCLUSIONS

The heat evolution (heating, melting and cooling cycles) during a multi layer process is considered to be a key factor controlling the resulting microstructure ultimately responsible for the final properties of the built part. Therefore, thermal modeling and simulation by finite element analysis of the electron beam selective process of Ti6Al4V alloys was used here as an strategy to minimize the turnaround time by partially reducing the trial an error testing currently performed during the additive manufacturing process when a new material and part application is developed.

However, accurate, reliable and reproducible thermal predictive models require the use of temperature dependant properties, in this case in powder and solid state to properly solve the fundamental equations representing this physical phenomenon. Consequently, the effect of temperature on the physical and thermal properties of Ti6Al4V powder alloys used in electron beam selective melting processes was presented here, comparing two commercially-available gas atomized powders, PREP and GA. Initial morphology results on powder material, showed spherical powder particles for both PREP and GA, typical from powder the atomization process. The presence of inner-particle porosity in PREP and GA powder was also observed through tomography analysis of *pressureless* sintered powder fractions, although no observed correlation between the particle and pore size was found. Particle size distribution by laser diffraction in wet and dry dispersion mode, showed how susceptible results are to the sample size (powder amount) used. Initially, comparative values for PREP and GA size distribution were found, when wet particle dispersion and 5 grams of sample was used. On the contrary when the powder dispersion method was changed to a dry procedure using 250 grams of sample an increase of 47% in particle size for PREP powder compared to GA was observed, for what a higher sample size (> 5grms) is advised.

True density values from loose to partially sintered powder showed no major changes; although higher powder porosity values were observed on PREP powder than in the GA based on bulk density data and the relative porosity reduction after the powder was partially sintered was higher in the GA powder material. Surface area methods were used to evaluate PREP and GA powders in both loose and partially sintered form, in order to calculate the area reduction caused by the sintering process and later correlate it with emissivity values. Small variability was observed in the data obtained by gas and liquid pycnometry, with the only observation being the deleterious effect of high intrusion pressures used by the mercury pycnometry technique when measuring partial sintered material, which caused de-bonding in the powder particles resulting on slightly higher surface area values.

Small particle contact area was observed in both of the partially-sintered powders during the tomography analysis, a result that explains the low recorded thermal diffusivity and thermal conductivity values. Heat capacity evaluation using high temperature DSC analysis showed no differences between (as-received) PREP and GA powders; in contrast, this data group differs from that of powder recycled from both methods at temperatures higher than the beta *transus*, mainly due to differences in thermal history. When compared with as-built EBSM solid samples using PREP and GA powder feedstock, the effect is even more pronounced, especially when an exothermic reaction takes place right after the beta *transus* is attained. Data indicated this exothermic phenomenon should be attributed to a crystallization process from isotropic columnar into *equiaxed* grains. Due to this occurrence, heat capacity evaluation in the range between beta *transus* and melting point was evaluated using laser flash calorimetry. No exothermic reaction was observed using this technique due to the high heating and cooling rates reached by the system and the data obtained was in agreement with previously published data. Small differences in thermal diffusivity and conductivity values were also observed on (as-built) PREP and GA materials and differences in thermal diffusivity and thermal conductivity between powder material and as-built samples of up to three times were observed, with the powder only representing approximately 14% of the total conductivity measured on the solid build. It can be concluded that although higher particle distribution and surface area are observed in PREP powders, no determinant effect is observed in thermal properties between PREP and GA powders. Since no effective differences are seen in the thermal properties between PREP and GA materials, an additional study was conducted on the effect of solid sample orientation on diffusivity and thermal conductivity of Ti6Al4V samples prepared using PREP powder. Higher values were observed in samples parallel to the built direction than in samples evaluated orthogonal to the build direction, later explained as a result of the scattering effect of the grain boundaries compared with lattice vibrations due to a lack of symmetry of a large grain boundary created as the product of anisotropic heat flux during the build creating a columnar growth and preferential heat conduction in the parallel direction of the build.

Temperature dependence on directional emissivity values for analysis on radiative heat losses were evaluated including the effect of particle size distribution and surface roughness on PREP and GA Ti6Al4V loose and pressureless sintered powder as well as in solid state. High surface roughness values, presented an increase in emissivity and a variable emission phenomena was observed during loose powder heating, where the effect of directional emissivity and spectral temperature range was observed by an initial decrease in emissivity followed by a sudden stabilization at 550 °C, and a sudden increase at temperatures close to 750 °C, thought to be caused by the powder sintering process.

Although single step modeling proved an impractical method for emulating moving heat sources in 3D due to excessive required computing resources and simulation time, it did show the feasibility for solving multiple time and temperature-dependent domains, when coupled with the use of *Matlab* sub-routines for automatization purposes. Multi-axis modeling based on the solution of individual domains using a function for activating and de-activating consecutive material layers during the process, proved to be an effective approach to numerically solve the thermal distribution during the additive manufacturing process including non-uniform geometries. The multi-axis model was validated using in-situ temperature data with reliable results. Alternative heat sources such as atmospheric plasmas was used as a validation strategy, further supporting the flexibility and robustness of this model as a representation of any heat source moving in three dimensions. Advantages of the thermal model are presented to be a reliable method to evaluate temperature gradients causing residual stresses as well as the use of these results for further analysis on microstructure models for phase evolution and preferential orientation studies. Limitations on the model were also presented such as the inability to predict surface roughness or built porosity values and location since the powder material is represented by a continuous conductive layer for which the shape of the powder is not accounted for in order to decrease computing resources.

Finally, a review of the current quality standards existing for materials to be used on additive manufacturing processes such as electron beam selective melting showed the requirements for Ti6Al4V powder feedstock on chemical composition and mechanical properties. Additionally, alternative methods for material analysis of parts produced by electron beam melting were discussed such as surface analysis, by non-contact 3D profilometry, offering a convenient way to estimate the surface quality of EBSM parts, where differences between the melt pool front and the powder contact area were observed. Later, the effect of initial powder size distribution on the resulting surface finish was presented, including novel post-processing methods to improve the surface finishing, such as micro machining processes. The effect of residual porosity after an EBSM part was produced is presented, including the use of computed tomography for inclusion and pore detection. This technique appears to be a convenient method for part inspection, with the only drawback presented being a limitation on the size of the inspected part due to signal attenuation factors.

Overall, a set of measurements were conducted on PREP and GA powder materials to be used as input information during modeling and simulation of the EBSM process. Initial evaluation results showed substantial differences between the two powder fractions only in particle size distribution, and its direct effect was observed in its thermal properties like heat capacity, diffusivity, and thermal conductivity. Directional thermal property dependence was found in thermal diffusivity and thermal conductivity values for as-built EBSM Ti6Al4V alloy parts when samples were prepared parallel and orthogonal to the build direction. On the modeling side, a new method was proposed to represent the EBSM process, with reliable results not only for additive manufacturing but for any other process involving a moving heat source. Lastly, the use of micro computed tomography was shown as able to resolve porosities down to 40 μm in processed parts before any hot isostatic pressing process has taken place.

8. FUTURE WORK

Based on the results presented in this research work, the list of subjects to be further evaluated is as follows:

- As previously shown, the thermal history of recycled powder materials affects their thermal properties, and additional studies must be conducted in order to improve the powder feedstock additive data based on materials such as Titanium Grade 2, CoCrMo ASTM F75, IN-718, Waspaloy, and Aluminum 6061, among others.

- Additional efforts should be also dedicated to in-situ control and temperature data acquisition during the EBSM process, enabling more accurate and reliable finite element models including flaw detection through thermal imaging [182] and chemical mapping control [183].

- For EBSM modeling, a methodology to convert entire 3D geometries into an array of individual slices to be further modeled by the multi-axis approach is required. Additionally, the creation of algorithms capable of generating adaptive electron beam melting scans similar to the ones used by the EBSM system and the use of the material temperature dependent properties, will help improve the accuracy of the current models enabling to obtain more predictive results.

- Finally, the efficiency on porosity reduction caused by hot isostatic pressing and its non-destructive inspection using micro-computed tomography is a subject of further analysis.

9. REFERENCES

1. Emsley, J., *Nature's building blocks: an A-Z guide to the elements*. 2001: Oxford University Press.

2. Froes, F., M. Gungor, and M. Ashraf Imam, *Cost-affordable titanium: The component fabrication perspective.* JOM Journal of the Minerals, Metals and Materials Society, 2007. **59**(6): p. 28-31.

3. Boyer, R., *Attributes, characteristics, and applications of titanium and its alloys.* JOM Journal of the Minerals, Metals and Materials Society, 2010. **62**(5): p. 21-24.

4. Peter W. H., B.C.A., Scorey C. R. , Ernst W., McKernan J. M., Kiggans J. O. , Rivard J.D.K. , and Yu C.,, *Non-Melt Processing of "Low-Cost", Armstrong Titanium and Titanium Allow Powders*, in *Proceedings of the Light Metals Technology Conference*. 2007.

5. EHK Technologies Inc., *Summary of Emerging Titanium Cost Reduction Technologies*. 2004, US Dept. of Energy / Oak Ridge National Laboratory.

6. Rivard J. D.K., B.C.A., Harper D. C. , Kiggans J. O., Menchhofer P.A., Mayotte J. R. , Jacobsen L. , and D. Kogut,, *The Thermomechanical Processing of Titanium and Ti-6Al-4V Thin Gage Sheet and Plate.* JOM, 2005. **Titanium Alloys**.

7. Yamamoto Y., K.J.O., Clark M. B. , Nunn S. D., Sabau A. S, Peter W. H. , *Consolidation Process in Near Net Shape Manufacturing of Armstrong CP-Ti/Ti-6Al-4V Powders*, in *Cost Affordable Titanium III*, T.P. Switzerland, Editor. 2010.

8. Salimijazi, H., T. Coyle, and J. Mostaghimi, *Vacuum plasma spraying: A new concept for manufacturing Ti-6Al-4V structures.* JOM Journal of the Minerals, Metals and Materials Society, 2006. **58**(9): p. 50-56.

9. Ashraf Imam, M. and F. Froes, *TMS 2010 symposium: Cost-Affordable Titanium III.* JOM Journal of the Minerals, Metals and Materials Society, 2010. **62**(5): p. 15-16.

10. D. Thomas, G.S., Southeastern Tool & Die – Additive Manufacturing Division, *Additive Manufacturing for the Aerospace Industry*, in *American Helicopter Society 68th Annual Forum*. 2012, American Helicopter Society International, Inc.: Fort Worth, Texas.

11. L.Leblanc, P.T., H.R.Salimijazi,T.W.Coyle, J.Mostaghimi *On Vacuum Plasma Spray Forming of Ti-6Al-4V*, in *Thermal Spray 2003: Advancing the Science and Applying the Technology*, B.R.M.a.C. Moreau, Editor. 2003, Materials Park, OH: ASM International. p. 603-609.

12. Xu, Y.B. and Z.S. Xu, *Interstitial segregation and embrittlement in Ti-6Al-4V alloy.* JOURNAL OF MATERIALS SCIENCE, 1990. **25**(9): p. 3976-3981.

13. Safdar, A., et al., *Evaluation of microstructural development in electron beam melted Ti-6Al-4V.* Materials Characterization, 2012. **65**(0): p. 8-15.

14. B.S. Bass, *Validating the Arcam EBM Process as an Alternative Fabrication Method for Titanium-6Al-4V Alloys*, in *Materials Science and Engineering* 2008, North Carolina State University: Raleigh, NC.

15. Murr, L.E., et al., *Microstructures and mechanical properties of electron beam-rapid manufactured Ti–6Al–4V biomedical prototypes compared to wrought Ti–6Al–4V.* Materials Characterization, 2009. **60**(2): p. 96-105.

16. L. Facchini, E.M., P. Robotti, A. Molinari, *Microstructure and mechanical properties of Ti-6Al-4V produced by electron beam melting of pre-alloyed powders.* Rapid Prototyping Journal, 2009. **15**(3): p. 171 - 178.

17. Al-Bermani, S., et al., *The Origin of Microstructural Diversity, Texture, and Mechanical Properties in Electron Beam Melted Ti-6Al-4V.* METALLURGICAL AND MATERIALS TRANSACTIONS A, 2010. **41**(13): p. 3422-3434.

18. Dinda, G.P., L. Song, and J. Mazumder, *Fabrication of Ti-6Al-4V Scaffolds by Direct Metal Deposition.* METALLURGICAL AND MATERIALS TRANSACTIONS A, 2008. **39**(12): p. 2914-2922.

19. Hague R.J.M., R.P.E., *Rapid Prototyping, Tooling, and Fabrication* Rapra Review Reports, ed. R.T. Ltd. 2000.

20. Davis J.R, *Heat-resistant materials*. Technology & Engineering, ed. A. International. 1997, Materials Park, OH.

21. Karapatis, N.Y.G., P. Gygax, and R. Glardon. . *Thermal behavior of parts made by direct metal laser sintering*. in *Solid Freeform Fabrication Symposium (SFFS)*. 1998. University of Texas at Austin, Austin, TX.

22. Bäuerle, D., *Chemical processing with lasers*. Technology & Engineering, ed. Springer-Verlag. 1986. 245

23. Zäh M. F., K.M.D. *Elektronenstrahl für das selektive Sintern von metallischen Pulvern nutzen*. in *Euro-uRapid2006*. 2006. Frankfurt.

24. Zaeh M., K.M., *The effect of scanning strategies on electron beam sintering.* 2009. **3. Production Engineering**(3): p. 217-224.

25. Burkins M., W.M., Fanning J., Roopchand B., *The Mechanical and Ballistic Properties of an Electron Beam Single Melt of Ti-6Al-4V Plate*, A.R.L. ARL, Editor. 2001, Army Research Laboratory: Abedeen probing Ground, MD 21005.

26. Dandekar, D.P.S., Stephen V., *Shock Response of Ti-6Al-4V*, in *Conference on Shock Compression of Condensed Matter* 1999, American Physical Society: Snowbird, Utah.

27. Hiemenz J. (2006) *EBM Offers a New Alternative For Producing Titanium Parts And Prototypes*. Rapid Prototyping/Manufacturing.

28. Gordon L. (2012) *Electron beam melting builds titanium parts* Machine Design.com.

29. Ezugwu, E.O., J. Bonney, and Y. Yamane, *An overview of the machinability of aeroengine alloys.* Journal of Materials Processing Technology, 2003. **134**(2): p. 233-253.

30. Arrazola, P.J., et al., *Machinability of titanium alloys (Ti6Al4V and Ti555.3).* Journal of Materials Processing Technology, 2009. **209**(5): p. 2223-2230.

31. Dinga R., G.Z.X., Wilson A.,, Materials Science and Engineering A,, 2002(327): p. 233-245.

32. Lutjering G., Materials Science and Engineering A, 1998(243): p. 32-45.

33. Wooten JR., D.D. *Microstructural Evaluation of Electron Beam Melted Ti-6Al-4V*. in *Microscopy and Microanalysis*. 2008.

34. Christensen A., L.A., Kircher R., *Qualificaytion of electron beam melted (EBM) Ti6Al4V-ELI for othopeadic implant applications* in *Medical Modeling LLC.* . 2007.

35. Parthasarathy, J., et al., *Mechanical evaluation of porous titanium (Ti6Al4V) structures with electron beam melting (EBM).* Journal of the Mechanical Behavior of Biomedical Materials, 2010. **3**(3): p. 249-259.

36. Hrabe, N.W., et al., *Compression-compression fatigue of selective electron beam melted cellular titanium (Ti-6Al-4V).* Journal of Biomedical Materials Research Part B: Applied Biomaterials, 2011. **99B**(2): p. 313-320.

37. Ponader, S., et al., *In vivo performance of selective electron beam-melted Ti-6Al-4V structures.* Journal of Biomedical Materials Research Part A, 2010. **92A**(1): p. 56-62.

38. Haslauer, C.M., et al., *In vitro biocompatibility of titanium alloy discs made using direct metal fabrication.* Medical Engineering & Physics, 2010. **32**(6): p. 645-652.

39. Cooper K.G., G.J.E., Gilley S.D., *Layered Metals Fabrication Technology Development for Support of Lunar Exploration at NASA/MSFC*. 2008, NASA-MSFC: Huntsville, AL

40. Grimm T., *Direct Metal On the Rise*, in *Manufacturing Engineering* 2004, Society of Manufacturing Engineers.

41. DeGrange J. *Boeing's Vision for Rapid Progress between Dream and Reality*. in *Euro-uRapid2006*. 2006. Frankfurt, Germany.

42. Groth C, M.G., *Grundlagen: Basiswissen und Arbeitsbeispiele zur Finite-Elemente-Methode mit dem FE-Programm ANSYS*. 7th., Rev. 5.5 ed. 2002: Expert, Renningen.

43. Hofmeister W.H, W.M., Smugeresky J, Philliber J.A, Griffith M, Ensz M (1999) *Investigating Solidification with the Laser Engineered Net Shaping (LENS™) Process*. JOM-e **51**.

44. Hofmeister W.H, G.M.L., Ensz M.T, Smugeresky J.E, *Solidification in Direct Metal Deposition by LENS Processing.* JOM, 2001. **53**(9): p. 30-34.

45. Labudovic M., H.D., Kovacevic R., *A three dimensional model for direct laser metal powder deposition and rapid prototyping.* JOURNAL OF MATERIALS SCIENCE, 2003. **38**: p. 35- 49.

46. Kelly S.M, K.S.L., *Micro structural Evolution in Laser-Deposited Multilayer Ti-6Al-4V Builds: Part II. Thermal Modeling.* METALLURGICAL AND MATERIALS TRANSACTIONS A, 2004. **35A**.

47. Costa L., R.T., Deus AM, Vilar R. . *Simulation of layer overlap tempering kinetics in steel parts deposited by laser cladding*. in *International conference on metal powder deposition for rapid manufacturing*. 2002: Princeton (NJ).

48. Costa L., C.R., Reti T., Deus A.M., Vilar R., In: Bartolo PJ, Mitchell G, *Tempering effects in steel parts produced by additive fabrication using laser powder deposition*, in *Proceedings of VRP 2003 – 1st international conference on advanced research, in virtual and rapid prototyping. ESTG*. 2003: Instituto Politécnico de Leiria. p. 249.

49. Costa L., V.R., Reti T., Deus A.M., *Rapid tooling by laser powder deposition: Process simulation using finite element analysis* Acta Materialia, 2005 **53**: p. 3987-3999.

50. ESI Group. *SYSWELD*. 2006; Available from: http://www.esi-group.com/products/welding-old/sysweld.

51. Wang L., F.S., Gooroochurn Y., Wang P.T., Horstemeyer M.F., *Numerical Simulation of the Temperature Distribution and Solid-Phase Evolution in the LENS Process*, in *Solid Freeform Fabrication* 2006. p. 453-463.

52. Takeshita K, M.A., *Numerical Simulation of the Molten-Pool Formation during the Laser Surface-Melting Process.* METALLURGICAL AND MATERIALS TRANSACTIONS B, 2001. **32B**.

53. Ye R., S.J.E., Zheng B., Zhou Y., Lavernia E.,, *Numerical modeling of the thermal behavior during the LENS® process* Journal of Materials Science and Engineering, 2006. **A 428**: p. 47-53.

54. Neela V., D.A., *Three-dimensional heat transfer analysis of LENS process using finite element method.* International Journal of Advanced Manufacturing and Technology 2009.

55. Patil, R.B.Y., Vinod, *Finite element analysis of temperature distribution in single metallic powder layer during metal laser sintering.* International Journal of Machine Tools and Manufacture, 2007. **47**(7–8): p. 1069-1080.

56. Sigl M., *A Contribution to the Development of Electron Beam Sintering (Ein Beitrag zur Entwicklung des Elektronenstrahlsinterns)*, in *Mechanical Engineering - Machine Tool and Manufacturing Technology*. 2008, Dissertation Technische Universität München.

57. Gregory J. Gibbons, R.G.H., *Direct tool steel injection mould inserts through the Arcam EBM free-form fabrication process.* Assembly Automation, 2005. **25**(4): p. 300 - 305.

58. Ablitzer, D. *Mathematical Modeling of Electron Beam Remelting Process: Application to the Processing of Titanium Alloys*. in *Proceedings Conference EBM&R State of the Art* 1992.

59. Bellot J.P., F.E., Jardy A. and Ablitzer D. *Numerical simulation of the E.B.C.H.R. Process*. in *Proc_ Conf. EBM&R State of the Art* 1993.

60. Westerberg, K., McClelland M., Finlayson B. . *Numerical Simulation of Material and Energy Flow in an E-Beam Melt Furnace*. in *Proc. Conf. EBM&R State of the Art*. 1993.

61. Powell A., D.B., Fisher A., Van Den Avyle J., and Szekely J., *Numerical Simulation of Beam Melt Interaction in Electron Beam Melting.* Metallurgical and Materials Transactions B 1994.

62. Powell A., V.D.A.J., Damkroger B., Szekely J., and Pal U., *Analysis of Multicomponent Evaporation in Electron Beam Melting and Refining of Titanium Alloys.* METALLURGICAL AND MATERIALS TRANSACTIONS B, 1997. **28B**: p. 1227-1239.

63. Wei L., F.L., Jiandong H., Haibo Q., Naisheng Y., *Scan Strategy in Electron Beam Selective Melting.* Tsinghua Science & Technology, 2009. **14**(Supplement 1): p. 120-126.

64. Zäh, M.F., Lutzmann, S.,, *Modelling and simulation of electron beam melting.* Production Engineering, 2010. **4**(1): p. 15-23.

65. Körner, C., E. Attar, and P. Heinl, *Mesoscopic simulation of selective beam melting processes.* Journal of Materials Processing Technology, 2011. **211**(6): p. 978-987.

66. Nopper, R., *Mathematical Modeling: An Industrial Perspective.* COMSOL News, 2012.

67. Bianco N., M.O., Nardini S. and Tamburrino S., *A Numerical Model for Transient Heat Conduction in Semi-Infinite Solids Irradiated by a Moving Heat Source*, in *Comsol Conference* 2008: Hannover, Germany.

68. Rogers E., a.G.-M.E., *An Analysis of the Thermal Effects of Focused Laser Beams on Steel*, in *Comsol Conference* 2007.

69. Gaillard J., L.D., Mulani S.B. and Kapania R.K, *Residual Stresses in a Panel Manufactured Using EBF3 Process*, in *Comsol Conference* 2008: Boston, MA.

70. Zäh M.F., L.S., Kahnert M. and Walchshäusl F., *Determination of Process Parameters for Electron Beam Sintering (EBS)*, in *Comsol Conference*. 2008: Hannover, Germany.

71. Gusarov, A.V. and E.P. Kovalev, *Model of thermal conductivity in powder beds.* Physical Review B, 2009. **80**(2): p. 024202.

72. Verein Deutscher, I. and V.D.-G.V.u. Chemieingenieurwesen, *VDI-Wärmeatlas : Berechnungsblätter für den Wärmeübergang*. 2002, Berlin [etc.]: Springer.

73. Lagutkin S. A., S.L., Uhlenwinkel S., Vikas V.S., *Atomization process for metal powder.* Materials Science and Engineering: A, 2004. **383**(1): p. 1-6.

74. Neikov O.D, N.S., Gopienko V.G, Frishberg I.V.,, *Handbook of Non-Ferrous Metal Powders: Technologies and Applications*. 2009: Elsevier.

75. Anderson L.E., T.R.L., *Progress toward gas atomization processing with increased uniformity and control.* Materials Science and Engineering A,, 2002. **A326**(101).

76. Upadhyaya G. S., *Powder Metallurgy Technology*, ed. C.I.S. Publishing. 1998.

77. Donachie M.J., J.S., *Superalloys: A Technical Guide* 2002, Materials Park, OH: ASM International

78. Mills K. C., *Recommended Values of Thermophysical Properties for Selected Commercial Alloys*. 2002, Woodhead Publishing.

79. Washburn, E.W., Proceedings Natural Academy of Sciece 1921. **7**(115).

80. Webb, P.A. (2001) *An Introduction To The Physical Characterization of Materials by Mercury Intrusion Porosimetry with Emphasis On Reduction And Presentation of Experimental Data*.

81. NIST, *Porosity and Specific Surface Area Measurements for Solid Materials*, in *NIST Recommended Practice Guide* 2006.

82. Lowell S., S.J.L., Thomas M.A., Thommes M., , *Characterization of Porous Materials and Powders: Surface Area, Pore Size and Density*, ed. Springer. 2004.

83. Cooper J., *Particle Size Analysis - The Laser Diffraction Technique.* Materials World, 1998. **6**(1): p. 5-7.

84. De Boer G. B. J., D.W.C., Thoenes D., Goossens H. W. J., *Laser Diffraction Spectrometry: Fraunhofer Diffraction Versus Mie Scattering.* Particle Characterization 1987. **4**: p. 14-15.

85. Leroux, P. *Nanovea 3D Profilometers* 2010; Available from: http://www.nanovea.com/Profilometers.html.

86. Ramsey, A., *The Rules of X-Ray Micro CT*, in *Quality Magazine*. 2011, bnp Media p. 8-11.

87. Cape, J.A. and G.W. Lehman, *Temperature and Finite Pulse‐Time Effects in the Flash Method for Measuring Thermal Diffusivity.* Journal of Applied Physics, 1963. **34**(7): p. 1909-1913.

88. Gruner K.D. (2003) *Principles of Non-Contact Temperature Measurement*.

89. Xu J and Fisher T., *Enhanced Thermal Contact Conductance Using Carbon Nanotube Array Interfaces.* IEEE Transactions on Components and Packaging Technologies 2006. **29**(2).

90. Upadhyaya, G.S., *Powder Metallurgy Technology*. 1998: Cambridge International Science Publishing.

91. Dennies, J.W.D., *Electron Beam Melting Manufacturing for Production Hardware*. 2008, CalRAM, Inc.

92. Lütjering G., W.J.C., *Technological Aspects* in *Titanium*, Springer, Editor. 2007. p. 442.

93. Yule A.J., D.J.J., *Atomization of melts for powder production and spray deposition* Oxford Series on Advanced Manufacturing. 1994: Clarendon Press; illustrated edition edition (8 Sep 1994)

94. Özbilen, S., *Satellite formation mechanism in gas atomised powders.* Powder Metallurgy, Volume 42, Number 1, January 1999 , pp. 70-78(9), 1999. **42**(1): p. 70-78.

95. Rabin, B.H., G.R. Smolik, and G.E. Korth, *Characterization of entrapped gases in rapidly solidified powders.* Materials Science and Engineering: A, 1990. **124**(1): p. 1-7.

96. Ng, G., et al., *Porosity formation and gas bubble retention in laser metal deposition.* Applied Physics A: Materials Science & Processing, 2009. **97**(3): p. 641-649.

97. Zhao X., C.J., Lin X., Huang W, *Study on microstructure and mechanical properties of laser rapid forming Inconel 718.* Materials Science and Engineering A 2008. **478**: p. 119-124.

98. Zheng, G.K.L.N.A.E.W.J.G.B.H.Y., *Porosity formation and gas bubble retention in laser metal deposition.* Applied Physics A 2009. **97**: p. 641-649.

99. Ahsan M. N, P.A.J., Moat R. J., Shackleton J, *A comparative study of laser direct metal deposition characteristics using gas and plasma-atomized Ti–6Al–4V powders.* Materials Science and Engineering: A, 2011. **528**(25–26): p. 7648-7657.

100. Susan, D.F.P., J. D. Brooks, J. A. Robino, C. V., *Quantitative characterization of porosity in stainless steel LENS powders and deposits.* Materials Characterization, 2006. **57**(1): p. 36-43.

101. Ziya E., E.T.B., Sakir B.,, *Characterization of loose powder sintered porous titanium and Ti6Al4V alloy.* Turkish J. Eng. Env. Sci., 2009(33): p. 207 - 219.

102. B. Engel, D.L.B., *Titanium alloy powder preparation for selective laser sintering.* Rapid Prototyping Journal, 2000. **6**(2): p. 97-106.

103. Sun, P., et al., *The effect of CaO sintering on cyclic CO2 capture in energy systems.* AIChE Journal, 2007. **53**(9): p. 2432-2442.

104. Rootare, H.M.a.C.F.P., *Surface areas from Mercury Porosimeter Measurements.* Journal of Physics Chemistry, 1967. **71**: p. 2733-2736.

105. Spierings A.B., H.N., Levy G., *Influence of the particle size distribution on surface quality and mechanical properties in AM steel parts.* Rapid Prototyping Journal, 2011. **17**(3): p. 195-202.

106. Gibson I., R.D.W., Stucker B.,, *Additive Manufacturing Technologies: Rapid Prototyping to Direct Digital Manufacturing* Springer, Editor. 2009.

107. Karlsson J., F.S.F., Snis A., Unosson E., Engqvist H., Lausmaa J,. *Characterization and Comparison of Electron Beam Melting (EBM) Produced Ti-6Al-4V Parts Using Two Different Powder Fractions*. in *140th Annual Meeting & Exhibition, Additive Manufacturing of Metals: Electron Beam Melting (EBM) I*. 2011. San Diego Convention Center, San Diego, California USA.

108. LW Technology, I. *Methods of Powder Production*. Available from: http://www.lpwtechnology.com/Methods+of+Powder+Production+PT1RTXhBRE14b0RkdVZHZHU5Mlk.

109. Bandyopadhyay, A., Espana, F., Balla, V. K., Bose, S., Ohgami, Y., & Davies, N. M., *Influence of porosity on mechanical properties and in vivo response of Ti6Al4V implants.* Acta Biomaterialia, 2010. **6**(4): p. 1640-1648.

110. Balla, V.K., et al., *Quasi-static torsional deformation behavior of porous Ti6Al4V alloy.* Materials Science and Engineering: C, 2011. **31**(5): p. 945-949.

111. Newell, A.P., *Microstructure Studies of Ti-6Al-4V Near-Net Shape Structural Components as Prepared by the Arcam Electron Beam Melting Process*, in *Materials Science and Engineering*. 2009, North Carolina State University: Raleigh, NC. p. 153.

112. Arcam AB. *Ti6Al4V ELI Titanium Alloy*. Arcam EBM System 2008; Available from: http://www.arcam.com/CommonResources/Files/www.arcam.com/Documents/EBM%20Materials/Arcam-Ti6Al4V-ELI-Titanium-Alloy.pdf.

113. Wang L., Z.-b.L., Hong-pei S.,, *Properties and forming process of prealloyed powder metallurgy Ti-6Al-4V alloy.* Transactions of Nonferrous Metals Society of China, 2007. **17**(3): p. 639 - 643.

114. Wang, L. and S. Felicelli, *Process Modeling in Laser Deposition of Multilayer SS410 Steel.* Journal of Manufacturing Science and Engineering, 2007. **129**(6): p. 1028-1034.

115. Gackstetter, M., *Measurements of Particle Size Distribution by Wet & Dry Laser Diffraction*. 2007, Malvern Instruments.

116. Kakushadze, T.I., *Electron heat capacity in transition metals and alloys. II.* Annalen der Physik, 1961. **463**(7-8): p. 360-365.

117. Cezairliyan A., M.J.L.a.T.R., *Thernmophysical Measurements on 90Ti-6Al-4V Alloy Above 1450K Using a Transient (Subsecond) Technique.* Journal of Research of the National Bureau of Standards -A. Physics and Chemistry 1977. **81A**(2-3): p. 251-256.

118. Basak, D., R.A. Overfelt, and D. Wang, *Measurement of Specific Heat Capacity and Electrical Resistivity of Industrial Alloys Using Pulse Heating Techniques.* International Journal of Thermophysics, 2003. **24**(6): p. 1721-1733.

119. Boivineau, M., et al., *Thermophysical Properties of Solid and Liquid Ti-6Al-4V (TA6V) Alloy.* International Journal of Thermophysics, 2006. **27**(2): p. 507-529.

120. Miloševic N, A.I., *Thermophysical properties of solid phase Ti-6Al-4V alloy over a wide temperature range.* International Journal of Materials Research, 2012(6): p. 707-714.

121. Homporova P., P.M., Stockinger M., Warchomicka F.,. *Dynamic phase evolution in titanium alloy Ti-6Al-4V*. in *The 12th World Conference on Titanium*. 2011.

122. Coppa, P. and A. Consorti, *Normal emissivity of samples surrounded by surfaces at diverse temperatures.* Measurement, 2005. **38**(2): p. 124-131.

123. Yang, J., et al., *Experimental investigation and 3D finite element prediction of the heat affected zone during laser assisted machining of Ti6Al4V alloy.* Journal of Materials Processing Technology, 2010. **210**(15): p. 2215-2222.

124. Atallah, S., *A relationship between emissivity and thermal conductivity of metals.* Britanic Journal for Applied Physics. , 1966. **17** (Letters to the Editor): p. 573-574.

125. Sih S., B.J.W. *Emissivity of Powder Beds*. in *Proceedings of the 6th Annual SFF Symposium*. 1995. The University of Texas at Austin.

126. Liu D.M , T.W.H., Chiu C.C.,, *Thermal diffusivity, heat capacity and thermal conductivity in A1203-Ni composite.* Materials Science and Engineering B, 1995. **31**: p. 287-291.

127. Koike, M., et al., *Evaluation of titanium alloy fabricated using electron beam melting system for dental applications.* Journal of Materials Processing Technology, 2011. **211**(8): p. 1400-1408.

128. Dabrowski R., *The Kinetics of Phase Transformations During Continous Cooling of the Ti6Al4V Alloy from the beta Single-Phase Range* Archive of Metallurgy and Materials 2011. **56** (3).

129. Karlsson J., S.A., Norell M., Engqvist H., Lausmaa J.,. *Characterization of Surface Oxides on Ti-6Al-4V Manufactured by Electron Beam Melting*. in *Materials Science & Technology 2012* 2012. Pittsburgh, PA.

130. Thomsen P., M.J., Emanuelsson L.,Rene M.,Snis A.,, *Electron beam-melted, free-form-fabricated titanium alloy implants: Material surface characterization and early bone response in rabbits.* Journal of Biomedical Materials Research Part B: Applied Biomaterials, 2008. **90B**(1).

131. Takahashi, Y., et al., *Laser-flash calorimetry I. Calibration and test on alumina heat capacity.* The Journal of Chemical Thermodynamics, 1979. **11**(4): p. 379-394.

132. Risegari, L., et al., *Low Temperature Thermal Conductivity of Ti6Al4V Alloy.* Journal of Low Temperature Physics, 2008. **151**(3): p. 645-649.

133. Costan A., D.A., Iionita A., Forna N, Perju M.C., Agop M.,, *Thermal properties of a Ti-6Al-4V alloy used as dental implant material.* OPTOELECTRONICS AND ADVANCED MATERIALS – RAPID COMMUNICATIONS, 2011. **5**(1): p. 92-95.

134. Goel, T.G. and B.A. Unvala, *Effect of phase transformation on the measurements of thermal conductivity and other physical properties of titanium.* Physics Letters A, 1970. **32**(7): p. 521-522.

135. Shapiro M., D.V., Royzen V, Krichevets Y., Lekhtmakher S., Grozubinsky V., Shapira M., Brill M., *Characterization of Powder Beds by Thermal Conductivity: Effect of Gas Pressure on the Thermal Resistance of Particle Contact Points.* Particle & Particle Systems Characterization, 2004. **21**(4).

136. Tritt. T.M., *Thermal Conductivity: Theory, Properties and Applications* Physics of Solids and Liquids 2004, New York: Kluver Academic / Plenum Publishers

137. Klemens, P.G. and R.K. Williams, *Thermal conductivity of metals and alloys.* International Materials Reviews, 1986. **31**(1): p. 197-215.

138. Kiseleva, A.F., V.A. Klimenko, and Y.S. Malakhov, *Thermal conductivity of the transition metals.* Russian Physics Journal, 1969. **12**(5): p. 577-581.

139. Williams, W.S., *High-Temperature Thermal Conductivity of Transition Metal Carbides and Nitrides.* Journal of the American Ceramic Society, 1966. **49**(3): p. 156-159.

140. Kobryn, P.A. and S.L. Semiatin, *Microstructure and texture evolution during solidification processing of Ti–6Al–4V.* Journal of Materials Processing Technology, 2003. **135**(2–3): p. 330-339.

141. Antonysamy A.A., P.P.B.a.M.J., *Effect of Wall Thickness Transitions on Texture and Grain Structure in Additive Layer Manufacture (ALM) of Ti-6Al-4V.* Materials Science Forum, 2012. **706-709**: p. 205-210.

142. Puebla K., M.L.E., Gaytan S. M., Martinez E., Medina F., Wicker R. B.,, *Effect of Melt Scan Rate on Microstructure and Macrostructure for Electron Beam Melting of Ti-6Al-4V.* Materials Sciences and Applications, 2012. **3**: p. 259-264.

143. Howell J. R., S.R., Menguc M. P.,, *Thermal radiation heat transfer*. 2011.

144. Taimarov, M.A., K.A. Rusev, and F.A. Garifullin, *Directional emissivity of structural materials.* Journal of Engineering Physics and Thermophysics, 1985. **49**(2): p. 939-942.

145. Peacock D., *Titanium for Automotive Applications* in *Materials World*. 1997. p. 580-583.

146. Eschey C., L.S., Zaeh M.F., *Examination of the powder spreading effect in Electron Beam Melting (EBM)*, in *Solid Free Form Fabrication Conference* 2009: Austin, Texas. p. 308 - 319.

147. Winterberg M., T.E., *Correlations for e!ective heat transport coefficients in beds packed with cylindrical particles.* Chemical Engineering Science 2000. **55**: p. 5937-5943.

148. Song, B., et al., *Process parameter selection for selective laser melting of Ti6Al4V based on temperature distribution simulation and experimental sintering.* The International Journal of Advanced Manufacturing Technology, 2011: p. 1-8.

149. Mahale, T., *Electron Beam Melting of Advanced Materials and Structures*, in *Industrial Engineering*. 2009, North Carolina University: Raleigh, NC.

150. Fuwa, K. and B.L. Valle, *The Physical Basis of Analytical Atomic Absorption Spectrometry. The Pertinence of the Beer-Lambert Law.* Analytical Chemistry, 1963. **35**(8): p. 942-946.

151. Jansen K.E., W.C.H., Hulbert G.M., , *A generalized-alpha method for integrating the filtered Navier-Stokes equations with a stabilized finite element method.* Computational Methods Applied. Engineering, 2000. **190**: p. 305-319.

152. Tendero, C., et al., *Atmospheric pressure plasmas: A review.* Spectrochimica Acta Part B: Atomic Spectroscopy, 2006. **61**(1): p. 2-30.

153. Hudak, S., *Atmospheric Plasma Depainting* in *Surface Engineering and Structural Materials* 2012, SERDP, WP-1762.

154. McWilliams, A.J.H., S.J. Shannon, S. C. and Cuomo, J.J. *Optical characterization of atmospheric torch operating modes*. in *38th IEEE International Conference on Plasma Science* 2011. Chicago, IL.

155. McWilliams, A.J.H., S.J. Shannon, S. C. and Cuomo, J.J. *Analysis of Atmospheric Pressure Plasma Torch and the Effects of Multiple Gas Compositions on Plasma Chemistry and its Interaction with High Density Polyethylene*. in *39th IEEE International Conference on Plasma Science* 2012. Edinburgh, UK.

156. Peet M. J., H.H.S., and BhadeshiaH. K. D. H, *Prediction of thermal conductivity of steel.* International Journal of Heat and Mass Transfer, 2011. **54**: p. 2602-2608.

157. Slattery K., S.B., Speore E., Good J., Gilley S.,and McLemore C. *Evaluation of Arcam Deposited Ti6-Al-4V* in *2nd SAIAS Symposium*. 2008. Stellenbosch, South Africa.

158. Bayoumi, M.R. and A.K. Abdellatif, *Effect of surface finish on fatigue strength.* Engineering Fracture Mechanics, 1995. **51**(5): p. 861-870.

159. Murr, L.E.G., S. Medina, M. Martinez, F. E. Hernandez, D. H. Martinez L., *Effect of Build Parameters and Build Geometries on Residual Microstructures and Mechaical Properties of Ti-6Al-4V Components Built by Electron Beam Melting (EBM)*, in *Annual International Solid Freeform Fabrication Symposium* 2009: Austin, Texas, USA. p. 374-397.

160. Thomsen, P., et al., *Electron beam-melted, free-form-fabricated titanium alloy implants: Material surface characterization and early bone response in rabbits.* Journal of Biomedical Materials Research Part B: Applied Biomaterials, 2009. **90B**(1): p. 35-44.

161. Smock, D., *Aircraft Engineers Explore Additive Manufacturing Technologies*, in *Engineering Materials*. 2010.

162. D. Ciscel, *CalRAM, Inc. Newsletter*. 2010, CalRam Simi Valley, CA.

163. Badrosamay M., Y.E., Van Vaerenbergh J., and Kruth J.P. *Improving productivity rate in SLM of commercial steel powders*. in *RAPID 2009 Conference & Exposition*. 2009. Schaumburg, IL.

164. Microteck Finishing, L. *The Micromachining Process - MMP*. 2011; Available from: http://www.microtekfinishing.com/.

165. Srisawadi, S., *An Investigation of Rapid Tooling For Electrochemical Machining of Ti-6Al-4V Alloy*, in *Industrial Engineering* 2006, North Carolina State University Raleigh

166. B Liu, W.R., Tuck C., Ashcroft I. *Investigation the effect of particle size distrubution on processing parameters optimization in selective laser melting process*. in *Twenty Second Annual International Solid Freeform Fabrication Symposium – An Additive Manufacturing Conference* 2011. Austin, TX

167. Microteck Finishing, L. 2011; Available from: http://www.microtekfinishing.com/binc_mmp.php.

168. Sodick, C.L. *Improvement of surface finish*. 2010; Available from: http://www.sodick.jp/product/beam/index.html.

169. AFS - American Foundry Society. *Surface finising for casting process*. 2010; Available from: http://prod.afsinc.rd.net/content.cfm?ItemNumber=6915&RDtoken=3453&userID=.

170. Atkinson, H. and S. Davies, *Fundamental aspects of hot isostatic pressing: An overview.* METALLURGICAL AND MATERIALS TRANSACTIONS A, 2000. **31**(12): p. 2981-3000.

171. Ipmd.net, *Recent trends in Hot Isostatic Pressing (HIP) technology: Part 1 - Equipment.* 2012.

172. Mculler-Reichert T., M.J., Lich B., and McDonald K.,, *Three-Dimensional Reconstruction Methods for Caenorhabditis Elegans Ultrastructure.* Methods in Cell Biology, 2010. **96**(Chapter 15): p. 331-361.

173. Zankel, A., et al., *Ultramicrotomy in the ESEM, a versatile method for materials and life sciences.* Journal of Microscopy, 2009. **233**(1): p. 140-148.

174. Karayazgan-Saracoglu B, G.Y., Atay A., *Fabrication of an auricular prosthesis using computed tomography and rapid prototyping technique.* Journal of Craniofacial Surgery, 2009. **20**(4): p. 1169-1172.

175. Rotaru, H., et al., *Cranioplasty With Custom-Made Implants: Analyzing the Cases of 10 Patients.* Journal of Oral and Maxillofacial Surgery, 2012. **70**(2): p. e169-e176.

176. Fitzwater, K.L., *Rapid Prototyping and Computed Tomography Optimization of Canine Long Bone Modeling*, in *Veterinary Clinical Sciences*. 2010, Ohio State University. p. 58.

177. Kroll Julia, I.E., Alexander Verl, *New solutions for industrial inspection based on 3D computer tomography*, in *Internationasl Society for Optics and Photonics: Optical and Digital Image Processing*. 2008.

178. Effenberger, N.B.a.I. *3D Computed Tomography - Technology, Applications and Process Integration*. in *16th World Conference on Nondestructive Testing*. 2004. Montreal, Canada: International Committee for Nondestructive Testing.

179. Jande, Y.A.C., *Manufacturing and Characterization of Uniformly Porous and Graded Porous Polymeric Structures via Selective Laser Sintering*, in *Mechanical Engineering*. 2009, Middle Esat Technical University

180. Wang L., P.P., Felicelli S.D., El Kadiri H., Wang P., , *Experimental Analysis of Porosity Formation in Laser-Assisted Powder Deposition Process*, in *2009 TMS Annual Meeting & Exhibition* 2009.

181. Murr, L.E., et al., *Microstructure and mechanical behavior of Ti–6Al–4V produced by rapid-layer manufacturing, for biomedical applications.* Journal of the Mechanical Behavior of Biomedical Materials, 2009. **2**(1): p. 20-32.

182. Schwerdtfeger, J.V.S., R.F. Körner, C, *In-situ Flaw Detection by IR-imaging during Electron Beam Melting.* Rapid Prototyping Journal, 2012. **18**(4).

183. Ritchie, M., et al., *X-ray-based measurement of composition during electron beam melting of AISI 316 stainless steel: Part I. Experimental setup and processing of spectra.* METALLURGICAL AND MATERIALS TRANSACTIONS A, 2003. **34**(3): p. 851-861.